MASS MEASUREMENT OF THE LIGHTWEIGHT SELF-CONJUGATE NUCLEUS ZIRCONIUM-80 AND THE DEVELOPMENT OF THE SINGLE ION PENNING TRAP

By

Alec Scott Hamaker

A DISSERTATION

Submitted to
Michigan State University
in partial fulfillment of the requirements
for the degree of

Physics - Doctor of Philosophy

2021

ABSTRACT

MASS MEASUREMENT OF THE LIGHTWEIGHT SELF-CONJUGATE NUCLEUS ZIRCONIUM-80 AND THE DEVELOPMENT OF THE SINGLE ION PENNING TRAP

By

Alec Scott Hamaker

An atom's mass provides a unique probe to the various interactions occurring within its nucleus. Hence, precise atomic mass measurements are fundamental for nuclear physics research. Penning trap mass spectrometry (PTMS) is currently the most precise method for performing these measurements. The Low Energy Beam and Ion Trap (LEBIT) Facility at the National Superconducting Cyclotron Laboratory (NSCL) uses PTMS to measure the masses of rare isotopes produced via projectile fragmentation. In this work, mass measurements of $^{80\text{-}83}$Zr and the development of the single ion Penning trap, both performed at the LEBIT facility, are presented.

Protons and neutrons in the atomic nucleus move in shells analogous to the electronic shell structures of atoms. The nuclear shell structure varies due to changes of the nuclear mean field with the number of neutrons N and protons Z. These variations can be probed by measuring mass differences between nuclei. The $N = Z = 40$ self-conjugate nucleus ^{80}Zr is of particular interest as its proton and neutron shell structures are expected to be very similar, and its ground state is highly deformed. Here, evidence for the existence of a deformed double shell closure in ^{80}Zr is presented through precision mass measurements of $^{80\text{-}83}$Zr. The measurement shows that ^{80}Zr is significantly lighter, and thus more strongly bound than predicted. This can be attributed to the deformed shell closure at $N = Z = 40$ and the large Wigner energy. A statistical Bayesian model mixing analysis employing several global nuclear mass models demonstrates difficulties reproducing the observed mass anomaly

using current theory.

To refine the deformed shell closure, high precision mass measurements in the ^{80}Zr region are needed, which will be made possible with next-generation radioactive ion beam facilities such as the Facility for Rare Isotope Beams (FRIB) and higher sensitivity mass measurement techniques. Current PTMS techniques used for rare isotope mass measurements are destructive. While these methods are flexible, they require a significant number of detected ions ($\sim$ 100 ions). The most exotic isotopes, however, may only be delivered at rates on the order of one ion per day, making mass measurements with the destructive techniques nearly impossible due to time restraints. To this end, LEBIT has developed a new single ion Penning trap (SIPT), which makes use of the non-destructive narrowband Fourier transform ion cyclotron resonance (FT-ICR) technique. Although FT-ICR is a widely used technique, it has never been applied to rare isotope mass measurements. SIPT's key features, development, and commissioning are presented in this work.

ACKNOWLEDGMENTS

Graduate school has been one of the most difficult but rewarding experiences of my life, and I am extremely grateful to those who helped me navigate it. First, I must thank the entire NSCL and FRIB staff and community. Their dedication to the science and facility provided the foundation for many successful LEBIT experiments during my time with the group.

Second, I would like to thank my advisor Georg Bollen for giving challenging and rewarding projects, providing funding to attend conferences locally and globally, and pushing me to become a better, more inquisitive scientist. I am thankful for my supportive committee: Oscar Naviliat-Cuncic, Witold Nazarewicz, Luke Roberts, Chong-Yu Ruan, and Hendrik Schatz. Their encouragement helped instill the confidence I needed in myself and my work. In particular, I must thank Professor Nazarewicz who provided extensive knowledge, analysis, and guidance throughout the ^{80}Zr mass measurement project. He, along with Rahul Jain, Samuel Giuliani, and Léo Neufcourt supplied valuable theory and statistical input to help with the interpretation of the experimental results.

Next, I must give a huge thank you to Ryan Ringle for being an excellent supervisor and team leader. Ryan was always available to provide direction, support, and assistance towards any and all of my projects, papers, presentations, and life problems. He also properly introduced me to coffee and the industrial rock music scene. Our gas cell collaborators Chandana Sumithrarachchi and Kasey Lund played a crucial role during my time at the lab as well. Not only did they provide the necessary beams and banter that led to many successful LEBIT experiments, they were always willing to give career advice and support.

I had the privilege to work with many great postdocs and students over the years. Martin Eibach and Kerim Gulyuz helped introduce me to LEBIT and Penning trap mass spectrom-

etry. Nadeesha Gamage was always available to discuss code and data analysis techniques. I am especially grateful for Erich Leistenschneider who assisted me with almost all aspects of the work presented in this thesis. Erich is a great scientist with a positive attitude that never seems to fade. I must thank Rachel Sandler and Chris Izzo for showing me the LEBIT ropes and coaching me through my early years of graduate school. I would not have been able to take SIPT as far along as it is today without Chris's teachings and initial work. A special thank you goes to Isaac Yandow, Danny Puentes, Jason Surbrook, and Catherine Nicoloff for being great colleagues and greater friends. Our discussions and shenanigans, no matter how meaningless, were always so enlightening.

I must thank my family for their endless love and support. My mom, Rhonda, has always been my biggest cheerleader while my dad, Andrew, always nurtured my strong work ethic. My sister, Alicia, is one of my biggest role models and has helped me handle many of life's curveballs. Finally, I must thank my wonderful wife, Monica, who has supported me throughout my entire physics career – since high school! She helped me celebrate the good times and pulled me out of the mud during the tough times. I am and forever will be thankful for her advice, encouragement, support, and love.

TABLE OF CONTENTS

LIST OF TABLES

LIST OF FIGURES

Chapter 1

Introduction

One of the most fundamental properties of an atom is its mass. The mass of an atom is not simply the sum of the masses of its constituent protons, neutrons, and electrons; a portion of the mass manifests itself as binding energy, which is responsible for holding the nucleus of the atom together. The binding energy of a nucleus with N neutrons and Z protons is found by determining the mass difference between the sum of the atom's constituent particles and its mass:

$$B(N,Z) = [NM_n + ZM_H - M(N,Z)]c^2 \tag{1.1}$$

where M_n, M_H are the masses of the neutron and hydrogen atom, respectively, and $M(N,Z)$ is the mass of the atom. This energy provides a unique probe to the various interactions that occur within the nucleus of the atom. Many techniques have been developed over the years to measure masses. Masses can be determined directly with techniques based on time-of-flight, magnetic rigidity, or frequency measurements. They can also be measured indirectly through mass differences relative to a known mass. To make meaningful contributions to nuclear science, masses M typically have to be measured to a high level of precision or low level of uncertainty δM. Relative mass uncertainties needed for advanced studies of nuclear structure, astrophysics, and fundamental interactions are usually $\delta M/M \leq 10^{-6}$, 10^{-7}, and 10^{-8}, respectively. Once measured to these high levels of precision, masses and differences in masses become useful tools for understanding the nucleus.

1.1 Mass Differences as a Probe for Nuclear Structure

Unique features in many fundamental properties of nuclei occur at specific numbers of protons or neutrons. These so-called magic numbers can be detected in trends of experimental observables such as binding energies [13], excitation energies [14], and nuclear radii [15]. In binding energy data, for example, a nucleus with a magic number of protons or neutrons typically has a lighter mass or enhanced $B(N, Z)$ relative to neighboring nuclei. The nuclear shell model attributes the emergence of magic numbers to a shell structure of the nucleus [16–18]. The shell model is a similar quantum mechanical treatment to that of electrons orbiting a nucleus. For the nucleus, however, one must consider nuclear forces and a much stronger spin-orbit interaction in addition to the Coulomb force and Pauli exclusion principle. In many cases, excellent agreement is observed between shell model predictions and the location of magic numbers particularly for stable or long-lived nuclei. When studying more exotic nuclei beyond the valley of stability, disagreements between theory and experiment become more apparent. Understanding the mechanisms of structural evolution in these regions of the nuclear chart is an active area of nuclear science [19, 20]. A common method for extracting information about the structure of the nucleus and exploring the discrepancies between theory and experiment is through the use of mass differences or binding-energy indicators [21, 22].

The simplest binding-energy indicators are the one and two-proton separation energies

$$S_p(N, Z) = B(N, Z) - B(N, Z - 1)\,, \tag{1.2}$$

$$S_{2p}(N, Z) = B(N, Z) - B(N, Z - 2)\,, \tag{1.3}$$

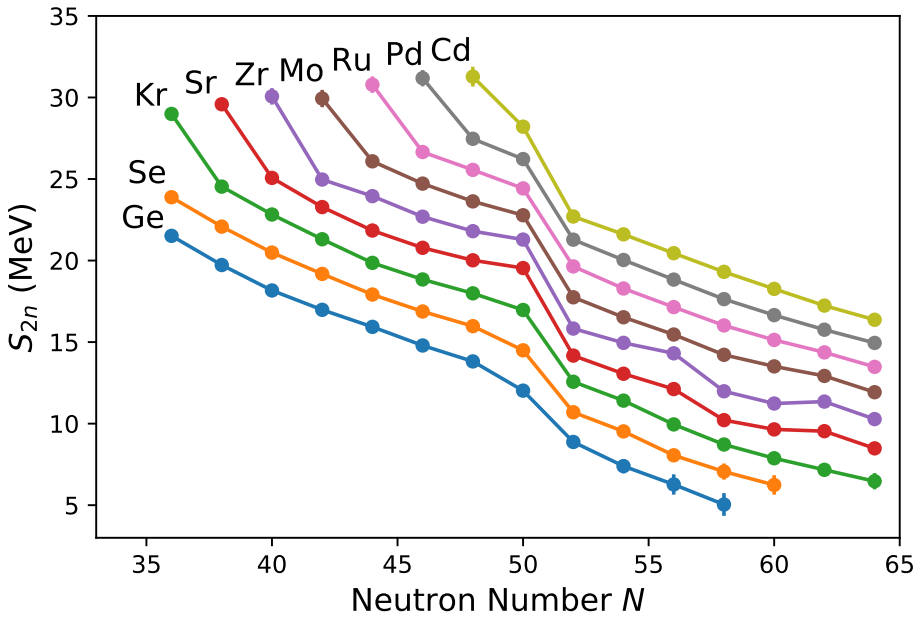

Figure 1.1: Two-neutron separation energies S_{2n} as a function of neutron number for even-even nuclei along isotopic chains between $Z = 32$ and $Z = 48$ using data from [1]. All symbols include error bars. In many cases the error bars are too small to see. The $N = 50$ magic number can be observed through the sharp decrease in S_{2n} just after $N = 50$.

as well as the one and two-neutron separation energies

$$S_n(N, Z) = B(N, Z) - B(N - 1, Z)\,, \tag{1.4}$$

$$S_{2n}(N, Z) = B(N, Z) - B(N - 2, Z). \tag{1.5}$$

Studying trends in these quantities is one method for identifying the location of magic numbers. For example, the $N = 50$ magic number reveals itself across several isotopic chains in the two-neutron separation energies plotted in Fig. 1.1 through the sharp decrease in S_{2n} just after $N = 50$. Other useful quantities for studying the structure of the nucleus can be derived from eqs. 1.2–1.5. One such quantity is the double mass difference δV_{pn} defined

as [23–25]:

$$\begin{aligned}\delta V_{pn}(N,Z) &= \frac{1}{4}[B(N,Z) - B(N-2,Z) - B(N,Z-2) + B(N-2,Z-2)] \\ &= \frac{1}{4}[S_{2p}(N,Z) - S_{2p}(N-2,Z)],\end{aligned} \tag{1.6}$$

which is a common tool for studying the residual p-n interaction of the last two protons with the last two neutrons, though it can also be used to study shell closures [26].

1.2 Nuclear Structure near $N = Z = 40$

Portions of the text in this section were recently accepted in Nature Physics [26] and are reproduced here with permission from Springer Nature. Additional details and discussion are included as well. The neutron-deficient region around mass number $A = 80$ is a rich area for studies of basic nuclear structure concepts [27]. Nuclei in this region rapidly change their properties with proton and neutron numbers. Indeed, some of these nuclei are among the most deformed in the nuclear chart showing collective behavior, while others exhibit non-collective excitation patterns typically observed in spherical systems.

The appearance of strongly deformed configurations around ^{80}Zr has been attributed to the population of the intruder $g_{9/2}$ orbitals separated by the spherical $N = Z = 40$ subshell closure from the upper-pf shell as can be seen in the single-particle energy diagram of Fig. 1.2. This specific shell structure leads to shape coexistence predicted by theory in nuclei near $N \approx Z \approx 40$ [2, 28–32]. For the nucleus ^{80}Zr in particular, spherical and deformed (prolate, oblate, and triaxial) structures are expected to coexist at low energies, and their competition strongly depends on the size of the calculated spherical $N = Z = 40$ gap [33]. Experimentally, ^{80}Zr has a very large prolate quadrupole deformation parameter

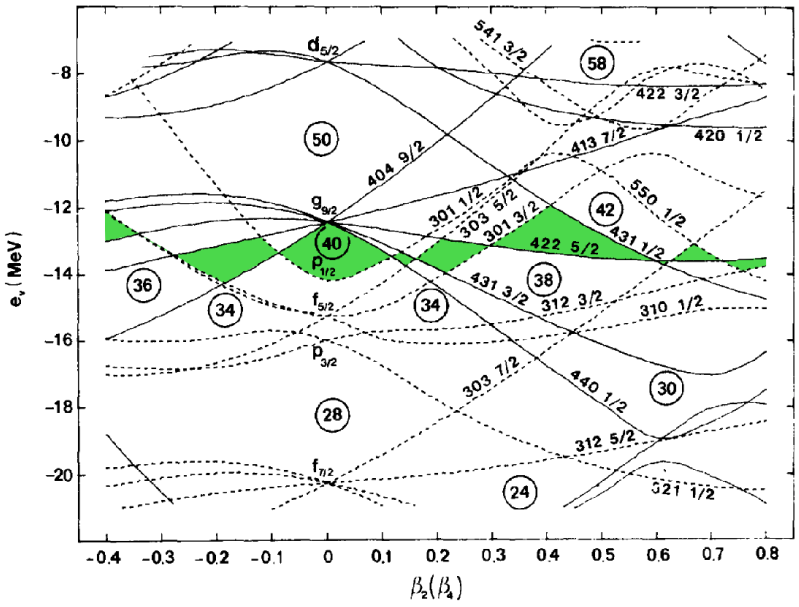

Figure 1.2: Neutron single-particle energy levels in Sr ($Z = 38$) as a function of the quadrupole deformation parameter β_2 as calculated in [2]. The gaps at $N = 40$ are highlighted in green. A large energy gap is possible at $\beta_2 \approx 0.4$ depending on the energy of the $g_{9/2}$ orbital. The results of this calculation can be used to qualitatively understand the structure of nearby nuclei such as ^{80}Zr. Figure adapted from [2].

$\beta_2 \approx 0.4$ [34, 35]. This has been attributed to the appearance of the large deformed gap at $N = Z = 40$ in the deformed single-particle spectrum [2], seen in Fig. 1.2, which is due to the relatively low density of single-particle levels near $\beta_2 \approx 0.4$ [2, 36]. Consequently, the nucleus ^{80}Zr can be viewed as a deformed doubly-magic system.

In addition to shape-coexistence effects, ^{80}Zr is a great laboratory for isospin physics. Having an equal number of protons and neutrons, this nucleus is self-conjugate; hence, it offers a unique venue to study proton-neutron pairing, isospin breaking effects, and the Wigner energy [4, 37].

There is a tendency for nuclei with $N = Z$ to be more strongly bound than their neighboring nuclei [13]. This so-called Wigner energy is thought to be a consequence of proton-neutron pairing. However, it is not reproduced well by modern theoretical approaches, so

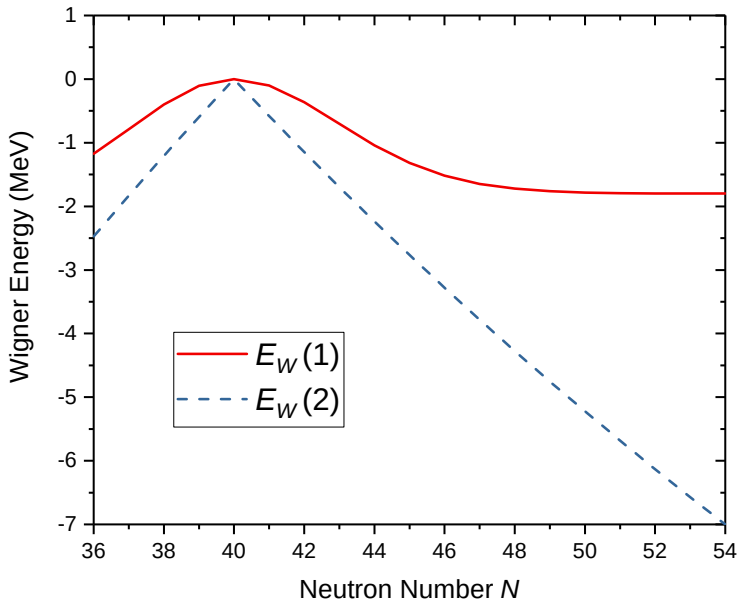

Figure 1.3: Comparison of the phenomenological Wigner energy models $E_W(1)$ (eq. 1.7 offset by V_W) [3] and $E_W(2)$ (eq. 1.8) [4] along the Zr isotopic chain.

it must be accounted for with a phenomenological approach that relies on large-scale fits to binding energy data. There are a few phenomenological expressions for the Wigner energy E_W. Two of those are described here.

In the HFB-24 mass model [3], the Wigner term has been parametrized as:

$$E_W(1) = V_W e^{-\lambda_W \left(\frac{N-Z}{A}\right)^2} + V'_W |N-Z| e^{-\left(\frac{A}{A_0}\right)^2}. \tag{1.7}$$

One set of values for the free parameters determined in [3] and employed in this thesis is $V_W = 1.8\,\mathrm{MeV}$, $\lambda_W = 380$, $V'_W = -0.84\,\mathrm{MeV}$, and $A_0 = 26$. In this model, E_W rapidly decreases initially with $|N-Z|$ before leveling off as $|N-Z|$ grows. In the traditional parametrization of E_W,

$$E_W(2) = -a_W \frac{|N-Z|}{A}, \tag{1.8}$$

one assumes that $E_W = 0$ at $N = Z$ and linearly decreases with the neutron excess. In this work, the value $a_W = 47\,\mathrm{MeV}$ is adopted from Ref. [4]. These phenomenological Wigner energy contributions to the binding energy along the Zr isotopic chain are shown in Fig. 1.3. The Wigner energy coefficient in eq. 1.8, $W(A) = a_W/A$, can be extracted empirically in an even-even nucleus with $N = Z = A/2$ [4]:

$$W(A) = \delta V_{pn}(A/2, A/2) - \frac{1}{2}\left[\delta V_{pn}(A/2, A/2-2) + \delta V_{pn}(A/2+2, A/2)\right]. \tag{1.9}$$

This quantity can be used to study the contributions of the Wigner energy to the total binding energy of a nucleus.

In Chapter 4, the results of a mass measurement of ^{80}Zr will be presented. The mass measurement will be interpreted in terms of its Wigner energy as well as the deformed shell closure at $N = Z = 40$. Comparisons of the results to theoretical mass models using a Bayesian model averaging (BMA) technique will also be discussed [38].

1.3 Precision Mass Measurements of Rare Isotopes

As discussed in the previous section, atomic masses are an important tool for studying the interactions within the nucleus, and high precision mass measurements, particularly of rare isotopes, are necessary to interpret these interactions. Many techniques have been developed over the years to measure atomic masses and push the precision limit. Mass measurement techniques are typically divided into direct and indirect techniques. Indirect techniques consist of measuring properties of a reaction or decay. These methods give one access to mass differences, or Q-values, which can be used to determine the mass of either the parent

or daughter nuclei of the reaction or decay. In this way, chains of Q-values can be used to determine masses of isotopes far from the valley of stability. However, the uncertainties are compounded for each mass difference resulting in rather large uncertainties if the reference isotope of the Q-value chain is far from the final isotope of the chain.

Direct techniques make use of time-of-flight, magnetic rigidity, and frequency measurements. Mass measurements of isotopes far from the valley of stability that are produced at very low rates and have extremely short lifetimes can typically be determined using the time-of-flight magnetic rigidity method [39]. This technique has been employed to measure masses of rare isotopes at many facilities around the world including SPEG at GANIL [40] and the S800 spectograph at the NSCL [41]. The mass resolution of these experiments is rather low due to the relatively short time of flight, and the relative mass uncertainty $\delta m/m$ is usually limited to about 10^{-6} [39]. Cyclotrons have been used to increase the flight path resulting in higher resolution. This has been done, for example, at Grenoble [42]. Storage rings, such as the Experimental Storage Ring (ESR) at GSI [43] and the Heavy Ion Cooler-Storage-Ring (HIRFL-CSR) at Lanzhou [44], are another device that increase the time-of-flight path by allowing particles to make many passes through the ring. More recently, the multi-reflection time-of-flight (MR-TOF) device was developed to perform mass measurements of rare isotopes. MR-TOFs bounce ions between two electrostatic deflectors extending their flight paths by the number of turns within the device. MR-TOFs achieve extremely high resolving powers, so they are typically employed as a beam purifier [45–48]. However, they can also be used as a high-precision mass spectrometer [48–53].

The most accurate and precise direct method is Penning trap mass spectrometry (PTMS). The Penning trap makes use of a strong magnetic field that provides access to the cyclotron frequency of an ion. A measurement of the cyclotron frequency allows for the determination

of the mass. The Penning trap and the techniques used to measure the cyclotron frequency will be discussed in Chapter 2. Penning traps have been used to achieve relative mass uncertainties of $\delta M/M < 10^{-10}$ on stable ions [54] and $\delta M/M < 10^{-8}$ on unstable ions [55]. They have also been used to measure very short-lived rare isotopes $t_{1/2} < 10$ ms to high precision $\delta M/M \sim 10^{-7}$ [56]. Many rare isotope beam facilities around the world have PTMS programs performing mass measurements: ISOLDE at CERN [57], JYFLTRAP at Jyväskylä [58], SHIPTRAP at GSI [59], CPT at Argonne National Lab [60], TITAN at TRIUMF [61], and LEBIT at the NSCL [62].

The Low Energy Beam and Ion Trap (LEBIT) facility at the National Superconducting Cyclotron Laboratory (NSCL) is currently the only Penning trap program coupled to a projectile fragmentation facility. This allows access to rare isotopes that are not available to other PTMS facilities. LEBIT has been active for over 15 years and achieving mass precisions for rare isotopes as low as $\sim$ 2 ppb [55] as well as measuring isotopes with half-lives less than 100 ms [63]. Currently, the NSCL is transitioning to the Facility for Rare Isotope Beams (FRIB), which will provide access to even more exotic isotopes that were difficult or impossible to produce at the NSCL. This upgrade will continue the mass measurement campaign at LEBIT for many years to come.

1.4 Achieving Highest Sensitivity with Non-Destructive Mass Determination

Although FRIB will improve rare isotope production yields by orders of magnitude, many isotopes of interest will still only be delivered at rates on the order of 1 ion per day. The PTMS techniques currently used for rare isotope measurements at LEBIT and other rare

isotope PTMS facilities are destructive. While these methods are quite robust, they require a significant number of detected ions ($\sim$ 100 ions) to complete a measurement making it difficult to perform mass measurements when the production rates are extremely low. To measure these exotic isotopes produced at such low rates, LEBIT has developed a new highly-sensitive single ion Penning trap (SIPT). SIPT uses the non-destructive narrowband Fourier transform ion cyclotron resonance (FT-ICR) technique [64], which will be discussed in Chapter 2. While this technique is widely used at other facilities, it has never been employed for mass measurements of rare isotopes. SIPT will enable rare isotope mass measurements using a single ion with a precision ($\delta M/M \leq 10^{-6}$) that meets the requirements of nuclear structure and astrophysics studies.

Details on PTMS and the methods used to measure the cyclotron frequency such as the FT-ICR technique is covered in Chapter 2. Chapter 3 describes the projectile fragmentation process, the delivery of rare isotopes to LEBIT, and the LEBIT facility. In Chapter 4, the discovery of the deformed double shell closure at $N = Z = 40$ through the mass measurement of ^{80}Zr is presented. Finally, the development and commissioning of SIPT is discussed in Chapter 5.

Chapter 2

Penning Trap Mass Spectrometry

2.1 Penning Trap Basic Concepts

2.1.1 Trapping Fields

The Penning trap combines a homogeneous magnetic field and a quadrupolar electrostatic field to trap a charged particle in three dimensions. The magnetic field provides radial confinement of an ion and causes it to precess, provided that the ion has some velocity perpendicular to the magnetic field, at the cyclotron frequency

$$\omega_c = 2\pi\nu_c = \frac{qB}{m} \tag{2.1}$$

where q is the charge of the ion, m is the mass of the ion, and B is the magnetic field strength. Axial confinement of the ion is achieved with the electrostatic quadrupolar field. The electrostatic field is produced using a set of three hyperbolic electrodes: two endcaps and a ring electrode (see Fig. 2.1 (Left)), which obey the equations of a hyperboloid of revolution. In cylindrical coordinates (ρ, z), these equations are

$$z^2 - \frac{\rho^2}{2} = \pm z_0^2 \tag{2.2}$$

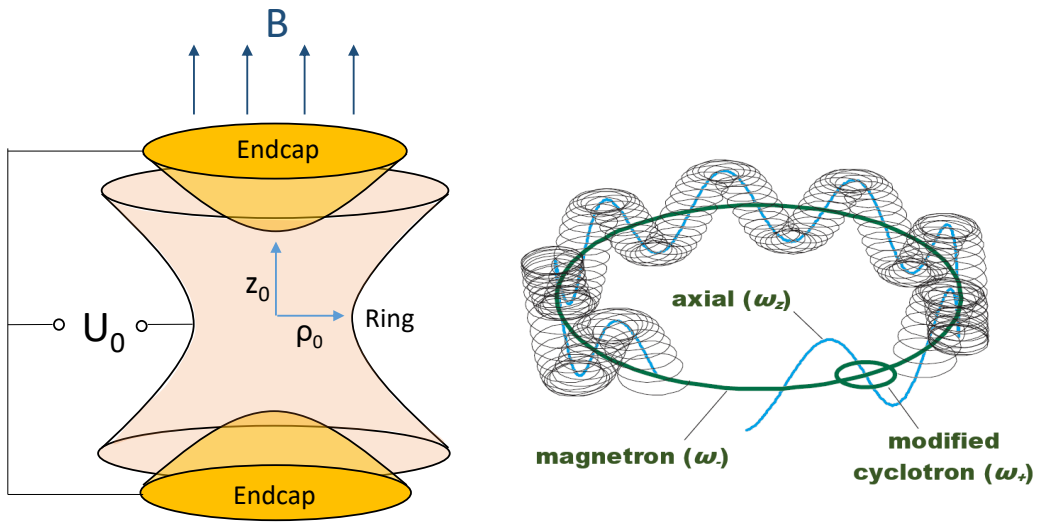

Figure 2.1: Schematic of a hypberolic Penning Trap (Left) and the three characteristic eigenmotions (Right).

where z_0 is half of the minimum distance between the end cap electrodes. The electrostatic quadrupole potential created by these three electrodes is given by

$$V(\rho, z) = \frac{U_0}{4d^2}(2z^2 - \rho^2), \tag{2.3}$$

where U_0 is the potential difference between the endcap and ring electrodes, and d is a characteristic trap parameter defined as $d = \sqrt{\rho_0^2/4 + z_0^2/2}$. The quantity ρ_0 refers to the minimum radius of the ring electrode. For high precision mass measurements, compensation electrodes must be added to the Penning trap in order to minimize frequency shifts due to higher-order electric field contributions [65]. Other Penning trap electrode geometries, such as cylindrical traps, can also be used to sufficiently approximate a quadrupolar electric field [66].

2.1.2 Ion Motion in a Penning Trap

A summary of the motion of an ion in a Penning trap will be presented here. For a full derivation, see [67], for example. In the axial direction, parallel to the magnetic field (typically defined as the z-direction), the electric field produces a harmonic oscillator system which causes the ion to precess at the frequency

$$\omega_z = 2\pi\nu_z = \sqrt{\frac{qU_0}{md^2}}. \tag{2.4}$$

In the radial direction, the magnetic and electric fields produce two additional eigenfrequencies $\omega_\pm$:

$$\omega_\pm = 2\pi\nu_\pm = \frac{\omega_c}{2} \pm \sqrt{\frac{\omega_c^2}{4} - \frac{\omega_z^2}{2}}. \tag{2.5}$$

Fig. 2.1 (Right) shows the three eigenmotions for an ion in a Penning trap.

The three eigenfrequencies satisfy a few relationships:

$$\omega_c = \omega_+ + \omega_-, \tag{2.6}$$

$$\omega_c = \sqrt{\omega_+^2 + \omega_-^2 + \omega_z^2}. \tag{2.7}$$

Both equations can be used to determine the mass of an ion. Eq. 2.6 only applies to an ideal Penning trap with no field misalignments or distortions. However, it has been demonstrated that this relationionship is still suitable for high precision measurements in a Penning trap without having to introduce additional systematic uncertainties [68]. Eq. 2.7, known as the invariance theorem [69], is insensitive to misalignments or distortions and is used in the highest accuracy Penning trap measurements [54]. For a typical Penning trap with a strong

magnetic field and weak electrostatic field, the frequencies follow a hierarchy:

$$\omega_+ \gg \omega_z \gg \omega_-. \tag{2.8}$$

The motion of an ion in a Penning trap can be manipulated by applying radio frequency (rf)-excitations to the ring electrode [6]. The ring electrode can be segmented into several components allowing for multiple excitation schemes. Figure 2.2 shows two common excitation schemes used at PTMS facilities. A dipole excitation at one of the ion's radial eigenfrequencies drives the radius of the excited eigenmotion $\rho_\pm$. This technique is useful for removing contaminant ions in the trap. An excitation at the contaminant ion's reduced cyclotron frequency ν_+ can cause the ion to collide with the trap electrodes or drive it to a large enough orbit preventing it from escaping the trap upon ejection. A quadrupole excitation at the sum or difference of the two radial eigenfrequencies couples the two eigenmotions together. A common technique used in Penning trap mass spectrometry is a quadrupole excitation at $\nu_c = \nu_+ + \nu_-$. This excitation is used to convert magnetron motion into reduced cyclotron motion.

2.2 PTMS Basics

Penning trap mass spectrometry (PTMS) is currently the most precise method for measuring an ion's mass because of the well controlled environment provided by the trap. In PTMS, the mass of an ion is obtained by determining the ion's cyclotron frequency ν_c. The cyclotron frequency can be determined with eq. 2.6, which requires a measurement of the two radial eigenfrequencies or their sum. It can also be determined with the invariance theorem

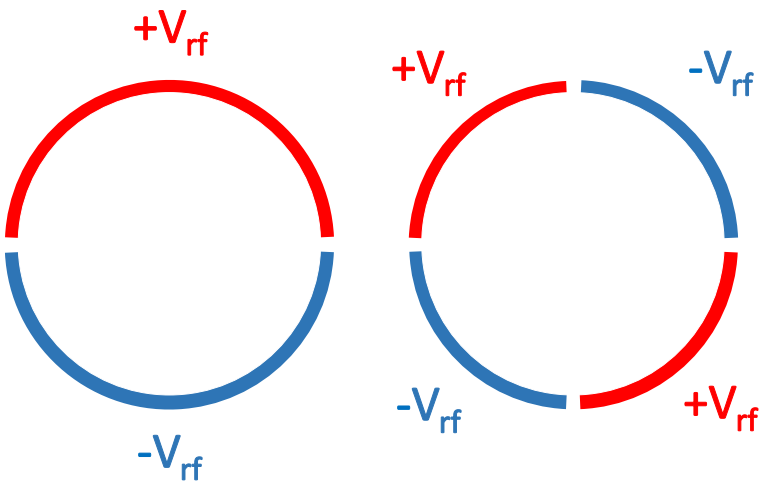

Figure 2.2: Diagram of two common rf-excitation schemes being applied to the segmented ring electrode: a dipole excitation (Left) and a quadrupole excitation (Right).

(eq. 2.7), which requires a measurement of all three eigenfrequencies. In either case, q and B must be know. A measurement of the mass-to-charge ratio m/q provides the charge state of the ion. The magnetic field strength B is determined through calibration measurements of an ion with a well known mass. The quantity of interest for extracting the mass of the ion is the ratio of frequencies

$$R = \frac{\nu_{c,\mathrm{ref}}^{int}}{\nu_c} \tag{2.9}$$

where $\nu_{c,\mathrm{ref}}^{int}$ is the cyclotron frequency from the reference measurements, which is typically linearly interpolated to the time of the measurement of the ion of interest's cyclotron frequency ν_c using reference measurements taken before and after the ν_c measurement. The mass m of the stable particle is then given by

$$m = \frac{q}{q_{\mathrm{ref}}} \cdot \bar{R} \cdot [m_{\mathrm{ref}} - q_{\mathrm{ref}} \cdot m_e] + q \cdot m_e \tag{2.10}$$

where $\bar{R}$ is the average over several frequency ratio measurements, m_e is the mass of the electron, and q_{ref} and m_{ref} are the charge and mass of the reference ion respectively. Electron

binding energies, typically ~ 10 eV, must also be included in very high-precision measurements. The relative uncertainty of a Penning trap measurement is given by

$$\frac{\delta m}{m} = \frac{\delta \nu_c}{\nu_c} = \frac{\gamma}{\nu_c \cdot T \cdot \sqrt{N}} \tag{2.11}$$

where T is the observation time determined by the measurement technique, N is the number of detected ions, and γ is a system-dependent value.

There are currently three well-established techniques used to measure the needed frequencies in eq. 2.9: Time-of-Flight Ion Cyclotron Resonance (TOF-ICR), Fourier Transform Ion Cyclotron Resonance (FT-ICR), and Phase Imaging Ion Cyclotron Resonance (PI-ICR). The first two methods will be discussed in detail below. The latter method, PI-ICR, will be summarized here.

In PI-ICR, the radial frequencies are determined through measurements of the accumulated angular phase of an ion in a Penning trap [70]. An initial and final phase are measured before and after some amount of accumulation time T_{acc} with a position sensitive detector outside the trap. The phase difference divided by the accumulation time T_{acc} allows for the extraction of the frequency. The observation time in eq. 2.2 for PI-ICR is T_{acc}.

2.3 TOF-ICR Technique

The TOF-ICR technique takes advantage of the ion's radial energy gain when its initial magnetron motion is converted to reduced cyclotron motion through a quadrupole excitation at the ion's cyclotron frequency ν_c. Because $\omega_+ \gg \omega_-$, the ion gains maximal energy when a full conversion of pure magnetron motion to pure reduced cyclotron motion occurs. The

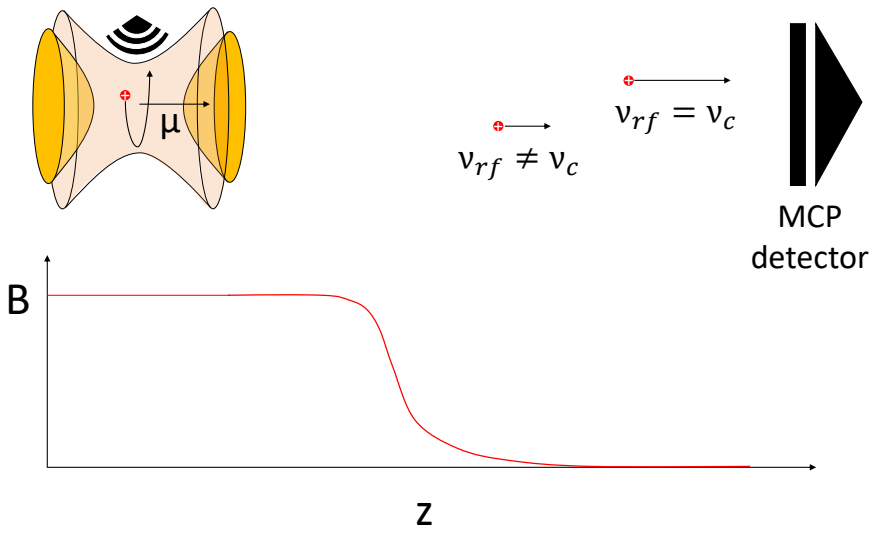

Figure 2.3: Illustration of the TOF-ICR measurement technique. The radial energy gained due to the quadrupole rf-excitation is converted to axial energy. Ions excited at their cyclotron frequency $\nu_{rf} = \nu_c$ gain more energy than ions excited at a different frequency $\nu_{rf} \neq \nu_c$. An MCP detector is used to measure the ions' time of flight. Figure adapted from [5].

radial energy gained ΔE_r by an ion with initial magnetron radius ρ and no initial reduced cyclotron radius is

$$\Delta E_r = \frac{1}{2} m(\omega_+^2 - \omega_-^2)\rho^2. \tag{2.12}$$

There are several ways to prepare the ions with an initial magnetron motion. One method is to inject the ions at the center of the trap and then drive the magnetron motion with a dipole rf-excitation. Another method, developed at LEBIT, is to use so-called Lorentz steerers [71], a set of steering electrodes placed just before the entrance to the trap that produce an electric field perpendicular to the magnetic field. The achieved $\vec{E} \times \vec{B}$ force steers the ions off the central axis of the trap providing the magnetron motion. To minimize any initial reduced cyclotron motion pick-up, ions must enter the magnetic field with minimal velocity perpendicular to the magnetic field.

After the rf-excitation, ions are ejected from the trap by lowering one of the endcap

voltages. As the ions leave the trap, they move from an area of strong magnetic field to an area with no magnetic field. The magnetic field gradient $\partial B/\partial z$ the ions pass through leads to a force on the ions in the axial or z-direction:

$$F_z = -\mu \left(\frac{\partial B}{\partial z} \right) = -\frac{E_r}{B_0} \left(\frac{\partial B}{\partial z} \right), \tag{2.13}$$

where μ is the magnetic dipole moment of the orbiting charged particle with radial energy E_r in a central magnetic field of strength B_0 [72]. This force converts the radial kinetic energy pickup due to the rf-excitation to axial kinetic energy. A microchannel plate (MCP) detector is placed at the exit of the magnet to measure the time of flight (TOF) of the ions from the trap to the detector. The TOF is then minimal, when the kinetic energy pickup is maximal. Thus, one can scan the rf-excitation frequency ν_{rf} while measuring the TOF and search for a minimum in the TOF which occurs when $\nu_{rf} \approx \nu_c$. This technique requires ≥ 100 detected ions to produce the characteristic resonance response seen in Fig. 2.4. The fit to the data in Fig. 2.4 is determined by numerically solving for the time of flight of the ion at each excitation frequency ω_{rf} [6]:

$$T(\omega_{rf}) = \int_{z_0}^{z_1} \left(\frac{m}{2[E_0 - q \cdot V(z) - \mu(\omega_{rf}) \cdot B(z)]} \right)^{\frac{1}{2}} dz \tag{2.14}$$

where E_0 is the total initial energy of the ion, q is the charge of the ion, $V(z)$ is the electric potential along the ion's path to the MCP, and $B(z)$ is the magnetic field strength along the ion's path.

The quadrupole rf-excitation amplitude V_{rf} and duration T_{rf} must be tuned in order to achieve a complete conversion of initial magnetron motion to reduced cyclotron motion.

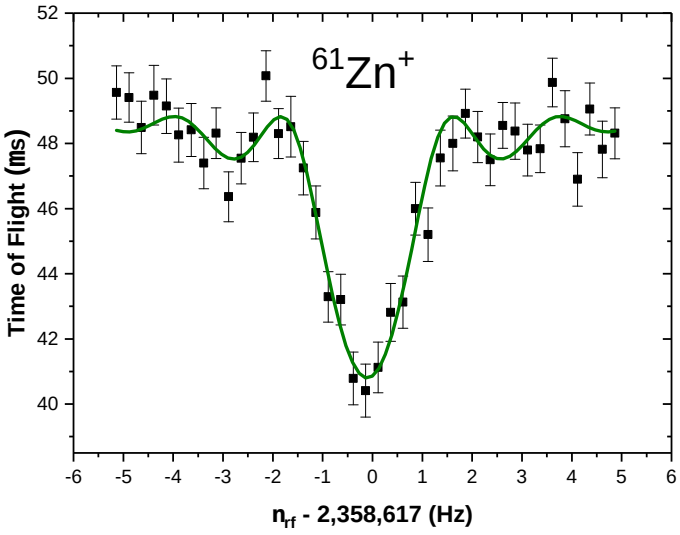

Figure 2.4: Example of a 500 ms TOF-ICR resonance obtained by scanning the applied quadrupole rf-excitation frequency and measuring the ions' time of flight to an MCP detector. The green curve is a theoretical fit [6] to the data. The minimum of the fit corresponds to the cyclotron frequency ν_c. Figure adapted from [7].

Once one set of V_{rf} and T_{rf} values has been determined, the excitation duration T_{rf} can be scaled in a simple way as the product $V_{rf} \cdot T_{rf}$ for a complete conversion is constant. This scaling is important for increasing the precision of the measurement. The relative uncertainty of a TOF-ICR measurement is given by eq. 2.2 where the observation time T is the excitation duration T_{rf}.

2.4 FT-ICR Technique

In the FT-ICR technique, the image current produced by ions in a Penning trap is detected on the trap electrodes [64]. The detected oscillatory signal will be a superposition of noise and ion image currents. A Fast Fourier Transform (FFT) is performed on the time-domain signal to produce a frequency-domain spectrum [73]. The image currents produced by the ions will appear as distinct peaks in the frequency domain, which can be fit to determine

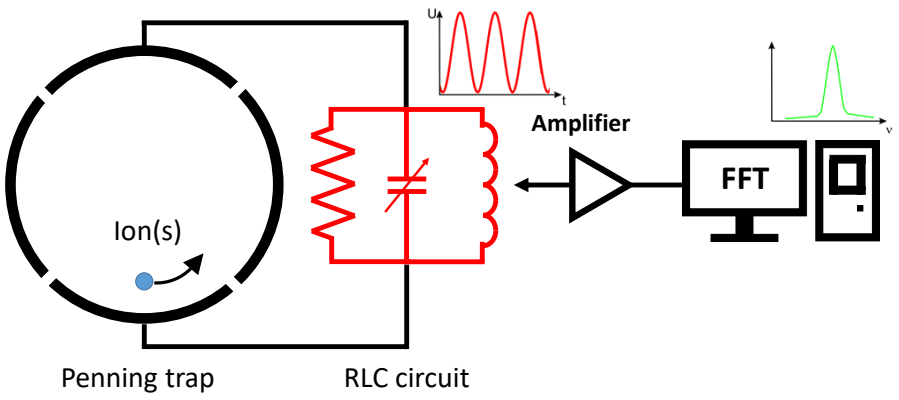

Figure 2.5: Schematic illustration of the narrowband FT-ICR detection technique. The RLC resonator circuit suppresses noise while amplifying signals with frequencies near the resonator frequency $\nu \approx \nu_{circ}$.

the frequency of the ions' motion.

This technique is commonly used to identify molecules in a sample. Because these molecules typically have many different mass-to-charge ratios, a broadband detection technique is used meaning that the observation is performed over a large range of frequencies to capture the various peaks created by the various ions in the trap. This technique works well with a large number of ions and when precision is not needed. However, for a precision measurement, the number of ions in the trap must be limited to avoid systematic frequency shifts due to ion-ion interactions [74]. The image current produced by a single ion in a Penning trap is on the order of picoamperes, so a highly sensitive detection technique is needed to be able to separate the ion signal from the noise.

The narrowband FT-ICR technique provides the needed sensitivity to perform precision measurements with a single ion [72]. The detection principle is illustrated in Fig. 2.5. The Penning trap electrodes used for the image current detection are connected in parallel with an

inductor to create an RLC resonator circuit. The pickup electrodes along with any additional added capacitance combine to give the total capacitance of the system C. The resistance R is the equivalent resistance of all components in the circuit. The detected voltage produced by the ions' image current I across the RLC circuit is given by Ohm's law to be $V = IZ$ where Z is the impedance of the circuit. The absolute value of the impedance for the RLC circuit is

$$|Z(\omega)| = \frac{1}{\sqrt{(1/R)^2 + (1/\omega L - \omega C)^2}} \tag{2.15}$$

where ω is angular frequency of the ion's image current. This quantity is maximum at the resonant frequency of the circuit:

$$\omega_{circ} = \frac{1}{\sqrt{LC}}. \tag{2.16}$$

The resonator can be tuned so that ω_{circ} is approximately equal to the frequency of the ion motion to be detected by choosing appropriate values for L and C. Impedances on the order of 10 MΩ are achievable with a well-tuned circuit leading to measurable voltages. An example FT-ICR resonance is shown in Fig. 2.6 along with a Lorentzian fit to the data.

The detection circuit required to be able to detect the image charge created by a single, singly-charged ion must be very sensitive. The relevant value that needs to be optimized to achieve this goal is the signal-to-noise ratio S/N. In this case, the S/N is the ratio of the root mean square (RMS) voltage signal generated in a narrowband FT-ICR detection circuit to the RMS Johnson-Nyquist noise [75]. This ratio is given by

$$S/N = \kappa \frac{\sqrt{\pi}}{4} Nq \left(\frac{\rho}{\rho_0}\right) \sqrt{\frac{\nu}{\Delta\nu}} \sqrt{\frac{Q}{k_B T C}} \tag{2.17}$$

where κ is a geometrical parameter that accounts for the fact that the pickup electrodes

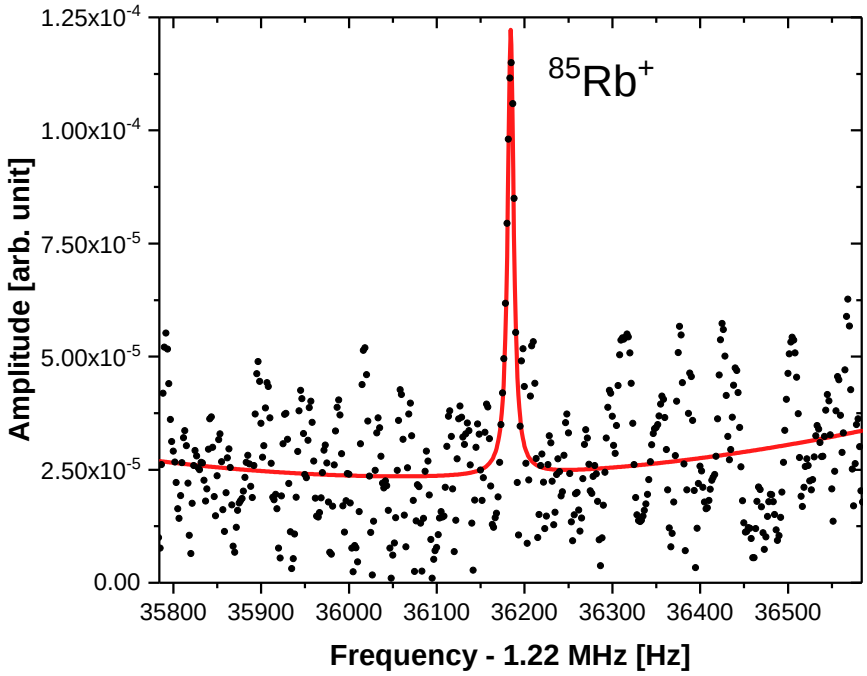

Figure 2.6: FT-ICR resonance of the ν_+ frequency of $^{85}Rb^+$.

are not infinite flat planes; N is the number of ions; q is the ion charge; ρ/ρ_0 is the radius of the ions' orbit relative to the trap radius; $\nu/\Delta\nu$ is the ratio of the ion frequency to the spectral bandwidth; k_B is the Boltzmann constant; and Q, T, and C are the quality factor, temperature, and capacitance of the detection circuit respectively [72, 76].

The key to reaching adequate S/N lies in optimizing the RLC circuit. In particular, the quality factor of the circuit, Q, defined as

$$Q = \frac{\nu_{circ}}{\Delta\nu_{circ}} \tag{2.18}$$

must be ~ 1000 or greater. Here $\Delta\nu_{circ}$ is the full width at half maximum (FWHM) of the resonator response in the frequency domain. For SIPT, the high Q-factor is achieved with a superconducting inductor coil. Hence, SIPT must be operated at cryogenic temperatures

(~ 5 K). The cryogenic temperatures also provide the advantage of low thermal noise leading to an improvement in S/N by a factor of 8 compared to room temperature. Alternatively, high Q-factors can be achieved at room temperatures using a quartz crystal in place of an inductor coil [77].

The geometry of the electrodes used to detect the ion signal also plays a role in the signal strength. The ion's image current I can be calculated as [76]

$$I = q\vec{v} \cdot \vec{E_1} \tag{2.19}$$

where q is the ion's charge, $\vec{v}$ is the ion's velocity, and $\vec{E_1} = \vec{E}/V$ is the unit electric field generated by a ± 1 V potential difference on the detection electrodes. If the ion signal is being detected off the ring electrodes, then similar couplings that were seen with the rf-excitations apply to the ion motion pickup. A dipole detection scheme like that in Fig. 2.2 (Left) is optimal for detecting the individual radial eigenfrequencies while a quadrupole detection scheme like that in Fig. 2.2 (Right) is optimal for detecting sum or differences of the radial eigenfrequencies. A more detailed study of the detection scheme's effect on the signal strength will be presented in Chapter 5. The relative uncertainty of an FT-ICR measurement is that of eq. 2.2 with the observation time T replaced with the acquisition time T_{acq}, or how long the signal is measured.

Chapter 3

The LEBIT Mass Spectrometer Facility at the NSCL

The Low Energy Beam and Ion Trap (LEBIT) facility is located at the National Superconducting Cyclotron Laboratory (NSCL) on the campus of Michigan State University. The NSCL is home to the Coupled Cyclotron Facility (CCF), a projectile fragmentation radioactive ion beam facility, which can deliver rare isotope beams to LEBIT. An overview of the CCF and LEBIT facility is presented here.

3.1 CCF as a Rare Isotope Beam Source

The CCF consists of two superconducting cyclotrons, the K500 and K1200, which are used to accelerate ion beams to speeds around half the speed of light. The primary beams are produced with electron-cyclotron resonance (ECR) ion sources and injected into the smaller K500 cyclotron. The K500 accelerates the primary beam to energies on the order of 10 MeV/u. Upon extraction, the beam is sent into the larger K1200 cyclotron where a charge stripper foil located near the center of the cyclotron is used to strip most of the remaining electrons from the beam. The K1200 accelerates the highly charged primary beam to an energy on the order of 100 MeV/u. The fast primary beam is then impinged on a production target typically made of beryllium to produce a plethora of rare isotopes via projectile

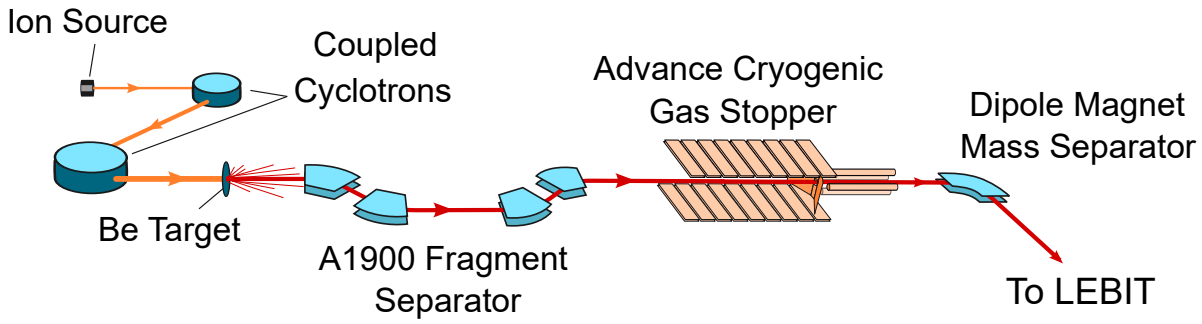

Figure 3.1: Schematic of the main components of the Coupled Cyclotron Facility that are relevant for the experiment discussed in this thesis.

fragmentation reactions. To isolate the rare isotope of interest, the secondary beam is sent to the A1900 fragment separator [78].

The main components of the A1900 fragment separator are four dipole magnets and an energy degrading wedge. The rare isotope of interest is initially selected by its magnetic rigidity $B\rho = p/q$ using the first two dipole magnets where B is the magnetic field strength of the dipole, ρ is the radius of the ion's motion, p is the momentum of the ion, and q is its charge. Isotopic selection is completed by passing the ions through the energy degrading wedge, which leads to momentum spread based on the atomic number of the ion. A final magnetic rigidity selection is made using the second set of dipole magnets to isolate the rare isotope of interest. This secondary beam can then be delivered to any of the experimental stations at the lab. LEBIT is located in the low-energy beam area. The low energies are achieved with the gas stopping facility. A schematic of the coupled cyclotrons as well as the A1900 and the relevant components of the gas stopping facility for this thesis is shown in Fig. 3.1.

The gas stopping facility at the NSCL is critical for LEBIT experiments because it reduces the energy of the rare isotope beam to a level compatible with injection into LEBIT's Penning

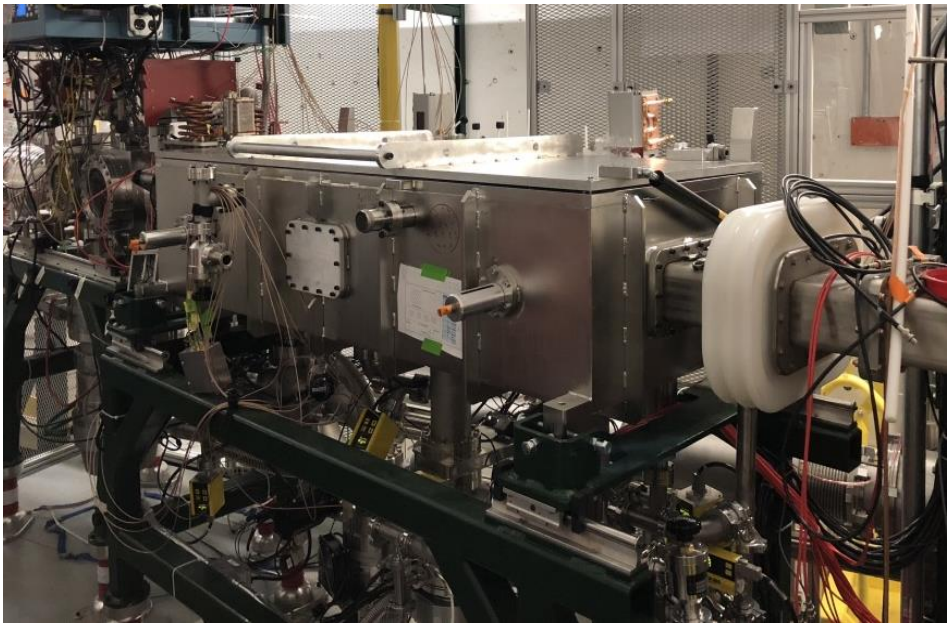

Figure 3.2: Image of the Advance Cryogenic Gas Stopper.

traps. At the NSCL, there are three helium-filled gas stoppers: the Argonne National Laboratory (ANL) cell [79]; the Advanced Cryogenic Gas Stopper (ACGS) [80]; and the Cyclotron Gas Stopper [81], which is currently being commissioned. An overview of ACGS, seen in Fig. 3.2, is presented here.

Before entering ACGS, the radioactive ion beam from the A1900 passes through a set of adjustable aluminum degraders used to remove most of the beam's kinetic energy. The ions are then stopped within ACGS through collisions with the ultra high purity helium buffer gas. Charge exchange reactions with the gas lower the ions' charge states to the 1+ or 2+ state. The cryogenic temperatures help reduce molecular recombination within the gas cell that can heavily contaminate beams extracted from gas cells. An electrode structure inside the gas cell is used to repel the ions from collisions with the walls of the cell and transport them to the exit of the gas cell. The ions then enter a three-stage radiofrequency quadrupolar (RFQ) ion guide which allows for differential pumping between the gas cell and

the beamline following the gas cell. Ions are transported through the RFQ ion guide with a combination of rf-quadrupole fields that confine ions radially and DC electrostatic fields that control the ions' axial motion.

ACGS sits on a high-voltage platform in order to accelerate ions after extraction from the ion guide and transport them to the low-energy experimental area. Ions are typically extracted at energies of 30 keV/Q. Before the low-energy experimental area, the beam passes through a dipole magnet, which allows for mass-to-charge (A/Q) separation. At this point, the low-energy beam can be sent to the LEBIT facility.

The NSCL was recently shut down to allow for the transition to the next-generation ion beam facility, the Facility for Rare Isotope Beams (FRIB). FRIB will be complete in spring 2022 and ready for user operation. With increased production rates and number of accessible rare isotopes, FRIB will allow for groundbreaking nuclear physics research to continue at MSU for the forseeable future.

3.2 Major Components of the LEBIT Facility

The layout of the LEBIT facility is shown in Fig. 3.3. Beam from the gas stopping facility is transported to LEBIT at a typical energy of 30 keV/Q. The LEBIT facility sits on a high-voltage (HV) platform that shares a power supply with the gas stopping facility's HV platform. This HV coupling removes the majority of the beam's energy as it enters LEBIT. A separate DC power supply coupled only to LEBIT allows for fine tuning of the incoming beam's energy. Upon entering LEBIT, an electrostatic deceleration section is used to prepare ions for injection into the LEBIT cooler and buncher [82]. LEBIT's offline ion sources are placed within this deceleration section as well. The cooler and buncher pulses the DC beam

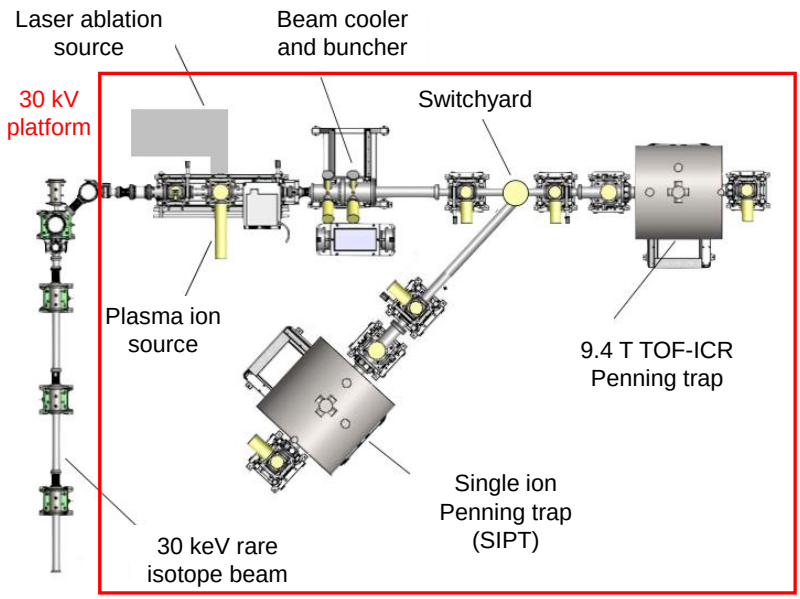

Figure 3.3: Layout of the LEBIT facility. Figure taken from [8].

from the gas stopping facility or offline ion sources. The ion pulses can then be sent either to the 9.4 T Penning trap [83] or around a 115° bend to the single ion Penning trap [8]. Beam observation boxes (BOBs) are placed throughout the LEBIT beamline. The BOBs typically contain Faraday cups to measure DC current as well as micro-channel plate (MCP) detectors and phospher screens, which are used to view the shape of the beam.

3.2.1 Offline Ion Sources

LEBIT is equipped with two offline ion sources, a Colutron plasma ion source, typically referred to as the thermal ion source (TIS), and a laser ablation source (LAS) [84]. The offline ion sources provide ions for development projects, beamline tuning and diagnostic studies, reference measurements to calibrate the magnetic field, and mass measurements of long-lived radioisotopes. The TIS, displayed in Fig. 3.4 (Left), consists of a tungsten filament that is heated to produce electrons and negatively biased to produce a discharge. The discharge can

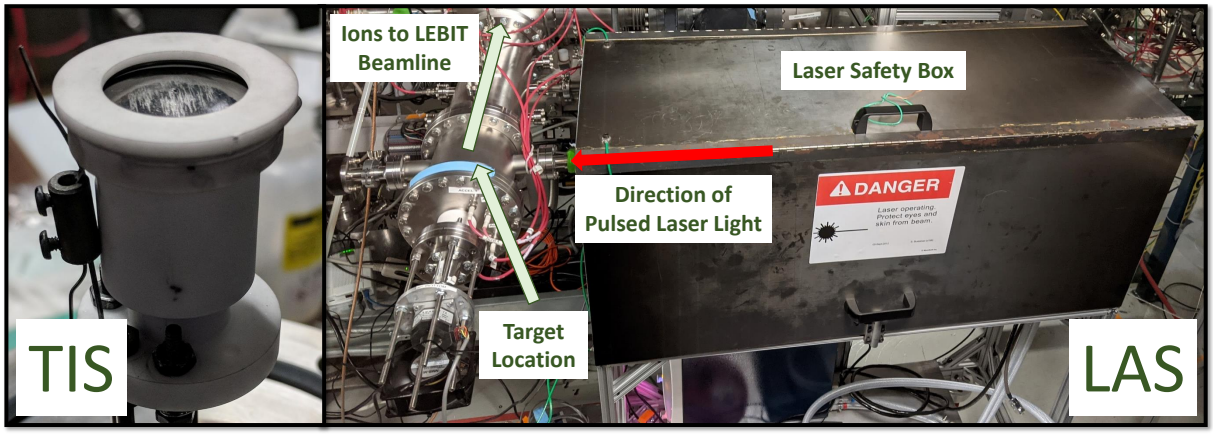

Figure 3.4: (Left) Photo of the Colutron plasma ion source (TIS) at the LEBIT facility. The tungsten filament sits within the white ceramic casing. (Right) Photo of the laser ablation ion source (LAS) at the LEBIT facility. The Nd:Yag laser sits within the laser safety box.

be used to ionize gaseous atoms of the desired species, which are introduced to the chamber through a leak valve. The filament can also be positively biased to provide alkali metal ions via surface ionization from impurities in the filament. The TIS produced the $^{41}K^{+}$ and $^{85,87}Rb^{+}$ ions that were used as reference ions in the $^{80-83}Zr$ experiment (Chapter 4), as well as the $^{84}Kr^{+}$ and $^{85}Rb^{+}$ ions that were used to commission SIPT (Chapter 5). The LAS uses a pulsed Nd:YAG Quantel Brilliant laser to produce light pulses which irradiate a target producing ions. The LAS has been used to perform high-precision offline measurements of scientific importance including recent measurements of ^{138}La [85] and ^{139}La, ^{89}Sr [86] for β-decay studies. A photograph of the LAS component of the beamline is shown in Fig. 3.4 (Right).

3.2.2 Cooler and Buncher

The LEBIT cooler and buncher is a three-staged gas-filled linear Paul trap used to convert continuous ion beams from the gas stopping facility or offline ion sources into short pulses for

injection into the Penning traps [82]. The three linear Paul traps use a similar mechanism for transporting ions as the RFQ ion guide after ACGS: an RFQ quadrupolar field confines ions radially while a DC electrostatic field controls the ions' axial motion. The buffer gas, typically helium, cools the ions' excess energy and brings them into thermal equilibrium with the gas. The DC axial field then pulls the ions through the buffer gas for extraction. This process removes any systematic effects that could result from the extraction of the beam from its source.

The first stage of the cooler and buncher is known as the pre-cooler and is responsible for dissipating most of the ions' energy. The second stage is the micro-RFQ, which connects the pre-cooler to the final buncher stage and provides the necessary differential pumping between these stages. The final buncher stage accumulates and thermalizes the ions before releasing them as short low-emittance pulses. For optimal capture, a voltage-pulsed drift tube after the cooler and buncher is used to adjust the energy of the ions to match the Penning trap's minimum DC potential. After passing through the pulsed drift tube, the ions are sent either to the 9.4 T Penning trap or the single ion Penning trap.

3.2.3 9.4 T Penning Trap

Before entering the 9.4 T Penning trap, ions pass through a time-of-flight gate used to allow ions of a certain A/Q ratio to enter the trap. The time-of-flight gate is produced by an electrostatic steering element that is grounded for $\sim$ 50 ns when ions of a given A/Q are passing through the filter and set to 1 kV at all other times. Just before the magnet, several Einzel lenses are used for final focusing prior to the beam's injection into the magnet. A series of injection optics guide the ions through the magnetic field and reduce their energy for optimal capture in the Penning trap. A set of Lorentz steerers [71] are placed just before

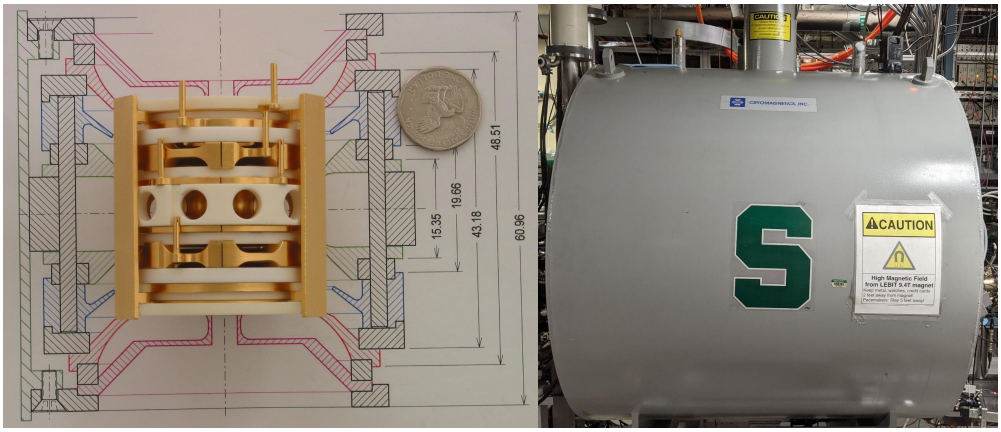

Figure 3.5: Image of the 9.4 T Penning trap. The Penning trap electrodes are shown on the left with a US $1 coin for scale. The 9.4 T magnet is displayed on the right.

the Penning trap electrode structure to prepare ions with an initial magnetron orbit for the TOF-ICR measurement technique.

The 9.4 T Penning trap, displayed in Fig. 3.5, consists of a hyperbolic electrode structure with additional correction ring and tube electrodes used to approximate the quadrupolar electrostatic potential [83]. Holes in the endcap and correction tube electrodes allow for injection and ejection from the Penning trap. The trap electrodes are made of high-conductivity copper and plated with gold to reduce patch effects caused by oxidation.

Upon ejection from the Penning trap, ions pass through another series of drift tubes that accelerate the ions to an MCP detector which is mounted in a Daly configuration [87] outside of the magnet. The positive ions are guided towards the more negatively biased Daly collector. An electron shower created by the ions' collision with the collector is detected on the MCP.

3.2.4 Single Ion Penning Trap

The single ion Penning trap (SIPT) beamline is located after the cooler and buncher allowing access to beams from the CCF and offline ion sources. The SIPT beamline and Penning trap as well as simulation and experimental results are discussed in detail in Chapter 5.

Chapter 4

Mass Measurement of the Lightweight Self-conjugate Nucleus ^{80}Zr

The results presented in this chapter were recently accepted in Nature Physics [26]. Portions of the text and several of the figures presented here are reproduced with permission from Springer Nature. Additional details and discussion are included as well.

4.1 Motivation for Mass Measurement of ^{80}Zr

The mass of an isotope is a sensitive indicator of the underlying shell structure as it reflects the net energy content of the nucleus, including its binding energy. Hence, doubly-magic nuclei are significantly lighter, or more bound, relative to their neighbors. Due to a lack of precision mass measurement data on ^{80}Zr and its surrounding nuclei, it is difficult to characterize the size of the shell effect responsible for the large deformation of ^{80}Zr discussed in Chapter 1. To this end, high precision Penning trap mass spectrometry was performed on four neutron-deficient zirconium isotopes – $^{80\text{-}83}$Zr. The local trends of the binding-energy surface were analyzed by studying several binding-energy indicators. To quantify the findings, experimental patterns have been interpreted using global nuclear mass models augmented by a Bayesian model averaging (BMA) analysis [38].

4.2 Experimental Procedure

The radioactive Zr isotopes were produced at the National Superconducting Cyclotron Laboratory's Coupled Cyclotron Facility via projectile fragmentation of a 140 MeV/u ^{92}Mo primary beam that was impinged on a 564 mg/cm^2 Be target. The produced Zr nuclei were separated from other fragments by the A1900 Fragment Separator [78] and sent to the Advanced Cryogenic Gas Stopper [80], where they were stopped as ions. The ions were extracted from the gas stopper as a low energy (30 keV/Q) continuous beam and selected by their mass-to-charge ratio (A/Q) using a dipole magnet. The optimal A/Q was determined using a silicon detector after the dipole magnet. The A/Q was scanned while measuring radioactivity on the silicon detector. Radiation was observed at A/Q values corresponding to singly charged zirconium ions, doubly charged zirconium ions, and singly charged zirconium-oxide moleculer ions. The relative amounts of radiation at each extraction state for each isotope were the same as the isotopes all share the same chemical properties. ^{80,82}Zr ions were measured in the singly charged oxide sate ($A/Q = 96, 98$ respectively); ^{81,83}Zr ions were measured bare and doubly charged ($A/Q = 40.5, 41.5$ respectively). The reasoning for these choices is discussed below.

The ions were then sent to the LEBIT facility [62]. Upon entering LEBIT, the ions first passed through the cooler and buncher [82] where they were accumulated, cooled, and released as ∼100 ns low-emittance bunches to the LEBIT 9.4 T Penning trap [83]. Before entering the trap, the pulses were purified using a time-of-flight filter to only allow ions with a specific mass-to-charge ratio to enter the trap. Once captured in the trap, ions were further purified using targeted dipole cleaning [88] and the stored waveform inverse Fourier Transform (SWIFT) technique [89]. All measurements were performed using the TOF-ICR

method [6]. The reference ions were produced using the LEBIT Colutron ion source and chosen as singly ionized species of widely available stable alkali atoms whose masses (m_{ref}) are well known in the literature [1], as well as whose A/Q was close to the ion of interest to avoid large mass-dependent systematic shifts in the calibration procedure. Eq. 2.9 was used to extract a frequency ratio for each measurement of the ion of interest. As explained in Chapter 2, each measurement of the ion of interest's cyclotron frequency ν_c was interleaved by measurements of the cyclotron frequency of the reference ion, $\nu_{c,\mathrm{ref}}$. The masses of each ion of interest were then calculated through Eq. 2.10 using the average of multiple frequency ratios ($\bar{R}$) weighted by their uncertainties.

Uncertainties related to the extraction of cyclotron frequencies from the fits dominate the statistical error budget. Systematic errors arising from magnetic field inhomogeneities, trapping potential imperfections, and a possible misalignment between the trap and magnetic field [76] result in a shift on the average frequency ratio that scales linearly with the difference in mass-to-charge ratio between the ion of interest and the reference ion. These A/Q-dependent shifts in $\bar{R}$ have been measured at the LEBIT facility and found to be $\Delta\bar{R} = 2(2) \times 10^{-10}/(\mathrm{u/q})$ [90] where u/q is the mass-to-charge ratio difference.

Other systematic errors on the individual measured frequency ratios R must be taken into account separately. Nonlinear magnetic field fluctuations in time can result in calibration errors. This effect has been studied at LEBIT and leads to a shift in R at a level below 1×10^{-9} per hour [91]. Measurement times ranged from three hours for ^{80}Zr to fifteen minutes for ^{83}Zr. This uncertainty was folded into the ratio uncertainties though it had a negligible effect on the final error estimate. Special relativity can have an effect on the cyclotron frequency ratios [67], however this error was negligible compared to the statistical uncertainty. Ion-ion interactions were first minimized using the purification techniques

described above. Additional ion-ion interactions were taken into account by performing a count-rate class analysis on each data set whenever possible [92]. Finally, Birge ratios were calculated to determine if the uncertainties were underestimated. The Birge ratio is the ratio of the outer to the the inner uncertainty [93]. A Birge ratio greater than one could indicate an underestimation of systematic uncertainties, while a Birge ratio less than one could indicate that the uncertainties have been overestimated. In the cases where the Birge ratio was greater than one, the outer uncertainty was used as the final uncertainty (e.g. the inner uncertainty was multiplied by the Birge ratio). A more detailed analysis of each isotope is given below.

4.2.1 ^{83}Zr

^{83}Zr was extracted from the gas stopper doubly charged to prevent the extraction of molecular contaminants, which are almost always singly charged. This choice provided a pure $^{83}Zr^{2+}$ beam with no measurable contamination. $^{41}K^{+}$ was chosen as a reference to reduce systematic uncertainties. The cyclotron frequencies of both $^{83}Zr^{2+}$ and $^{41}K^{+}$ were measured with the Ramsey excitation scheme [9] and a 1 s excitation time. An example 1 s Ramsey TOF-ICR resonance of $^{83}Zr^{2+}$ is shown in Fig. 4.2. A total of three measurements of the ratio R were performed. The longest measurement time was 15 minutes. Systematic shifts due to nonlinear drifts in the magnetic field are an order of magnitude lower than the measured uncertainty. The count rate was high enough to perform a count-rate class analysis on both the reference and ion of interest data sets [92]. With this technique, the data from each scan is divided into classes corresponding to the number of ions collected on the MCP. The class data is fit with a line, which is used to determine the cyclotron frequency when only one ion is present in the trap. The analysis must take into account the detection efficiency

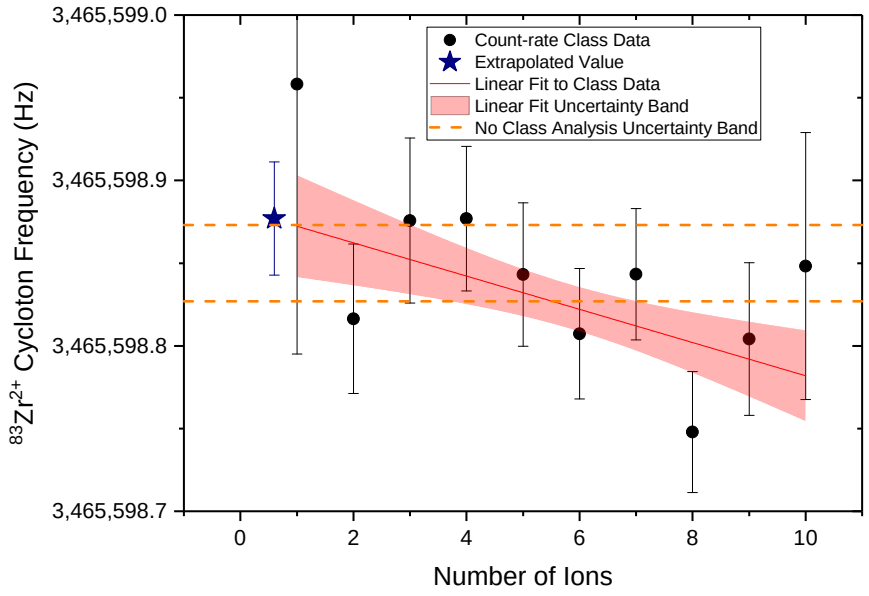

Figure 4.1: Example of a count-rate class analysis performed on a $^{83}Zr^{2+}$ TOF-ICR resonance scan. The cyclotron frequency as a function of the number of ions collected on the MCP is shown with black circles. A linear fit along with it's 1σ uncertainty band are also displayed. The extrapolated cyclotron frequency with a single ion in the trap including the MCP efficiency is indicated with a blue star. The 1σ uncertainty band for fitting the data with five ions or fewer detected ions is shown with dashed-orange lines.

of the MCP, which is ∼60% for LEBIT. An example of this procedure applied to a $^{83}Zr^{2+}$ scan is shown in Fig. 4.1. The $\pm1\sigma$ uncertainty band as a result of fitting data corresponding to five or fewer detected ions is also indicated in Fig. 4.1 by the two dashed-orange lines. The discrepancy between the measured cyclotron frequency with and without the count-rate class analysis is 0.48σ. Performing this analysis on each scan for both $^{83}Zr^{2+}$ and $^{41}K^{+}$ led to a non-negligible shift in the average ratio ($\Delta\bar{R} = 9.8(7.3) \times 10^{-9}$). Adding this shift to the average ratio along with the small shift due to the difference in A/Q between the ion of interest and the reference yielded a final weighted ratio of $\bar{R} = 1.012\,274\,829\,7(85)$. The Birge ratio for this measurement was 0.98(28) indicating that the measurement fluctuations were purely statistical.

4.2.2 ^{82}Zr

^{82}Zr was extracted from the gas stopper as a singly charged oxide molecule $^{82}Zr^{16}O^{+}$. The major contaminant identified at $A/Q = 98$ was $C_5H_8NO^{+}$. This molecule was easily cleaned with a targeted dipole excitation. $^{87}Rb^{+}$ was chosen as the reference. The cyclotron frequency of $^{82}Zr^{16}O^{+}$ was measured with 500 ms and 1 s Ramsey excitations. An example 500 ms Ramsey resonance is shown in Fig. 4.2. $^{87}R^{+}$ was also measured using the Ramsey excitation scheme with 1 s and 1.5 s excitation times. A total of six measurements of the ratio R were performed. The count rate was high enough to perform a count-rate class analysis on both data sets [92], however the result showed no shift in the measured ratio. The maximum length of time for a $^{82}Zr^{16}O^{+}$ measurement was 1.5 h, which led to a negligible shift in $\bar{R}$ due to magnetic field fluctuations. The difference in the mass-to-charge ratio between the ion of interest and reference is 11. Folding this shift into the final ratio had a negligible effect as well. The Birge ratio for this measurement was 1.45(19), so the final uncertainty was inflated by multiplication with the Birge ratio. The final weighted ratio was $\bar{R} = 1.126\,770\,338(31)$.

4.2.3 ^{81}Zr

^{81}Zr was extracted doubly charged. While this reduced the amount of contamination accompanying the ion of interest, there was still some amount of $^{40}Ar^{+}$ that passed through the dipole mass separator after the gas stopper as well as the LEBIT time-of-flight filter. Because of its much lower mass-to-charge ratio, the $^{40}Ar^{+}$ was easy to clean with a targeted dipole excitation. $^{41}K^{+}$ was chosen as the reference. The cyclotron frequency of $^{81}Zr^{2+}$ was measured with one 50 ms, two 100 ms, and one 200 ms continuous excitation as well as one 100 ms Ramsey excitation. The 200 ms continuous resonance is shown in Fig. 4.2.

The cyclotron frequency of the reference ion was measured with 500 ms quadrupole excitations. A total of five measurements of the ratio R were performed. The $^{81}Zr^{2+}$ rate was low enough that a count-rate class analysis was infeasible to perform. Indeed, $\sim 90\%$ of the data consisted of two or fewer detected ions. A count-rate class analysis was performed on the reference ion data. Comparing results with and without the count-rate analysis showed a negligible difference, so the count-rate class analysis was not used. The longest $^{81}Zr^{2+}$ resonance was ~ 3 hours. Even with this long measurement time, systematic shifts due to nonlinear drifts in the magnetic field are negligible ($\sim 3\times10^{-9}$) compared to the uncertainty on the individual ratios ($\delta R \sim 1\times10^{-7}$). The difference in the mass-to-charge ratio between the ion of interest and reference was 0.5. Folding this shift into the final ratio led had a negligible effect as well. The Birge ratio for this measurement was 1.49(21), so the final uncertainty was inflated by multiplication with the Birge ratio. The final weighted ratio was $\bar{R} = 0.987\,971\,08(13)$.

4.2.4 ^{80}Zr

^{80}Zr was extracted from the gas stopper as a singly charged oxide molecule $^{80}Zr^{16}O^{+}$. The major contaminants identified at $A/Q = 96$ were $C_7H_{12}^{+}$ and $C_2H_2Cl_2^{+}$. Both were cleaned with targeted dipole excitations. The cyclotron frequency of $^{80}Zr^{16}O^{+}$ was measured with three 50 ms and two 100 ms continuous excitations. A 50 ms resonance is shown in Fig. 4.2. Two of the three 50 ms resonances appeared to have a possible contaminant ~ 40 Hz below the cyclotron frequency of $^{82}ZrO^{+}$. These resonances were fit with a double resonance curve to account for the contaminant. This contaminant could be explained by a plethora of possible stable contaminants. The contaminant did not persist throughout the measurement unlike the $^{80}Zr^{16}O^{+}$. The count rate in the trap was extremely low (< 1 particle per minute),

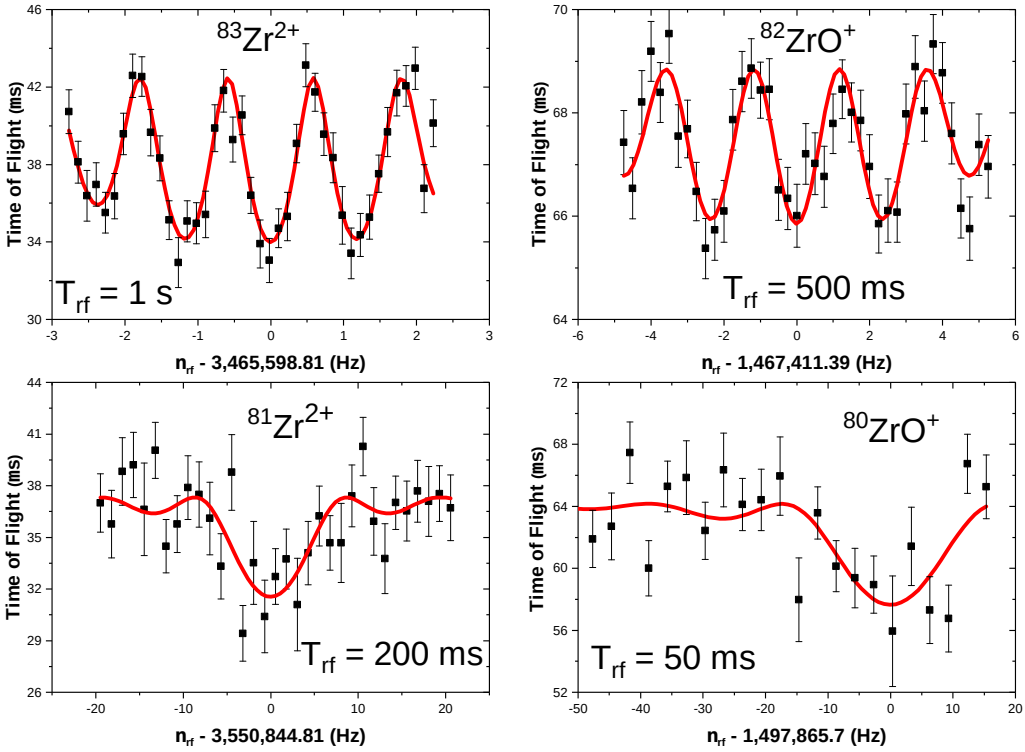

Figure 4.2: TOF-ICR resonances for $^{83}Zr^{2+}$, $^{82}ZrO^{+}$, $^{81}Zr^{2+}$, and $^{80}ZrO^{+}$. The excitation times (T_{rf}) are indicated in the figures as well. The red curves are analytical fits to the data [6, 9].

so it was difficult to determine the exact species of the contaminant. $^{85}Rb^{+}$ was chosen as a reference and measured with 500 ms Ramsey excitations. A total of five measurements of the ratio R were performed. The $^{80}Zr^{16}O^{+}$ rate was low enough that a count-rate class analysis could not be performed. The count-rate class analysis performed on the reference was not necessary due to the relatively low precision on the $^{80}Zr^{16}O^{+}$ measurements. Individual ratio measurements uncertainties were all near 1×10^{-6}, so all systematic errors were negligible. The final weighted ratio was $\bar{R} = 1.129\,829\,01(99)$ with a Birge ratio of 0.58(21) indicating that the measurement fluctuations were purely statistical and that the uncertainties may have been overestimated.

4.3 Mass Measurement Results

Table 4.1 lists the mass excesses, i.e. the difference between the mass of the atom and its mass number, of each measured isotope calculated from the average ratios $\bar{R}$ reported above along with their comparisons to the Atomic Mass Evaluation of 2020 (AME20) [1]. The mass measurement results are in good agreement with the mass values recommended by AME20 [1], and provide an improvement of one order of magnitude or more to the precision of the ^{80,81,83}Zr masses. The AME20 values for $^{81\text{-}83}$Zr are derived mainly from previous high precision mass measurements. Penning trap mass measurements of ^{82,83}Zr performed at JYFLTRAP form the basis of the AME20 mass values for these isotopes [94, 95], while a recent HIRFL-CSR storage ring measurement [96] dominates the AME20 mass of ^{81}Zr. Our measurement of ^{82}Zr has the largest discrepancy from AME20 with a value $1.5\,\sigma$ lower. The mass of ^{80}Zr listed in AME20 is an extrapolated value calculated from neighboring known nuclei using smooth trends of the mass surface. It is worth noting that two previous mass measurements of ^{80}Zr have not been included in the AME. A measurement with only a single event [42] yielded a mass excess of -55.5 (1.5) MeV. The second measurement [97], albeit significantly more precise with a mass excess of -55 647 (150) keV, has not been included in the AME because other isotopes measured in the same experiment were in disagreement with more recent high-precision results (e.g. ^{68}Se [98, 99] and ^{80}Y [94, 99]).

Isotope	Mass Excess	AME20 [1]	Difference
^{80}Zr	-55 128 (80)	-54 760 (300)[a]	-370 (310)
^{81}Zr	-57 556 (10)	-57 524 (92)	-32 (93)
^{82}Zr	-63 618.6 (2.5)	-63 614.1 (1.6)	-4.5 (3.0)
^{83}Zr	-65 916.33 (65)	-65 911.7 (6.4)	-4.7 (6.5)

[a] Extrapolated value based on trends of the mass surface.

Table 4.1: Mass measurement results. The mass excesses are relative to the mass number of the isotopes of interest. The results are compared to the mass excesses recommended by the AME20 [1]. All mass excesses are in keV. 1σ uncertainties are shown in parenthesis.

4.4 The Anomalous Mass of ^{80}Zr

The mass measurement of ^{80}Zr revealed that this nucleus is significantly more bound than expected from systematic trends. Indeed, high-quality extrapolations of the mass surface towards ^{80}Zr have been produced by the AME collaboration and others; this has been especially motivated by the astrophysical significance of this nucleus for X-ray bursts [100]. The mass value from this measurement is 370 (310) keV/c^2 more bound than the extrapolated value from AME20 [1], and 950 (260) keV/c^2 more bound than the Lanzhou extrapolated value [96].

To study the impact of this mass measurement, various binding-energy differences were employed adopting the measured mass values for $^{80\text{-}83}$Zr. All other masses used in the calculations were taken from AME20 unless stated otherwise. Along the $N = Z$ line, nuclei are known to be exceptionally well bound as neutrons and protons occupy the same shell model orbitals. Therefore, a useful indicator is the double mass difference δV_{pn} (eq. 1.6).

In Fig. 4.3a and Fig. 4.3b, δV_{pn} is shown for the $N = Z + 2$ and $N = Z$ sequences, respectively. For nuclei away from $N = Z$, the overall behavior of δV_{pn} is well described by the macroscopic mass formula [24, 101] (MMF): $\delta V_{pn} \approx 2(a_{\rm sym} + a_{\rm ssym} A^{-1/3})/A$, where $a_{\rm sym}$ and $a_{\rm ssym}$ are, respectively, symmetry and surface-symmetry energy coefficients. In the MMF plotted in Figure 4.3a, the values $a_{\rm sym} = 35\,$MeV and $a_{\rm ssym} = -59\,$MeV were employed and determined through a fit to the data neglecting the outliers at $A = 58, 82, 102$. Along the $N = Z$ sequence, δV_{pn} is strongly impacted by the Wigner energy [4], whose behavior is more convoluted. Moreover, mass data on the neutron-deficient side of $N = Z$ are scarce in the investigated region. Consequently, if some masses required for the δV_{pn} determination were not experimentally available, the recommended values from AME20 [1]

were used instead.

Although δV_{pn} is expected to vary smoothly overall, fluctuations around the average trend carry important structural information [23–25]. Binding-energy outliers, especially those found in magic nuclei along the $N = Z$ line, result in δV_{pn} deviations for both $N = Z$ and $N = Z + 2$ sequences. Considering the $N = Z + 2$ results with masses from this work, the value of δV_{pn} for ^{82}Zr (which is reliant on the mass of ^{80}Zr) is a clear outlier, being 185 keV lower than the MMF trend. This anomaly is similar to those found in ^{58}Ni and ^{102}Sn, associated with the increased binding energies of the doubly-magic self-conjugate nuclei ^{56}Ni and ^{100}Sn. The increased binding energy of ^{80}Zr also impacts the $N = Z$ trends resulting in increasing values of δV_{pn} for Zr and Mo.

Analogous outliers can also be found inspecting other mass filters at ^{80}Zr, such as the two-proton shell gap δ_{2p} [102]:

$$\begin{aligned} \delta_{2p}(N,Z) &= 2B(N,Z) - B(N,Z+2) - B(N,Z-2) \\ &= S_{2p}(N,Z) - S_{2p}(N,Z+2), \end{aligned} \tag{4.1}$$

which approximates the second derivative of the nuclear binding energy [102] making it a useful quantity for studies of magic numbers and their appearance or disappearance across a sequence of nuclei [13]. The δ_{2p} mass filter as a function of proton number for both the $N = Z$ and $N = Z + 2$ sequences is shown in Figure 4.4. Along the $N = Z$ sequence, ^{80}Zr is again a clear outlier with a similar increase from the baseline that is observed in ^{56}Ni.

The results shown in Fig. 4.3 and 4.4 provide compelling empirical evidence for the existence of a deformed shell closure in ^{80}Zr. One needs to bear in mind, however, that ^{80}Zr is a self-conjugate system and some additional contribution to its binding energy comes

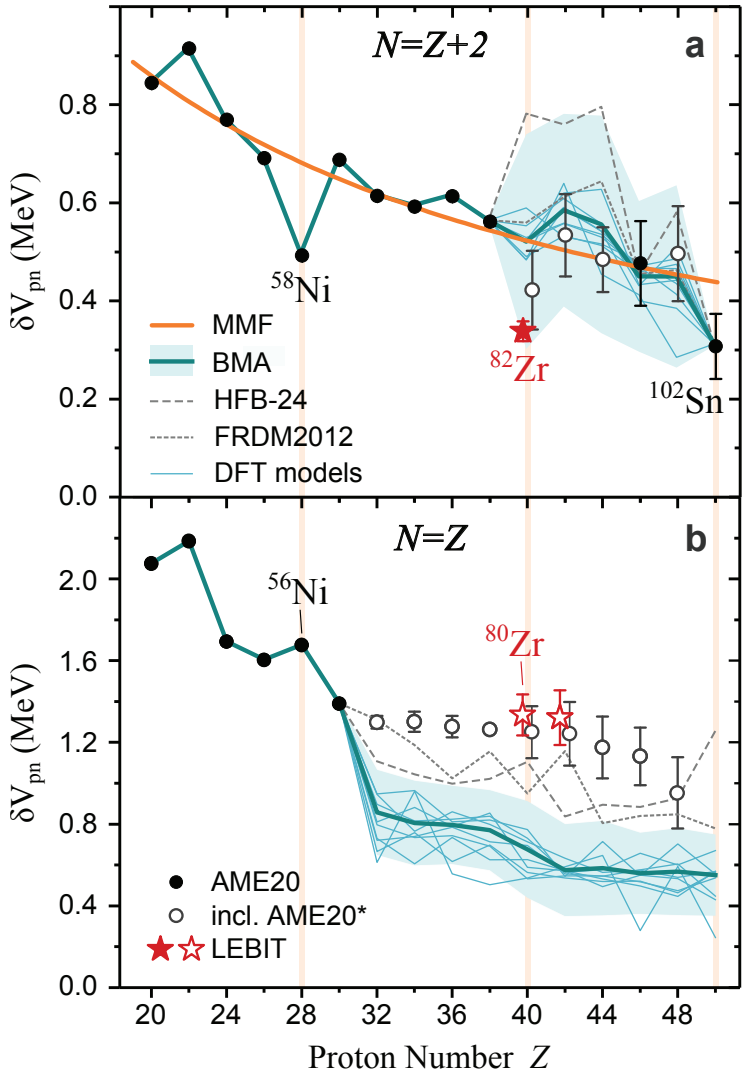

Figure 4.3: The effect of the anomalous mass of ^{80}Zr on the mass indicator δV_{pn}: a significant decrease from the baseline in the $N = Z + 2$ sequence **(a)**, and a slight rise in the $N = Z$ sequence **(b)**, which mirrors the behavior of other doubly-magic nuclei (e.g. ^{56}Ni and ^{100}Sn). Black circles represent mass data from the AME20 [1]. Red stars include data from this work. Closed symbols (both circles and stars) include only experimental mass values from AME20 [1]. Open symbols include mass extrapolations (AME20*) from AME20 [1]. All symbols include 1σ error bars. In many cases the error bars are too small to see. The MMF prediction is marked by an orange line in **(a)**. The thick teal line is the BMA result based on several nuclear models (thin solid lines: DFT models; thin dashed lines: HFB-24 and FRDM2012 models that include the Wigner-energy correction), and the light teal band represents the uncertainty of the BMA approach. The vertical bands denote the magic numbers 28 and 50 as well as the proton number of Zr, $Z = 40$.

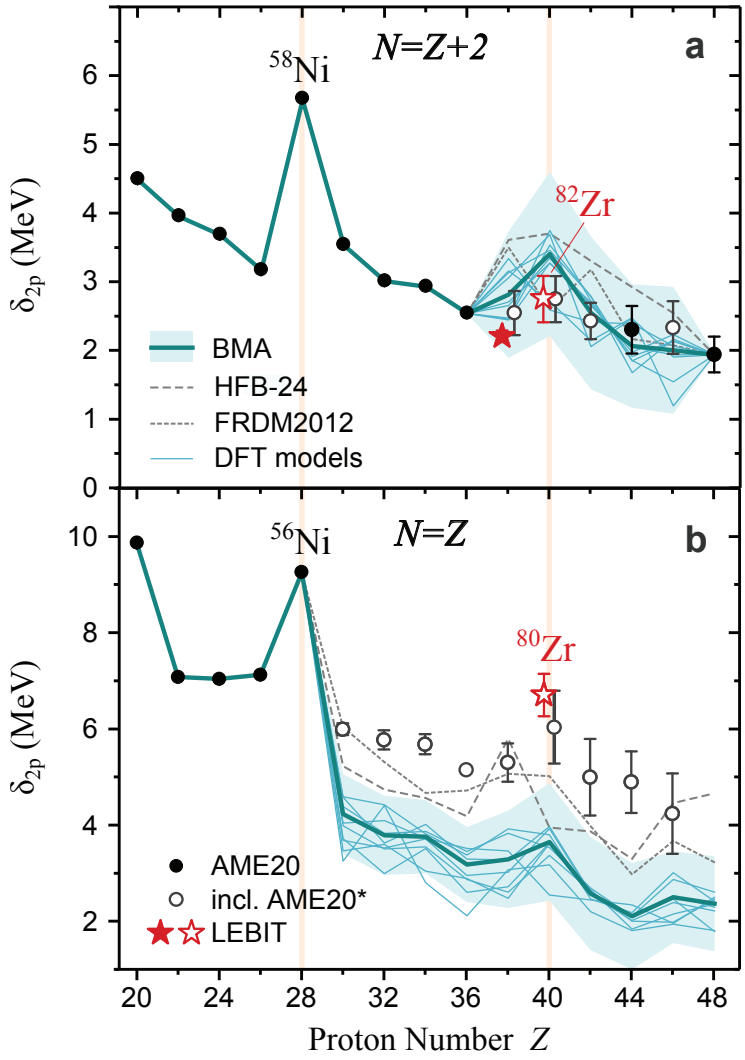

Figure 4.4: The effect of the anomalous mass of ^{80}Zr on the mass indicator δ_{2p}: a decrease from the baseline in the $N = Z + 2$ sequence **(a)**, and a corresponding rise in the $N = Z$ sequence **(b)**. Black circles represent mass data from the AME20 [1]. Red stars include data from this work. Closed symbols (both circles and stars) include only experimental mass values from AME20 [1]. Open symbols include mass extrapolations (AME20*) from AME20 [1]. All symbols include 1σ error bars. In many cases the error bars are too small to see. The thick teal line is the BMA result based on several nuclear models (thin solid lines: DFT models; thin dashed lines: HFB-24 and FRDM2012 models that include the Wigner-energy correction), and the light teal band represents the uncertainty of the BMA approach. The vertical bands denote the magic number 28 and the proton number of Zr, $Z = 40$.

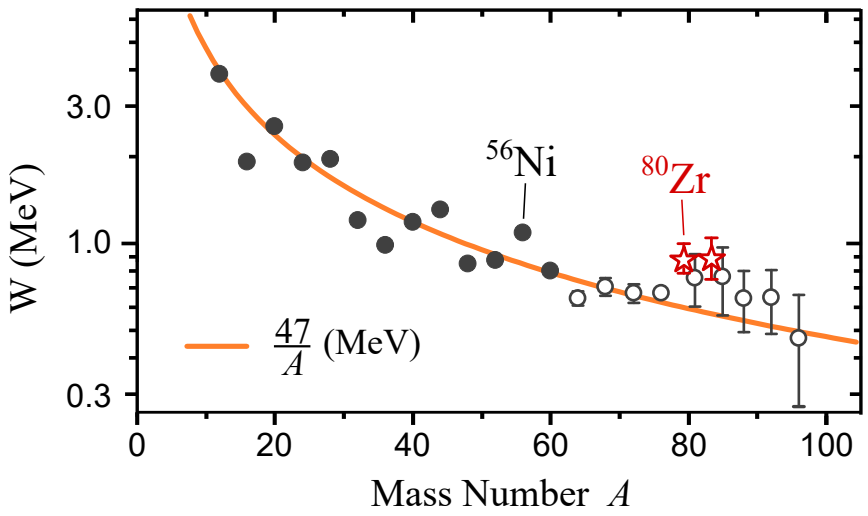

Figure 4.5: The Wigner-energy coefficient $W(A)$ extracted from δV_{pn} values according to eq. 1.9 [4]. Black circles represent mass data from the AME20 [1]. Red stars include data from this work. Open symbols (AME20*) include mass extrapolations. The average trend of [4] is shown by a thick line. All symbols include 1σ error bars. In many cases the error bars are too small to see.

from the Wigner energy. Usually, the Wigner term in even-even nuclei is parametrized as $E_W = -a_W|N-Z|/A$ (eq. 1.8). As discussed in [4] and Chapter 1, the Wigner-energy coefficient $W(A) = a_W/A$ can be empirically extracted from the values of δV_{pn} through eq. 1.9. Data from this experiment, shown in Figure 4.5, indicate that the value of $W(A)$ at ^{80}Zr and ^{56}Ni is locally enhanced, contrary to the gradually decreasing trend for heavier $N = Z$ nuclei that is well captured by the value of $a_W = 47\,\text{MeV}$ obtained in [4]. A note of caution is in order: some contribution to the local increase of the empirical value of W in ^{80}Zr and ^{56}Ni can be attributed to the enhanced binding due to their shell structure. The contributions of the Wigner energy and shell structure will be disentangled with another mass filter below.

Experimental masses offer a way to assess the size of the deformed $N = 40$ single particle gap. This can be done by employing an estimate of the single-particle energy gap at the

Fermi level:

$$\begin{aligned}\Delta e(N,Z) = e_{n+1} - e_n =& 2[\Delta_n^{(3)}(N=2n,Z) - \Delta_n^{(3)}(N=2n+1,Z)] \\ =& (-1)^N[S_n(N,Z) - S_n(N+2,Z)],\end{aligned} \tag{4.2}$$

where $\Delta_n^{(3)}(N,Z)$ is the three-point mass difference [10]:

$$\begin{aligned}\Delta_n^{(3)}(N,Z) =& \frac{(-1)^N}{2}[2B(N,Z) - B(N-1,Z) - B(N+1,Z)] \\ =& \frac{(-1)^N}{2}[S_n(N,Z) - S_n(N+1,Z)].\end{aligned} \tag{4.3}$$

Figure 4.6 shows Δe for the Zr isotopic chain (see [103] for the applications of Δe to the K and Ca chains). Some masses of proton-rich Zr isotopes needed to determine Δe are not known experimentally; those have been taken from mass relations of mirror nuclei by Zong et al. [11] because they are better constrained than the extrapolations from AME20. Furthermore, it is difficult to trust the AME extrapolations near ^{80}Zr due to the discrepancy between the measured value and the extrapolation for ^{80}Zr. It is seen that Δe reaches a maximum for ^{90}Zr at the spherical magic number $N = 50$ and a local maximum for ^{80}Zr at the deformed magic number $N = 40$. Since the latter value can be affected by the Wigner energy, the binding-energy contribution from E_W was removed by applying two models: $E_W(1)$ (eq. 1.7) [3] and $E_W(2)$ (eq. 1.8) [4]. The resulting correction to Δe practically affects the $N = 40$ value only. The expression $E_W(1)$ is well localized at $N = Z$ and reduces Δe by about 300 keV. The expression $E_W(2)$ decreases linearly with the neutron excess, and the corresponding reduction of Δe is about 1.1 MeV. Even in this case, the energy gap at $N = 40$ is a factor of 2-3 larger than Δe for $42 \leq N \leq 48$. While the size of this gap is reduced as compared to the spherical $N = 50$ gap, it is characteristic of a deformed shell

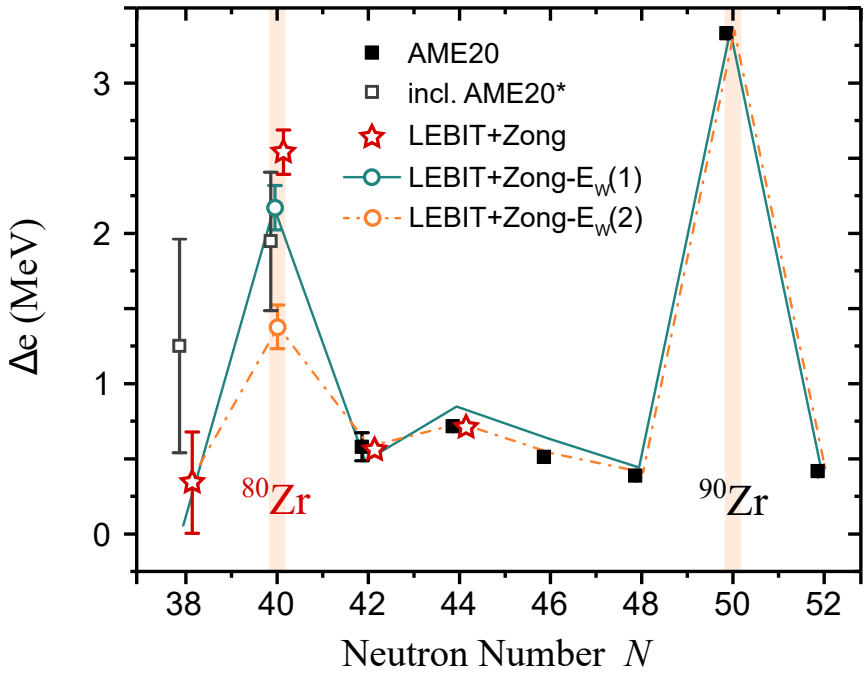

Figure 4.6: The empirical single-particle energy gap $\Delta e(N)$ at the Fermi level for the chain of even-even Zr isotopes extracted from nuclear binding energies according to [10]. Black squares represent mass data from the AME20 [1]. Open gray squares include AME20 mass extrapolations (AME20*). Open stars represent the data from this work augmented by mass extrapolations from [11]. These values of Δe were further corrected by removing contributions from the Wigner energy term $E_W(1)$ (solid line [3]) or $E_W(2)$ (dash-dotted line [4]). No uncertainty is assigned to $E_W(1)$ or $E_W(2)$, so the error bars for the corrected Δe values match those of the corresponding uncorrected values. The corrected Δe error bars are only shown for ^{80}Zr. All error bars represent a 1σ uncertainty. In many cases the error bars are too small to see. The vertical bands denote shell closures at $N = 40$ and $N = 50$.

closure. The strong shell effect comes from the self-conjugate nature of ^{80}Zr as the deformed proton and neutron shell effects reinforce one another.

4.5 Bayesian Analysis of Mass Models

To obtain improved theoretical mass predictions in the ^{80}Zr region, A Bayesian statistical analysis combining Gaussian process extrapolation and BMA [104] of eleven theoretical global mass models following the same procedure as in [38, 105] was conducted by nuclear

theory and statistics collaborators R. Jain, S. A. Giuliani, W. Nazarewicz, and L. Neufcourt. The BMA framework uses the collective wisdom of the models, constrained by data, to make predictions and quantify uncertainties. In this study 9 nuclear density functional theory (DFT) models were considered [106–114]. Two additional mass models commonly used in nuclear astrophysics studies were also considered: FRDM2012 [115] and HFB-24 [3]. Details on the individual models and the BMA methodology can be found in the included references.

The BMA predictions for δV_{pn} are shown in Fig. 4.3. The predictions for $N = Z + 2$ are well constrained outside the region $38 < Z < 50$ due to the wealth of experimental mass data. In the region $38 \leq Z \leq 50$, the BMA results are consistent with the AME20 data and the MMF trend. At $Z = 40$, the experimental δV_{pn} value, which includes the mass results of ^{80,82}Zr from this experiment, falls just within the error band. The BMA result for δV_{pn} along the $N = Z$ line in the region $Z > 30$ does not agree with either the AME20 extrapolations or the LEBIT values. Two of the models, FRDM2012 [115] and HFB-24 [3], that include the phenomenological Wigner term perform slightly better than the density functional theory (DFT) models. However, they still fall short of the experimental trends, most likely due to an underestimated Wigner energy. Indeed, the value of a_W in FRDM2012 [115] is 30 MeV, which is significantly less than $a_W = 47$ MeV representing the average trend seen in Fig. 4.5. The Wigner energy $E_W(1)$ of HFB-24 is even smaller.

The BMA predictions for δ_{2p} are shown in Fig. 4.4 and similar trends seen in the δV_{pn} results are observed. For the $N = Z+2$ sequence, the BMA prediction agrees with experiment within the estimated uncertainty. For $N = Z$, the anomalous mass of ^{80}Zr results in an increase of δ_{2p} above the baseline. Similar to what is seen in Fig. 4.3b, the HFB-24 and FRDM2012 models that include the Wigner-energy correction lie slightly below the data

points again suggesting that the Wigner energy term is underestimated by both models.

4.6 Conclusion and Perspective for $^{80-83}$Zr Mass Measurement

The high precision mass measurements of $^{80\text{-}83}$Zr performed at the LEBIT facility allow a more detailed investigation of the mass surface in the region of strongly deformed nuclei with $N \approx Z \approx 40$. The measurement reveals a significant enhancement in the binding energy of ^{80}Zr. By considering binding-energy indicators, this enhancement can be attributed to a deformed double shell closure and an increase in the Wigner energy of this exotic self-conjugate system. A Bayesian average based on eleven global mass models was unable to account for the new mass value of ^{80}Zr as the Wigner-energy enhancement has not been taken into account microscopically. The comparisons to theory demonstrate the challenges posed by this region of the nuclear chart where deformation effects, isospin breaking effects, and proton-neutron pairing can coexist. The interplay between theory and experiment was crucial in understanding this region of the nuclear chart. While the deformed shell gap at $N = Z = 40$ was predicted over 30 years ago [2, 28], a lack of precise experimental data prevented a quantitative assessment of the gap's size until now.

In order to test the robustness of the deformed shell closures near $N \approx Z \approx 40$, the mass surface must be defined towards and beyond the isotopes of interest, so that variations in the binding energy evolution are properly captured and the dependence on extrapolation is removed. Since nuclear structure phenomena manifest in the scale of hundreds of keV to few MeV, masses should be measured to an uncertainty of $\delta m < 100$ kev/c^2 for detailed structural investigations. In the case of ^{80}Zr, it would be desirable to improve the precision on the mass

value of ^{80}Zr and determine the binding energies of ^{78,79}Zr (towards lower neutron number) as well as ^{81}Nb and ^{82}Mo (towards higher proton number). To evaluate pairing gaps in the nearby neighbors ^{78,79}Y, the masses of $^{77-80}$Y, ^{77,78}Sr, and ^{79,80}Zr are required. Among these, the masses of ^{77,78}Sr and ^{80}Y have already been measured to < 10 keV/c^2 via Penning trap mass spectrometry [94,116,117]. An FRIB proposal has been accepted to perform mass measurements of $^{78-80}$Zr and $^{77-79}$Y, which will remove many of the experimental gaps in this region of the nuclear chart. Measurements of ^{81}Nb and ^{82}Mo are not currently within reach due to their very short lifetimes and/or low production rates.

Chapter 5

The Development of the Single Ion Penning Trap Mass Spectrometer for Rare Isotopes

While FRIB will allow access to many additional rare isotopes, some of these isotopes, like ^{100}Sn – the heaviest $N = Z$ nucleus, will still be produced at low rates (expected rate ≤ 1 particle per minute at LEBIT) during the first year of operation. These low rates are at odds with the current destructive mass measurement techniques used at LEBIT and other rare isotope PTMS facilities around the world. Hence, more sensitive mass measurement techniques are needed. This chapter presents the development of LEBIT's single ion Penning trap (SIPT) that makes use of the nondestructive FT-ICR technique described in Chapter 2. Some of the work presented in this chapter was published in [8] and discussed in [12]. Since the release of [8, 12], simulations, physical upgrades, and experimental studies have been performed to guide SIPT towards it's ultimate goal: precision mass measurements with a single ion.

5.1 SIPT Design

5.1.1 The Beamline

The SIPT beamline was designed to be an extension of the LEBIT main trap beamline. Fig. 5.1 provides a schematic of the SIPT beamline, which connects to the main beamline just after beam observation box 4 (BOB4). A 25° spherical kicker is used to divert ions from the cooler and buncher off the main beamline and into the SIPT beamline. Ions then move through a series of two electrostatic quadrupoles, a 115° cylindrical bender, which is split by another electrostatic quadrupole, and two final electrostatic quadrupoles. These five quadrupoles along with the bender complete the steering and focusing through the beamline bend. After the bend, ions are focused with two Einzel lenses before entering the SIPT magnet. Just before the magnet, at SIPT BOB3, an MCP in the Daly configuration [87] is setup to allow for TOF-ICR. The MCP and Daly collector are also used to extend the electric potential between the SIPT beamline and the drift tubes within the magnet. Faraday cups and phosher screens are present at both SIPT BOB1 and BOB2 to help diagnose and improve beamline transmission.

Upon entering the magnet, ions pass through a series of six drift tubes that transport them through the magnet and reduce their energy for optimal capture in the Penning trap. After the six drift tubes, a set of Lorentz steerers are used to steer the ions either off-center for ν_c measurements or on-center for ν_+ measurements. A final drift tube is between the Lorentz steerers and the Penning trap.

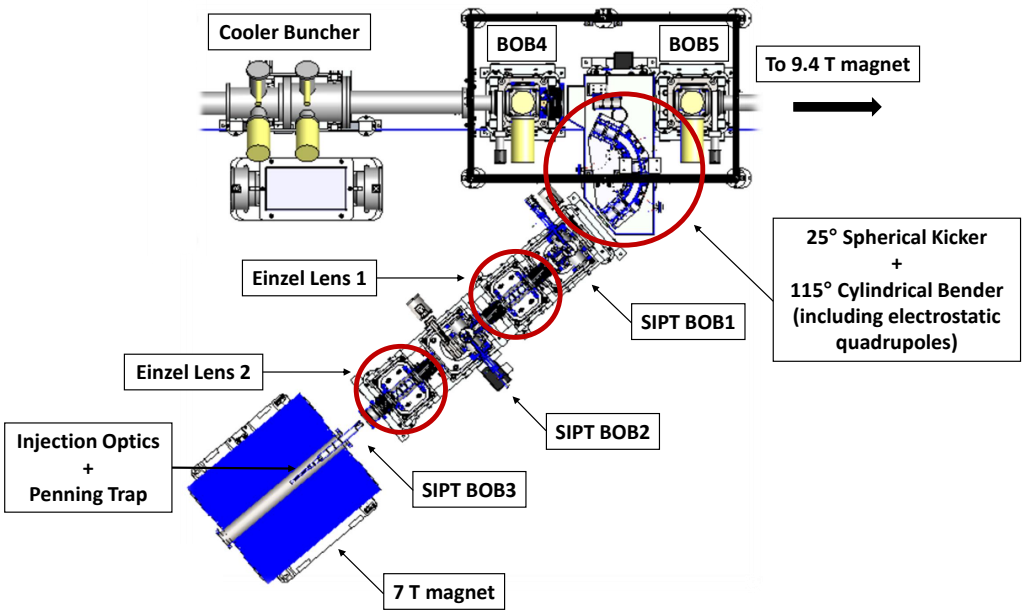

Figure 5.1: Schematic of the SIPT Beamline. Figure adapted from [12].

5.1.2 The Penning Trap

5.1.2.1 The Magnet

The SIPT magnet is a 7 T superconducting solenoid from Oxford Instruments. It has excellent field stability over time with a field decay of ≤ 50 ppb/hr. Active shielding is also employed to reduce the fringe field outside the magnet. Possible frequency shifts associated with the magnetic field are due to field decay over time, trap vibrations caused by the cryocooler expansion cycle, and misalignments between the trap and the magnetic field. The field decay can be accounted for by taking occasional measurements of reference ions with a well-known mass. The cryocooler expansion cycle has a period of ~ 1 s, which could cause a slow trap vibration within the magnet. The shift in the cyclotron frequency due to

this vibration can be estimated by

$$\frac{\Delta\nu_c}{\nu_c} = \frac{dB_{rel}}{dZ}\Delta Z \tag{5.1}$$

where $\Delta\nu_c/\nu_c$ is the relative cyclotron frequency shift, dB_{rel}/dZ is the gradient of the relative magnetic field strength, and ΔZ is the peak-to-peak amplitude of the trap vibrations. Using a worst-case relative field gradient of 4×10^{-7}/mm based on Oxford magnet specifications and 20 μm for the peak-to-peak amplitude of the vibrations (typical maximum expected for a pulse tube cryocooler) leads to a relative frequency shift of less than 8 ppb.

Shifts in the cyclotron frequency due to a misalignment between the trap and the magnetic field scale approximately with the square of the misalignment angle θ [69]:

$$\Delta\nu_c \approx \nu_-\left(\frac{9}{4}\theta^2 - \frac{1}{2}\epsilon^2\right) \tag{5.2}$$

where ϵ is the eccentricity of the trapping potential. The angular alignment between the magnetic field and the bore tube was determined using an NMR probe to measure the field at a series of points along the axial planes ± 4 cm from the center of the magnet at a radius of 2.5 cm. From this data and assuming the trap is perfectly aligned with the bore tube, a misalignment of $\theta \approx 0.002^\circ$ was found resulting in mass shifts well below 1 ppb. Additional frequency shifts can still be introduced from a misalignment between the trap axis and the bore tube. However, these shifts must be evaluated experimentally. If they happen to be significant, they can likely be compensated by introducing eccentricity to the trapping potential.

5.1.2.2 The Penning Trap Electrode System

A schematic of the SIPT Penning trap electrode system along with its dimensions can be seen in Fig. 5.2 and Table 5.1, respectively. The size and geometry of the electrode system is of particular importance for SIPT. SIPT uses a hyperbolic trap geometry, which provides the best approximation of a perfect quadrupole potential with finite electrodes [65, 67]. The design of the electrodes is based on the Penning trap used in the 9.4 T magnet but scaled down to 50% of the size. The smaller size of the trap minimizes the radius of the ions' motion which in turn minimizes frequency shifts due to special relativity. Relative cyclotron frequency shifts due to special relativity scale with the square of the radius of the modified cyclotron motion [67] and are expected to be less than 6 ppb for masses greater than 70 amu. Furthermore, these frequency shifts will mostly cancel if the reference ion and ion of interest are a mass doublet. Field imperfections due to the finite size of the end cap and ring electrodes as well as the hole in the end cap are largely compensated by correction ring and tube electrodes. A method for minimizing frequency shifts due to field imperfections is presented later in this chapter.

a (Height Endcap-to-Endcap)	28 mm
b (Radial Width)	28 mm
L_{CR}	3.9 mm
ρ_0	6.485 mm
z_0	5.59 mm
r_a	2 mm
α	54.74°

Table 5.1: SIPT Penning trap dimensions. The labels in the left column are depicted in Fig. 5.2.

The trap electrodes are made of oxygen-free copper with good thermal conductivity at cryogenic temperatures and plated with gold to reduce potential electric field irregularities due to patch effects. Sapphire insulators are used to maintain thermal conductivity across

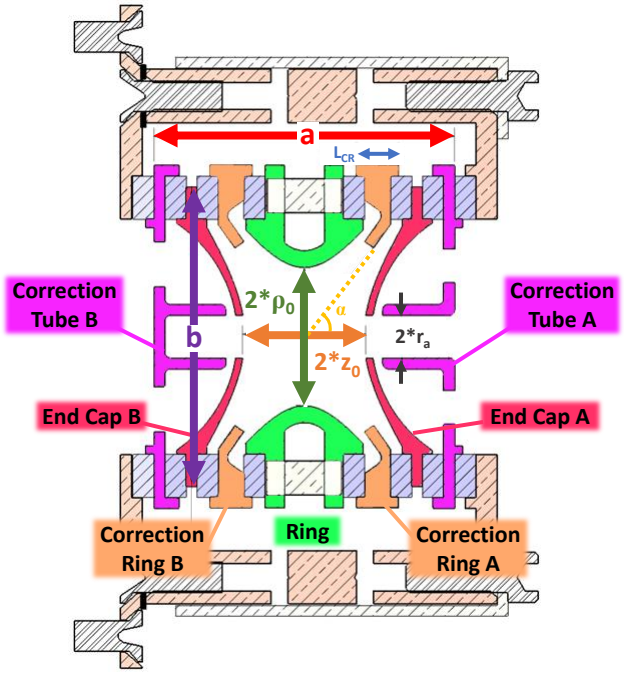

Figure 5.2: Design drawing of the SIPT hyperbolic Penning trap electrode structure. The trap dimensions are listed in Table 5.1. Figure taken from [8, 12].

the trap. The ring electrode is segmented into eight identical pieces to allow for flexibility in the detection and excitation configuration making it possible to create configurations for detecting either the modified cyclotron frequency or the cyclotron frequency. Pictures of the trap before, during, and after assembly are presented in Fig. 5.3. All trap voltages except those for the correction tubes first pass through a cryogenic filter board to prevent noise from the power supplies being detected in the FT-ICR signal. The correction tube wires were decoupled from the filter board to allow current pickup off the tubes for beamline tuning.

5.1.3 The Cryogenic Image Charge Detection System

As mentioned in Chapter 2, the SIPT detection circuit must be operated at cyrogenic temperatures to achieve single ion sensitivity. A schematic of the detection circuit is presented

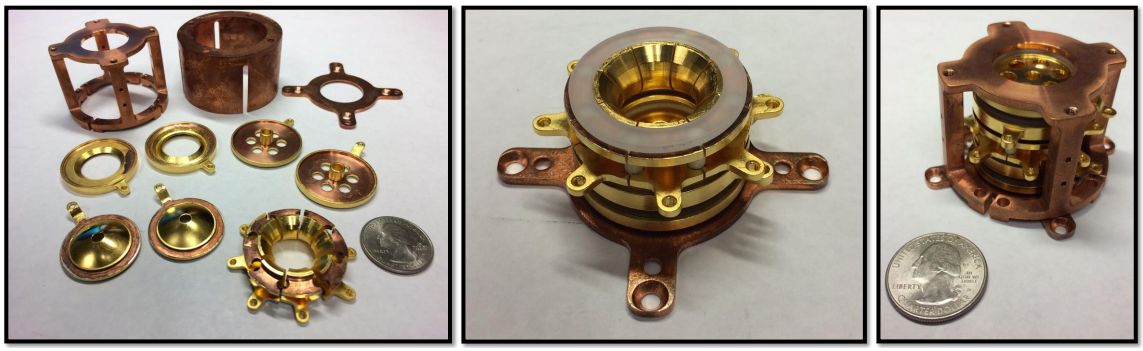

Figure 5.3: SIPT Penning trap before assembly (left), during assembly (middle), and after assembly (right). A quarter is shown for scale. Figure adapted from [8, 12].

in Fig. 5.4, and an image of the NbTi inductor coil and it's casing is shown in Fig. 5.5. The cryogenic amplifier utilizes gallium arsenide (GaAs) FET technology to provide low noise amplification at cryogenic temperatures. To minimize noise pickup on the wires, the amplifier is kept as close as possible to the Penning trap. The output from the cryogenic amplifier is delivered by cryogenic coaxial cable to a room temperature A7-2 amplification module. The A7-2 also provides stable, low-noise DC supply voltages to the cryogenic amplifier via an internal PID loop. After passing through the room temperature amplifier, the signal is sent through a low-noise frequency mixer, which subtracts a given local oscillator frequency from the entire signal. This frequency mixing shifts the ion signal to a much lower frequency, allowing for high-resolution signal sampling with less data.

For the first tests of FT-ICR, the trap has been wired for dipole pickup of the modified cyclotron frequency ν_+. Three adjacent ring segments were connected together to provide ample surface area for image current pickup. The three adjacent segments opposite the pickup segments are grounded for signal reference. The remaining two ring segments are used for the rf signals to drive the ions' motion. In principle, a stronger ν_+ signal could be obtained by using the grounded segments for differential signal pickup. However, the current cryogenic amplifier is known to perform much better with single-input pickup.

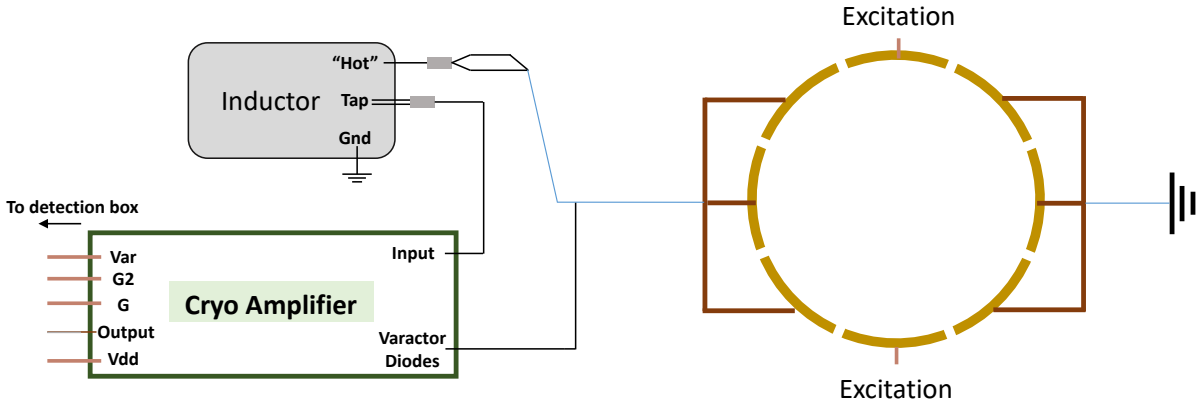

Figure 5.4: Schematic of the SIPT detection circuit. The inductor and cryogenic amplifier wiring are shown on the left, while the trap ring electodes are shown on the right. Figure adapted from [8, 12].

Figure 5.5: The 600 μH NbTi inductor coil (left) and NbTi inductor case (right) used for the SIPT FT-ICR detection circuit. Figure adapted from [8, 12].

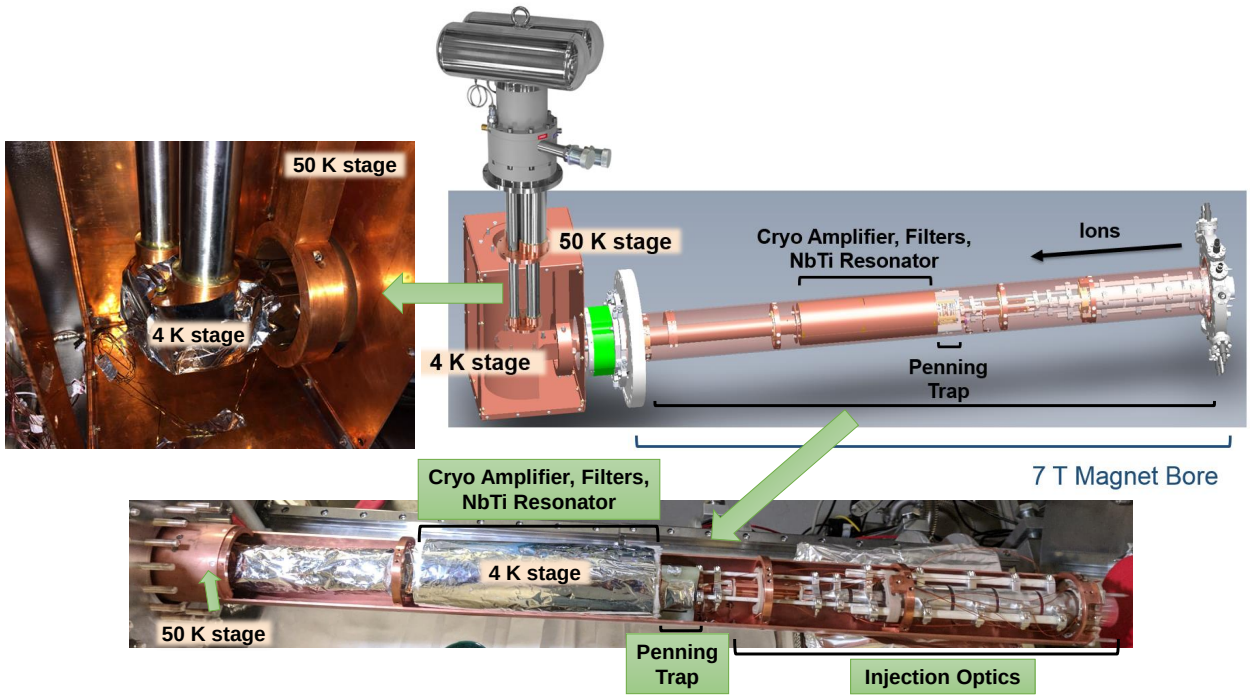

Figure 5.6: Overview of the SIPT cryogenic system components (top right) as well as images of the inside of the detection box where the cold head is located (top left). The injection optics, Penning trap, and 4 K chamber that houses the cryogenic filters and detection electronics are also shown (bottom). Several of these components are wrapped in Mylar insulation. Figure adapted from [8].

The cryogenic temperatures necessary for single ion sensitivity are achieved using the PT415 cryorefrigerator with the CP1110 helium compressor from Cryomech, Inc. This pulse tube cryocooler has no moving parts in the low-temperature section resulting in very low vibrations. The model is operated with a remote motor located off the high voltage platform allowing the compressor package to remain at ground. The compressor is connected to the back of the cold head by transfer lines with a high-voltage insulating break.

An overview of the SIPT cryogenic system is presented in Fig. 5.6. The SIPT cryocooler includes two temperature stages. The first stage reaches temperatures around 50 K and is thermally coupled to a copper shield which surrounds the lower temperature stage. The 50 K copper shield consists of a long hollow tube, which extends through the magnet bore

Figure 5.7: SIPT 4 K stage wrapped in Mylar insulation to reduce radiative heating from the surrounding 50 K stage. Figure adapted from [8, 12].

and acts as both a heat shield and housing for all of the components of SIPT that sit inside the magnet. The second stage reaches temperatures around 4 K and is thermally coupled to the SIPT cryogenic components including the superconducting resonator circuit, cryogenic amplifier, cryogenic filters, and Penning trap electrodes. The cold head sits inside the SIPT detection box, which is mounted to the end of the SIPT magnet. It is connected to the cryogenic components via a long copper arm which extends into the bore of the magnet. The 4 K stage copper arm connection as well as the chamber housing the detection electronics and cyrogenic filters are shown in Fig. 5.7. A copper shield inside the SIPT detection box connects to the 50 K stage and surrounds the cold head helping to isolate the 4 K stage. As can be seen in Fig. 5.6 and Fig. 5.7, several 4 K stage components are wrapped in aluminum coated Mylar insulation to reduce radiative heating from the 50 K stage. Apiezon N cryogenic high-vacuum grease is also applied between joints to increase thermal conductivity.

5.2 Simulations

5.2.1 Detection Scheme Simulations

The FT-ICR signal strength is highly dependent on the specific electrode configuration used to detect the ion's motion in the trap. As expressed in eq. 2.19, the signal strength is proportional to both the ion's velocity and the electric field produced by the detection electrodes. The velocity of the ions in an ideal Penning trap can be determined analytically from the equation of motion. In Cartesian coordinates where the axis parallel to the magnetic field is defined as the z-direction, the ion's position is given by

$$\begin{aligned} x &= \rho_+ \cos(\omega_+ t) + \rho_- \cos(\omega_- t) \\ y &= \rho_+ \sin(\omega_+ t) + \rho_- \sin(\omega_- t) \\ z &= \rho_z \cos(\omega_z t) \end{aligned} \tag{5.3}$$

where ρ_+, ρ_-, and ρ_z are the initial radii of the eigenfrequencies ω_+, ω_-, and ω_z respectively. Differentiating these expression with respect to time, t, gives the velocities:

$$\begin{aligned} v_x &= -\rho_+\omega_+ \sin(\omega_+ t) - \rho_-\omega_- \sin(\omega_- t) \\ v_y &= \rho_+\omega_+ \cos(\omega_+ t) + \rho_-\omega_- \cos(\omega_- t) \\ v_z &= -\rho_z\omega_z \sin(\omega_z t). \end{aligned} \tag{5.4}$$

The electric field must be solved numerically, which was done using SIMION [118]. Because image currents in SIPT are detected solely off the ring electrodes, the field only needed to be solved for the 8 ring electrodes. The dimensions of the simulated electrodes matched those of the SIPT trap, and a 0.25 mm/grid unit scaling was used. The field was refined to

a relative level of 5×10^{-7}. The refined electric field calculated by SIMION can be scaled by the voltages applied to each of the 8 ring electrodes. For the signal strength calculations, only $\pm 1, 0$ V were needed. The detection configurations were labeled in terms of the applied voltages to each electrode with a label of P for $+1$ V, M for -1 V, and 0 for 0 V. Ring electrodes used for rf-excitations were given a voltage of 0 V. The current configuration has a label of PPP00000, for example (see Fig. 5.10 for an illustration of two detection schemes). The signal strength could then be calculated as $S(t) = \vec{v} \cdot \vec{E}$.

The simulations were run over a period of $T = 1$ ms with a time step of $dt = 100$ ns. All combinations of integer steps of $\rho_{\pm}$ from 0 to 6 mm such that $\rho_+ + \rho_- \leq 6$ mm and ρ_z from 0 to 5 mm were simulated for each detection configuration. The signal strengths for ν_c and ν_+ were determined using the lock-in method:

$$S(\nu) = \left[\left(\frac{\int_0^T S(t) \cdot \cos(2\pi\nu t) dt}{T} \right)^2 + \left(\frac{\int_0^T S(t) \cdot \sin(2\pi\nu t) dt}{T} \right)^2 \right]^{1/2}. \tag{5.5}$$

Fig. 5.8 shows the signal strengths for ν_+ and ν_c as a function of ρ_+ and ρ_- for the current detection configuration PPP00000. From Fig. 5.8 (Left), it is clear that the ν_+ signal strength increases with increasing ρ_+. Hence, stronger ν_+ signals are achieved by driving the ion's ρ_+ as close as possible to the ring electrodes. To obtain stronger ν_c signals, both ρ_+ and ρ_- must be driven to the same distance and as close as possible to the ring electrodes (see Fig. 5.8 (Right)). Note that the maximum ν_+ signal strength is 3.6 times larger than the maximum ν_c signal strength.

Fig. 5.9 shows the ν_+ and ν_c signal strengths for three configurations. The ν_+ signal strengths are relative to the PPPP0000 configuration, which is the best possible approxima-

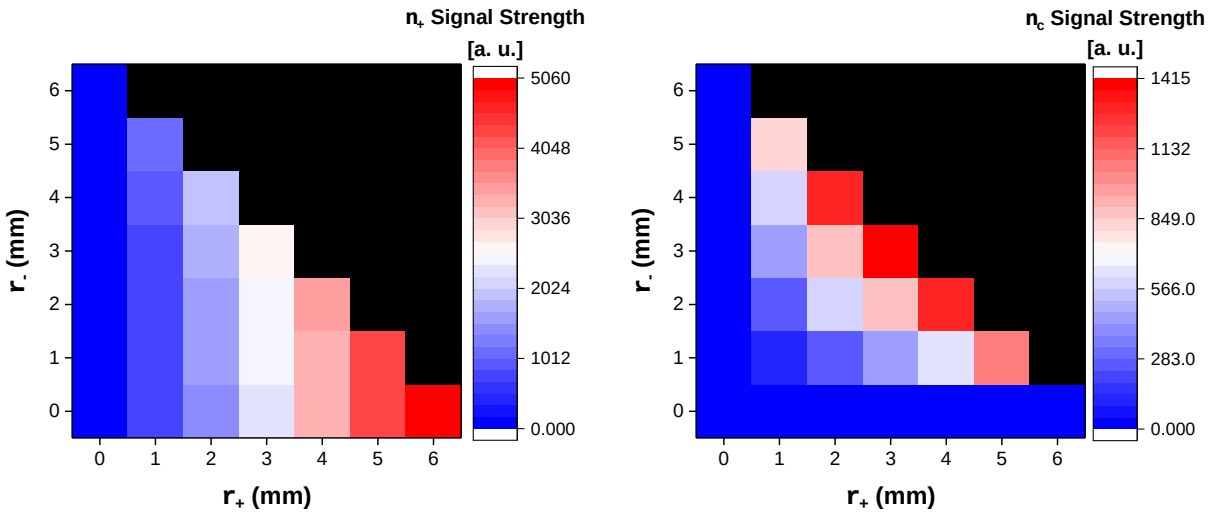

Figure 5.8: Heat maps of the PPP00000 configuration's signal strengths versus ρ_+ and ρ_- for ν_+ (Left) and ν_c (Right). The signal strength is denoted using a blue to red color scale. Black squares denote combinations of ρ_+ and ρ_- that are unphysical as they exceed the radius of the trap.

tion of a dipole configuration with the single-input amplifier. The ν_c signal strengths are relative to the PP00PP00 configuration. In both cases, if the true dipole and quadrupole configurations were possible, the signal strengths would be double their respective best approximations for a single-input amplifier. The current configuration performs well for picking up ν_+ but poorly for ν_c. However, adding one additional electrode directly opposite the three electrodes currently used doubles the ν_c signal strength. The loss in the ν_+ signal strength with this PPP00P00 configuration is minimal. The ratio of the maximum signal strengths for ν_+ to ν_c for the PPP00P00 configuration is 1.7. Hence, with this configuration, maximal ν_+ signal strengths should be almost double the size of the maximal ν_c signal strengths. Rewiring the SIPT detection circuit with the PPP00P00 (Fig. 5.10 (Right)) configuration would allow simultaneous measurements of ν_+ and ν_c making ion identification and verification more robust.

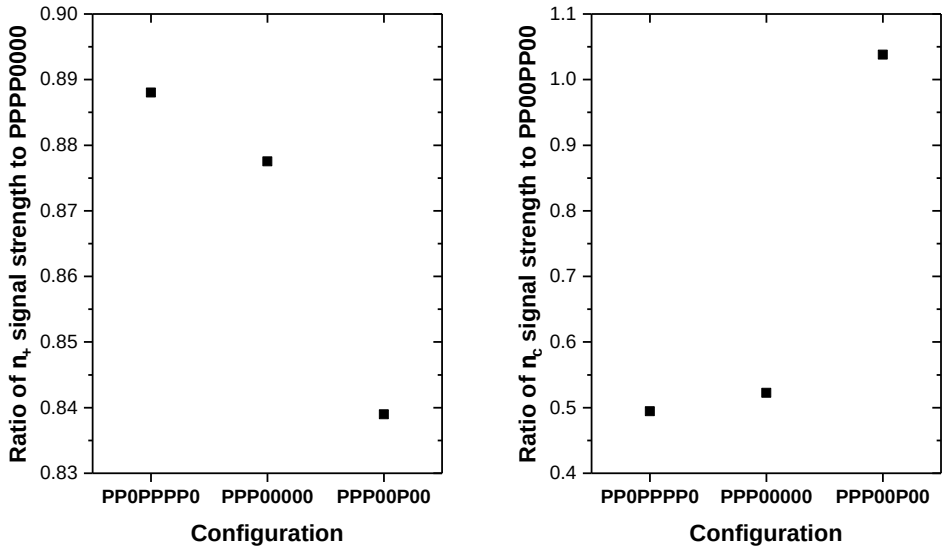

Figure 5.9: Comparison of several detection configurations for pickup of ν_+ and ν_c.

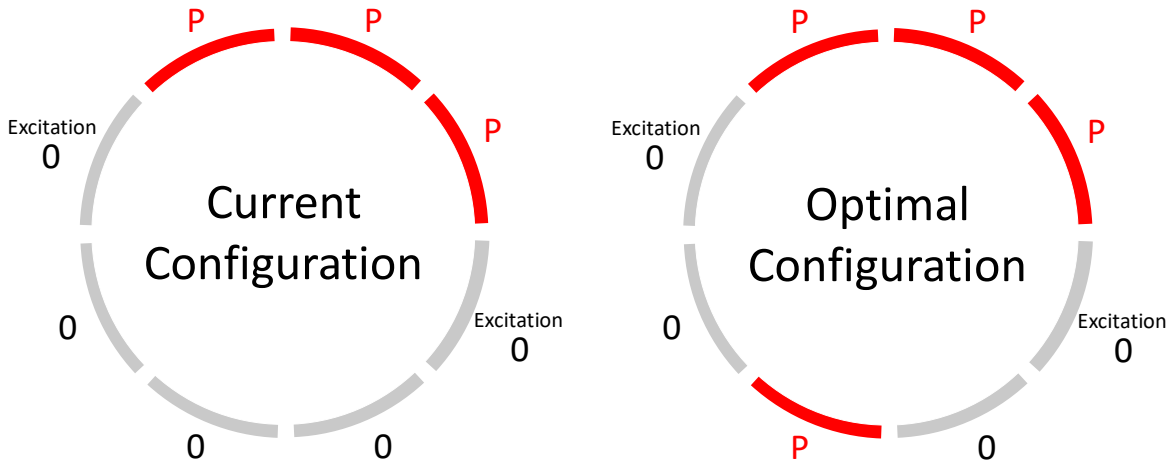

Figure 5.10: Schematic of the ring electrode detection configuration for the current configuration (Left) and optimal configuration for detecting both ν_+ and ν_c (Right).

5.2.2 Improved SIPT Beamline Simulations

In the past, simulations of the SIPT beamline were performed using SIMION [118] to determine the optimal voltages needed to maximize ion transport to the Penning trap while simultaneously minimizing the ions' radial energy inside the trap. The voltages applied to the bending elements and electrostatic quadrupoles were verified experimentally, however the voltages of the Einzel lenses led to poor transmission efficiency to the Penning trap. To explore this issue, simulations were performed again to find more optimal voltages for the Einzel lenses as well as the first few drift tubes. Table 5.2 compares the original simulation to the updated simulation for the Einzel lenses (EL) and first three drift tubes (DT). The visual result of sending 1000 ions one at a time down the beamline is shown in Fig. 5.11. The ions' initial conditions were taken from simulations of ions exiting the cooler and buncher. With the voltages shown in Table 5.2, over 99% of the ions were transported to the back of the Penning trap. However, it is worth pointing out that many of the ions still have initial cyclotron motion when entering the trap. This can lead to the smearing of FT-ICR signals, which is discussed later in the chapter.

Two methods were used to determine the optimal values experimentally. First, a continuous Kr^+ beam from the offline Colutron ion source was measured at several Faraday cups along the beam line. The Faraday cup readings were compared to measurements of the current detected on the Penning trap correction tube farthest from the entrance of the trap (CTB). A hand tuning was performed in this manner. After hand tuning with DC beam, the signal strength of FT-ICR signals was used to tune beamline elements. An optimizer program was created to scan various elements and choose an optimal value. These methods resulted in the experimental values seen in Table 5.2.

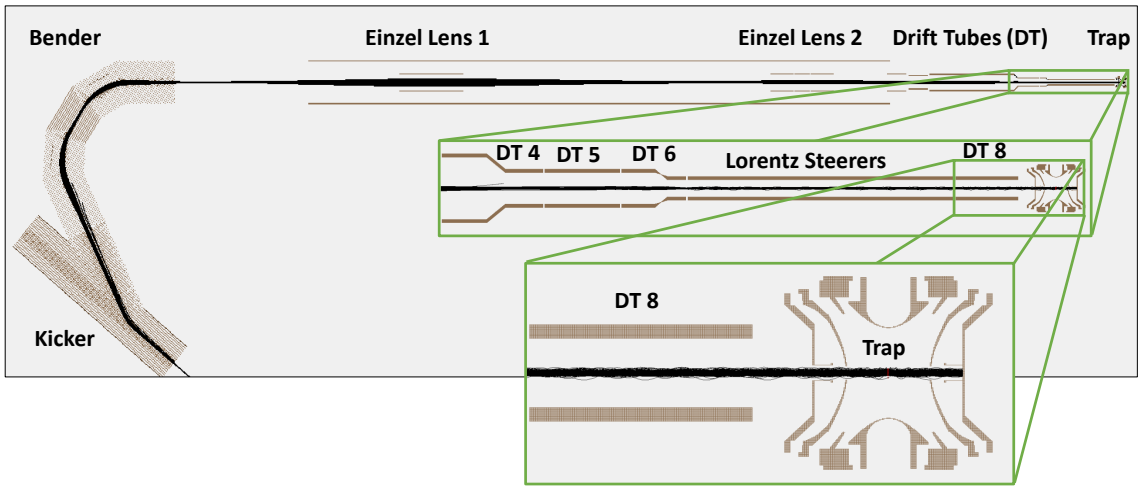

Figure 5.11: Image of the SIPT Beamline SIMION simulation. The black lines represent individual ion paths. Just over 99% of ions from the cooler and buncher reach the back of the Penning trap.

Beamline element	Original Voltage	Updated Voltage	Experimental Voltage	Difference
EL1	-4675	-1725	-1725	0
EL2	-3820	-2900	-2750	-150
DT1	NA	-1900	-1950	50
DT2	NA	-550	-555	5
DT3	NA	-1775	-1775	0

Table 5.2: Ion optics simulations. All voltages and differences are in V. The original voltages are from the first simulation. The updated voltages are from the new simulation. The experimental values are the current best voltages for maximizing ion transport efficiency. Not all elements were simulated in the original simulation. A not applicable (NA) has been placed in those spots.

To verify the performance of this beamline tuning method, a scan of the beam's axial energy profile was performed. Measurements of the beam current were taken at BOB4 (just after the cooler and buncher) and on CTB. The voltages of all trap electrodes except the ring electrodes and CTB were scanned, and the fraction of current remaining at the back of the trap was recorded. CTB was kept at -33 V. The ring electrodes could not be biased because they are involved in the detection circuit, so they were kept at ground. Varying the trap electrode voltages produces a potential barrier that only allows ions with enough energy

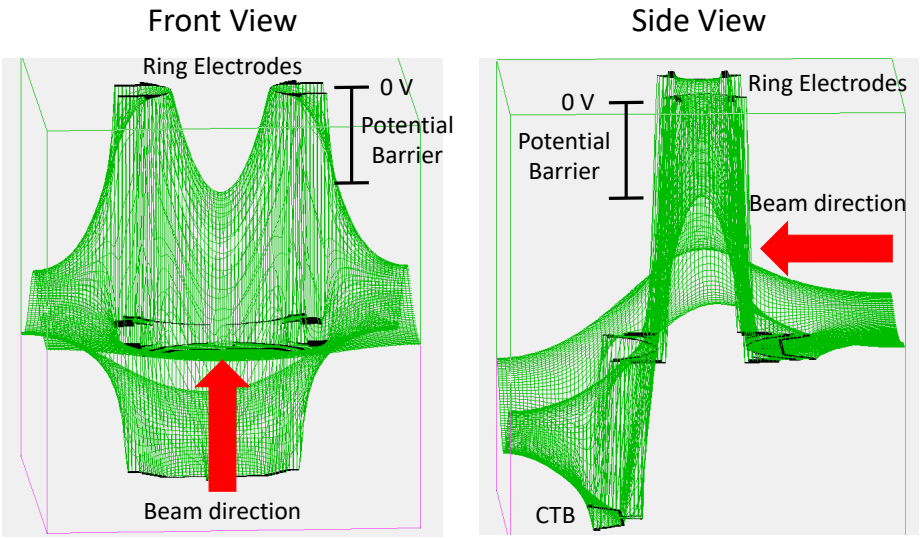

Figure 5.12: The potential barrier used to measure the beam's energy profile. The equipotential lines are shown in green. The trap electrodes are shown in black. The direction of the ion beam is indicated with a red arrow. The potential barrier in this figure is produced by biasing CTB at -33 V, grounding the ring electrodes, and biasing all other trap electrodes at -20 V.

to pass over. The potential barrier produced by biasing CTB at -33 V, grounding the ring electrodes, and biasing all other trap electrodes at -20 V is shown in Fig. 5.12.

A plot of the fraction of beam remaining on CTB as function of the potential barrier is shown in Fig. 5.13. At a potential barrier of -20.6 V, just over 90% of the beam is delivered to the back of the trap. As the barrier increases, the efficiency begins to decrease. The majority of the losses occur between -7.5 and 0 V. This can be seen by examining the derivative of the remaining beam on CTB. This 7.5 V difference is roughly the axial energy spread of the ions just before entering the trap. The spread is due to a combination of a lack of cooling from the cooler and buncher since DC beam is being used as well as a pickup of radial energy as the ions enter the magnetic field. The latter effect can be reduced with further beamline tuning studies. As mentioned earlier, the spread in the beam energy can lead to the smearing of FT-ICR signals, which is investigated later in this chapter.

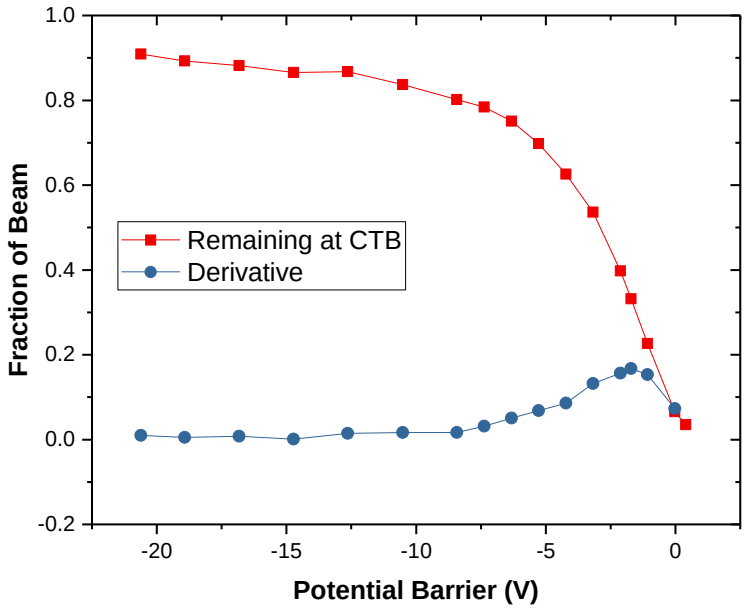

Figure 5.13: The fraction of beam remaining on CTB as a function of the potential barrier is indicated with red squares. The numerical derivative of this curve is indicated with blue circles.

5.3 SIPT General Studies

5.3.1 TOF-ICR with SIPT

In addition to FT-ICR detection, SIPT was designed to allow for the use of TOF-ICR, which is useful for optimizing steering and focusing as well as trap voltages and timings. The SIPT BOB3 MCP used to perform TOF-ICR is set up in the Daly configuration [87]. Due to the cryogenic FT-ICR detection circuit, ions must be extracted from the same side of the trap which they entered and pass through the same injection optics. In order to do this, the Daly collector, the Lorentz steerers [71], and several of the drift tubes must be switched while the ions are in the trap. A conceptual overview of the reverse extraction configuration is presented in Fig. 5.14. As ions pass the MCP upon injection, the Daly collector is set to

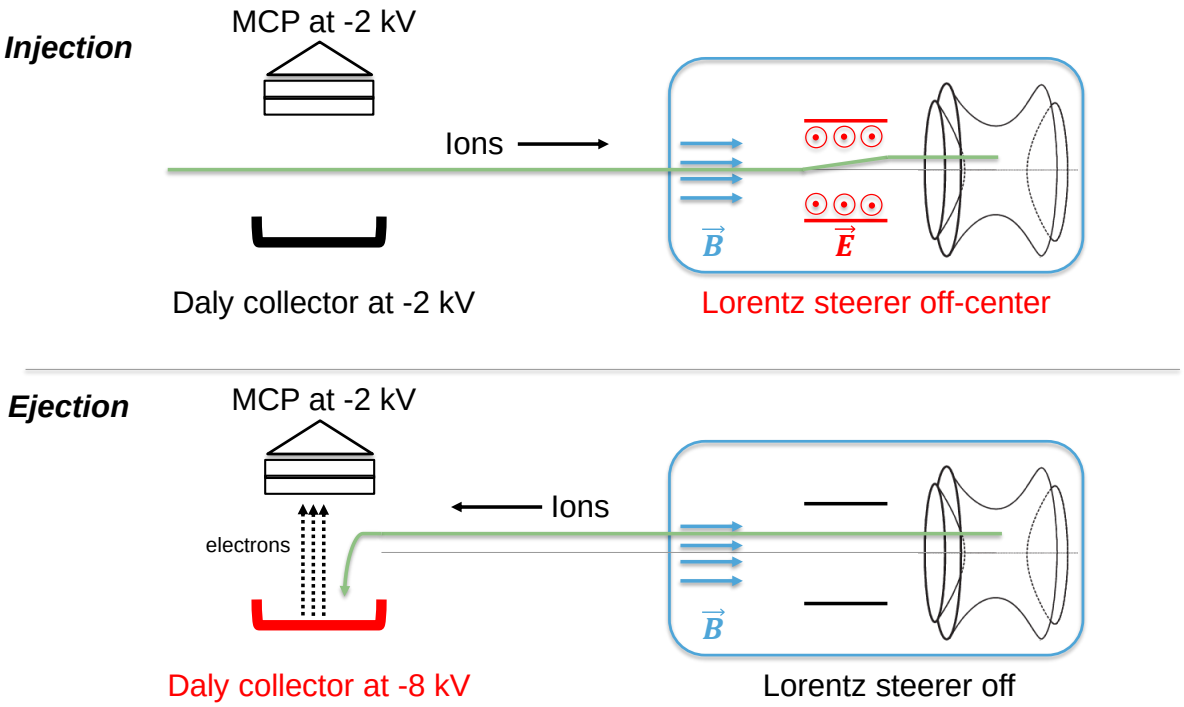

Figure 5.14: Conceptual overview of reverse extraction from the Penning trap for TOF-ICR. Figure adapted from [8, 12].

the same voltage as the MCP (-2 kV), and the Lorentz steerers are set to their off-center values to give the ions initial magnetron motion [119]. Once the ions enter the trap, the Daly collector is set to -8 kV, and the Lorentz steerers are set to 0 V to remove the $\vec{E} \times \vec{B}$ force. Several of the drift tubes near the maximum of the magnetic field gradient (drift tubes 3,4, and 5) are also switched to voltages closer to ground to allow for slower extraction leading to higher resolution in the time of flight and larger time-of-flight effects in the resonances. $^{39}K^{+}$ was used to obtain the first TOF-ICR resonance at cryogenic temperatures. Fig. 5.14 shows a 50 ms excitation TOF-ICR resonance. A relative uncertainty of $\delta\nu_c/\nu_c = 2 \times 10^{-7}$ was obtained from the fit to the data.

It is important to note the difficulties that occured when using the reverse extraction mode. Switching a few kV within a magnetic field can lead to sparking. To help remedy this

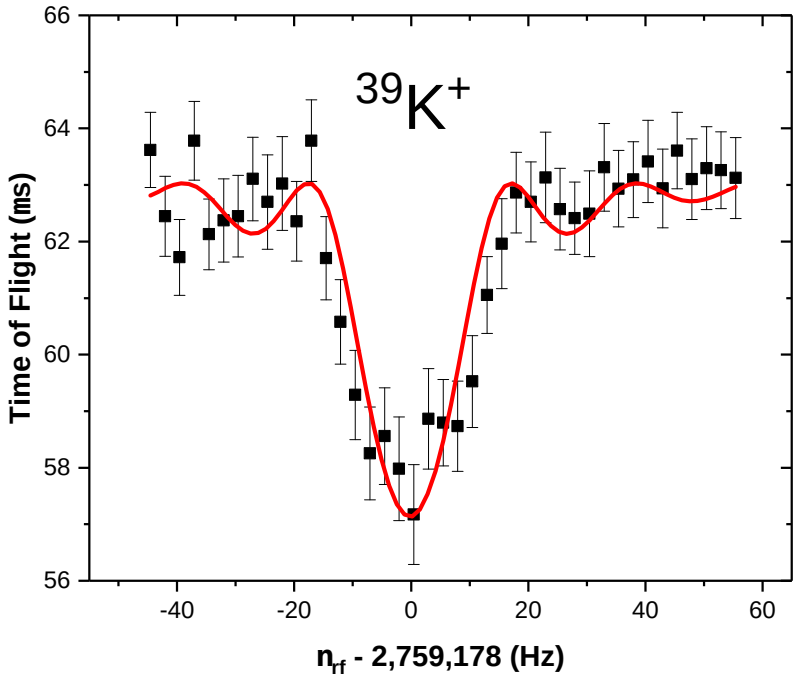

Figure 5.15: 50 ms TOF-ICR resonance of $^{39}K^+$ at cryogenic temperatures.

effect, the electrodes must have sufficient time to switch. This leads to extra trap storage time on the order of 100 ms, which is not ideal for certain beamline tuning measurements. Furthermore, low-noise HV switches for the Daly collector, which is switching 6 kV, are expensive and fragile.

5.3.2 Resonator Response

The response of the resonator circuit has been thoroughly tested at cryogenic temperatures. One method for testing the resonator response is to feed in 20 mVpp noise over a 2 MHz bandwidth to one of the rf drive segments of the trap's ring electrode. Using this method, the resonator response observed at 5.2 K can be seen in Fig. 5.16. The quality factor was measured by fitting the response with a Lorentz function and found to be 2784, exceeding

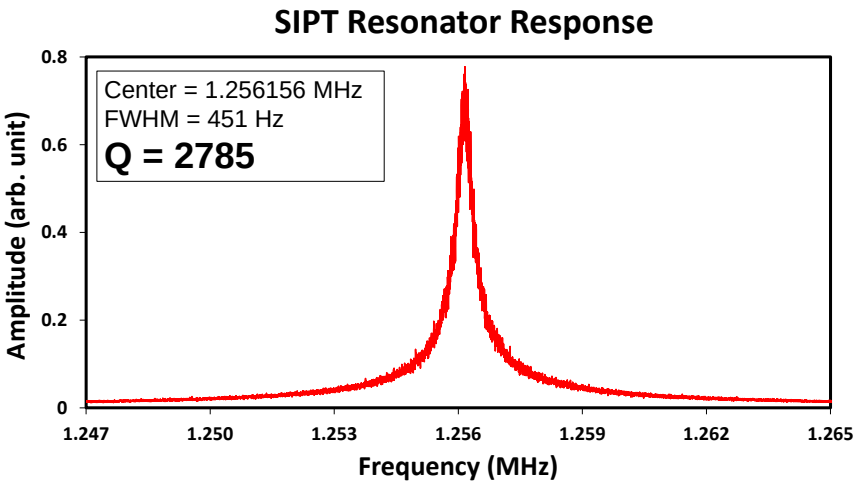

Figure 5.16: Frequency domain response of the SIPT narrowband FT-ICR cryogenic detection circuit operating at 5.2 K. Figure adapted from [8, 12].

the quality factor of ~ 2000 advertised by the manufacturer.

Using the resonator frequency and the known value of the inductance $L = 600$ μH, the paracitic capacitance of the trap electrodes and wires can be calculated resulting in a value of 28 pF. The paracitic capacitance is very sensitive to any changes to the detection circuit, so the value typically has to be remeasured after each change. To make optimal use of SIPT, the center frequency of the resonator should be tunable to allow for measurements of multiple isotopes at different mass numbers during an experimental campaign. This is accomplished with a varactor diode, which provides voltage-dependent capacitance adjustments.

5.3.3 Varactor Studies

The cryogenic amplifier is equipped with two GaAs high-Q varactor diodes in parallel at the input of the amplifier, which should provide a tunable capacitor. However, the combination of high magnetic field strength and low temperatures led to a malfunction in the varactor that caused a significant decrease in the quality factor of the resonator circuit.

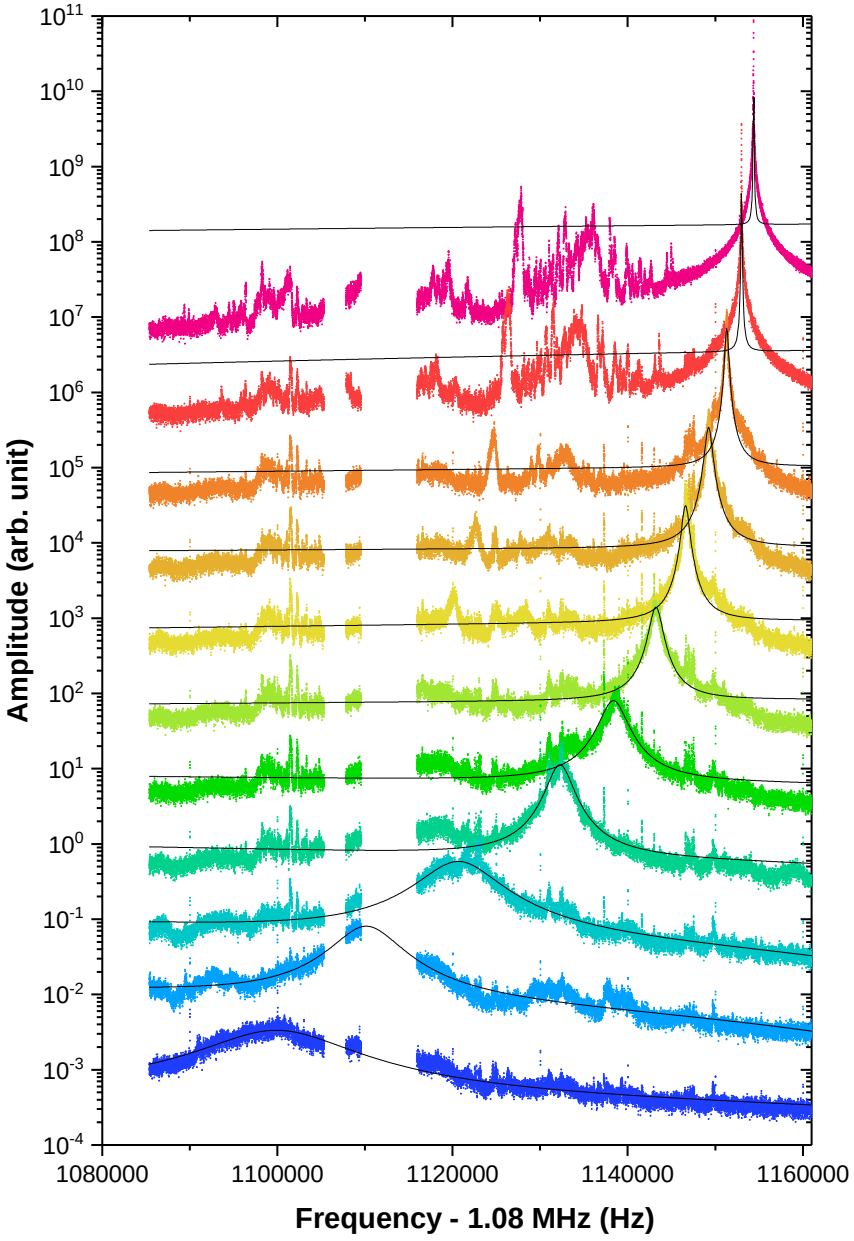

Figure 5.17: Resonator response as a function of frequency for varactor voltages between 0 and 10 V. Each response is offset by a factor of 10 from the previous voltage response. Two large noise peaks have been removed from the plot.

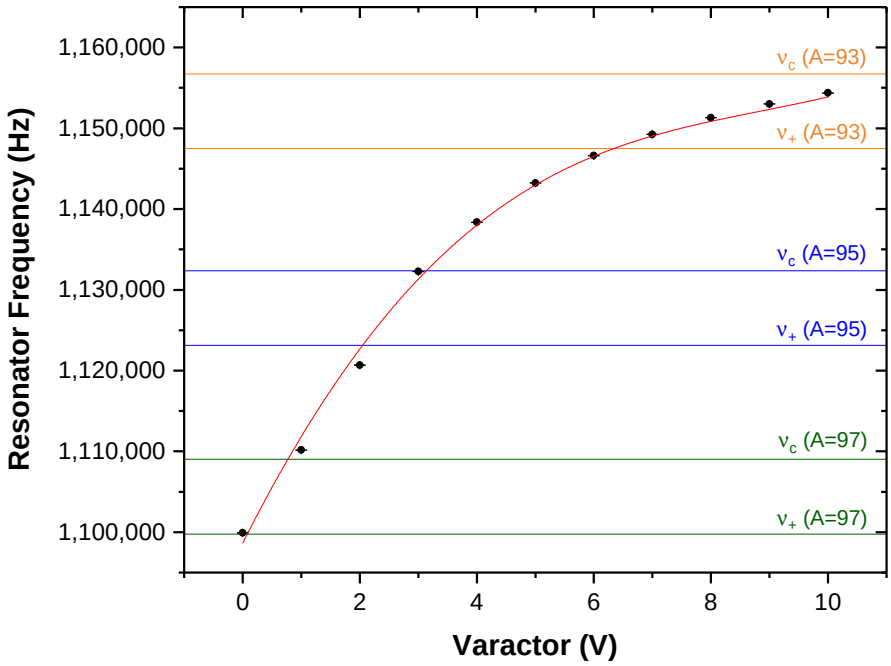

Figure 5.18: Resonator frequency as a function of varactor voltage.

A replacement varactor was installed that mitigates the problems caused by the original varactor. The new varactor adds between 1.3 pF and 6 pF of capacitance, which is adjustable through the reverse biasing voltage (10 V provides 1.3 pF while 1 V provides 6 pF). Fig. 5.17 shows the resonator response as a function of frequency for 1 V varactor voltage steps from 0 V to 10 V. Fig. 5.18 shows the resonator frequency as a function of the varactor voltage. This measurement was taken with an extra 6.1 pF of capacitance added in parallel to the detection circuit to achieve a frequency range that would cover $A = 96$. Nominally, the resonator circuit is near $A = 85$.

One feature that is evident from Fig. 5.17 is the decrease in the quality factor as the varactor biasing voltage decreases. Fig. 5.19 (Left) shows the Q-factor as a function of the varactor voltage. At low varactor voltages, the Q-factor is well below 1000. This lowers

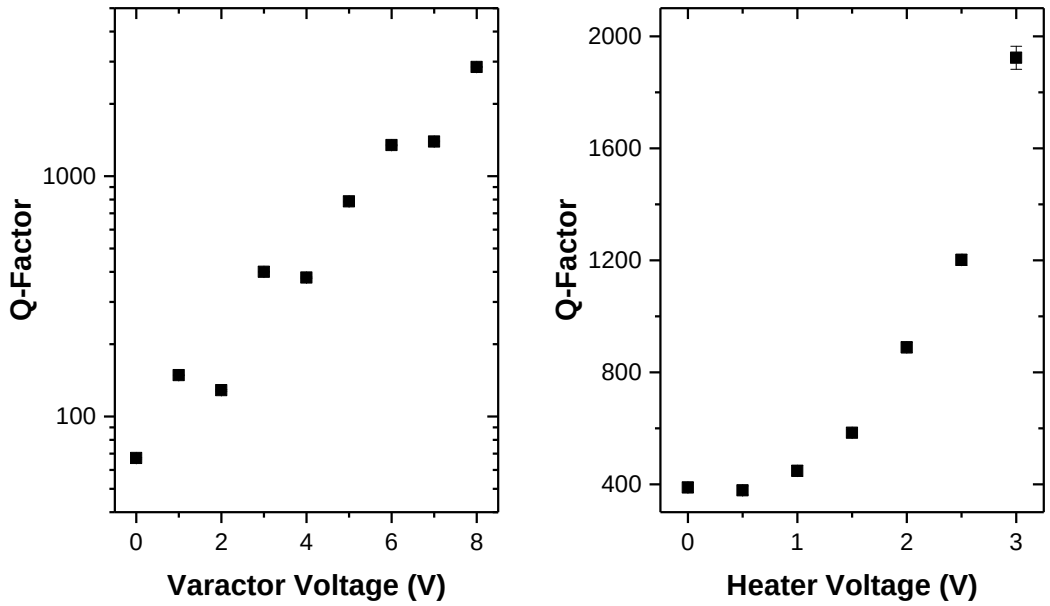

Figure 5.19: (Left) Q-factor as a function of the varactor voltage. (Right) Q-factor as a function of the varactor heater voltage for a varactor voltage of 4 V.

the signal-to-noise ratio, which could lead to difficulties detecting single ions. To raise the Q-factor, a controllable heater has been attached to the varactor, which allows for localized temperature increases. The temperature of the varactaor and the Q-factor can be raised by increasing the heater voltage as seen in Fig. 5.19 (Right). 1 V supplies 100 μW of power while 10 V supplies 10 mW.

5.3.4 Trap Tuning

A non-harmonic electric field can cause frequency shifts that lead to lower accuracy for a Penning trap. The non-harmonic imperfections originate from the holes in the end cap electrodes and the truncation of the hyperboloid structure. To study the effects of these imperfections,

the octupole and dodecapole terms of the trapping potential must be considered [76]:

$$V_4(\rho, z) = C_4\left(\frac{U_0}{2d_0^4}\right)\left[z^4 - 3z^2\rho^2 + \frac{3}{8}\rho^4\right], \tag{5.6}$$

$$V_6(\rho, z) = C_6\left(\frac{U_0}{2d_0^6}\right)\left[z^6 - \frac{15}{2}z^4\rho^2 + \frac{45}{8}z^2\rho^4 + \frac{5}{16}\rho^6\right], \tag{5.7}$$

where C_4 and C_6 are the octupole and dodecapole correction strengths, respectively, and U_0 is the potential difference between the endcap and ring electrodes. The higher-order terms scale with $1/d^l$ where l indicates the order of the expansion ($l = 2$ corresponds to the quadrupole term of the expansion, for example). Hence, higher-order terms become increasingly smaller, so they are typically not considered. The frequency shifts caused by these higher-order terms are [67, 76]:

$$\Delta\nu_\pm \approx \pm\frac{3}{4}\frac{C_4}{d_0^2}\nu_-\left[\rho_\pm^2 + 2\rho_\mp^2 - 2z^2\right], \tag{5.8}$$

$$\Delta\nu_\pm \approx \frac{15}{16}\frac{C_6}{d_0^4}\nu_-\left[-3z^4 + 6z^2(\rho_\pm^2 + 2\rho_\mp^2) - (\rho_\pm^4 + 3\rho_\mp^4 + 6\rho_+^2\rho_-^2)\right], \tag{5.9}$$

for the octupole and dodecapole terms, respectively. Using $\nu_c = \nu_+ + \nu_-$, one can estimate the shift on ν_c:

$$\Delta\nu_c \approx \frac{3}{4}\frac{(\rho_-^2 - \rho_+^2)}{d_0^2}\nu_-\left[C_4 + \frac{5}{2}\frac{C_6}{d_0^2}(3z^2 - \rho_+^2 - \rho_-^2)\right]. \tag{5.10}$$

There are two ways to minimize the frequency shifts seen in eq. 5.10. The first is to ensure that $\rho_- = \rho_+$. This method is infeasible for TOF-ICR since it relies on the conversion of one motion into the other. However, it is possible for FT-ICR. In fact, a quadrupole excitation at the frequency $\nu_+ - \nu_-$ would accomplish this. While this drive frequency has been tested with simulations, it has not been explored experimentally with SIPT due to the small ν_c

signal strengths. The second method is to minimize C_4 and C_6. This can be accomplished with the correction ring and correction tube electrodes. The optimal correction electrode voltages can be determined numerically using SIMION. The voltages are calculated relative to the trap depth, which for SIPT, is simply the end cap voltage since the ring electrodes are grounded. The SIPT calculated values are 0.353 for the correction ring and 1.695 for the correction tube. For an end cap voltage of 22.5 V, which is the current end cap voltage used in SIPT, these ratios correspond to correction ring and tube voltages of 7.94 V and 38.14 V, respectively.

Methods for minimizing these coefficients experimentally have been outlined before [120, 121]. They involve scanning the voltages applied to the correction electrodes while minimizing frequency shifts in ν_+ as a function of the capture time (e.g. the time at which the trapping voltage is switched from a low voltage allowing ions to enter the trap to a high voltage creating the quadrupolar electrostatic potential) and ν_c as a function of the quadrupole excitation amplitude. Similar techniques have been explored with SIPT; the measurement process is outlined below.

For a set of voltages applied to the correction electrodes, a measurement of the reduced cyclotron frequency ν_+ as a function of the capture time is performed. This measurement probes the dependence of ν_+ on the ion's axial location in the trap. Poor capture times lead to large axial oscillations allowing access to regions of the electric field where imperfections are most likely to be present. Results from this measurement for several correction tube values can be seen in Fig. 5.20 (Left). A quadratic fit to this data can be used to extract a concavity. Minimal frequency shifts are observed when the concavity is zero. A measurement of ν_+ as a function of the dipole rf-excitation amplitude at a frequency near the ion's ν_+ frequency probes the dependence of ν_+ on the ion's radial location in the trap. Results from

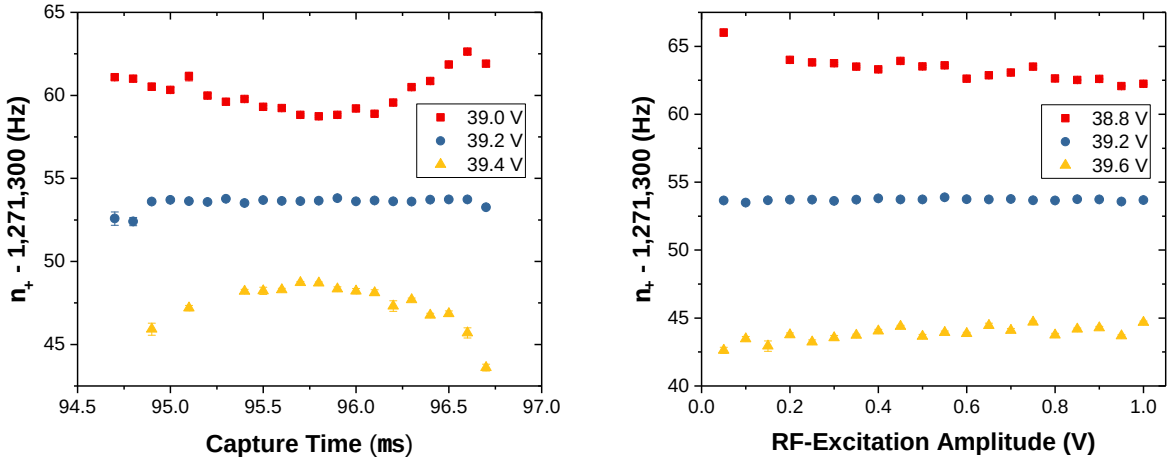

Figure 5.20: Trap tuning measurements performed with SIPT. Measurements of the reduced cyclotron frequency as a function of the capture time (Left) and rf-excitation amplitude (Right) are shown. The correction ring is set to 9.0 V. The correction tube voltages are shown in the legends.

this measurement for several correction tube values can be seen in Fig. 5.20 (Right). A linear fit to this data can be used to extract a slope. Minimal frequency shifts are observed when the slope is zero.

These measurements are performed for a range of correction electrode voltages. For a given value of one of the correction electrodes, a plot of the concavities and slopes as a function of the other correction electrode is produced. A linear fit to these data sets allows for the determination of the voltage that gives either zero slope or zero concavity. Each type of measurement will then produce a range of possible optimal values. The optimal values for each measurement type are shown in Fig. 5.21. The optimal values typically follow a linear trend, which intersect at some point. The intersection is taken as the optimal value since it is simultaneously minimizing frequency shifts caused by axial oscillations and large radii. The intersection in Fig. 5.21 gives a ring voltage of 9.20 V and a tube voltage of 39.37 V. The correction ring and tube voltages are respectively 16% and 3% larger than the calculated

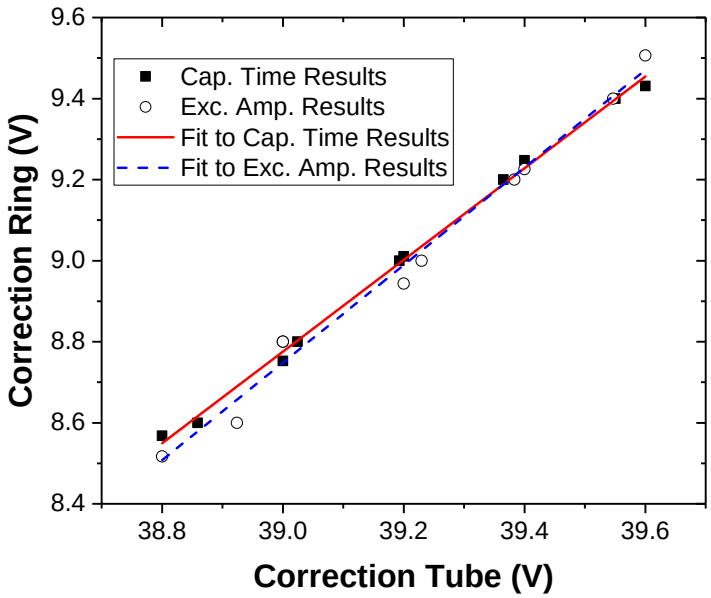

Figure 5.21: Correction electrode voltages that minimize ν_+ frequency shifts for capture time and rf-excitation amplitude measurements along with linear fits to these results are shown. The intersection of these lines should provide the optimal voltages that minimize the non-harmonic imperfections in the electrostatic trapping field.

values. Improvements to this method will be possible once ν_c is more accessible to SIPT. Then, measurements of ν_c at several quadrupole rf-excitation amplitudes can be performed as well.

5.3.5 Contaminant Identification with SIPT

Beam from the gas stopping facility has been sent to SIPT to perform contaminant identification. Ions of a given mass-to-charge ratio A/Q extracted from the gas cell can be trapped in SIPT and excited with a short dipole rf-excitation at the ν_+ frequency of an ion with the same mass-to-charge ratio. The short rf-excitation excites the ν_+ radius of the majority of the ions with the given A/Q. An example FT-ICR spectrum taken from the ANL gas cell with $A/Q = 95$ can be seen in Fig. 5.22.

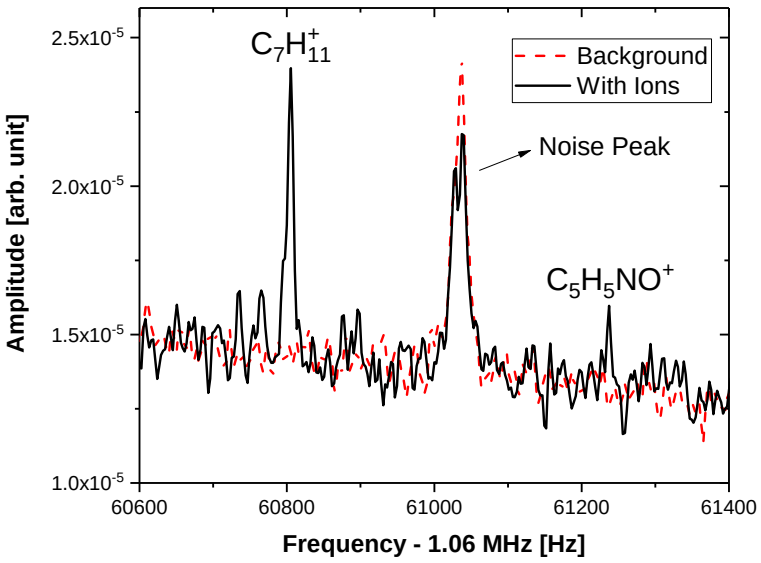

Figure 5.22: An FT-ICR spectrum taken with ions from the ANL gas cell at a mass-to-charge ratio $A/Q = 95$ is shown with a solid-blick line. A background spectrum is shown with a dashed-red line for comparison. The identified contaminant labels are displayed as well.

Contaminant identification using the traditional TOF-ICR technique is rather slow because TOF-ICR is an averaging technique. Typically the contaminants must be identified one at a time starting with the most abundant. Once a contaminant is identified, it can be cleaned with a dipole excitation. The process is then repeated until all contaminants are identified. With FT-ICR, multiple contaminants can be identified at once as can be seen in Fig. 5.22. SIPT will thus allow for significant reductions in the time required for contaminant identification during rare isotope beam experiments.

5.4 Single Ion Sensitivity Studies

5.4.1 Simulation Studies

The signal strength created by an ion on the ring electrodes of a Penning trap should be sensitive to the ion's location within the trap. To develop an intuition for this sensitivity, a single ion signal strength simulator was prepared. The surface charge density $\sigma(\rho, z)$ induced on the ring electrodes by an ion at a given radius ρ and axial position z relative to the center of the trap was calculated using SIMION. The surface charge was then integrated over one axial period to obtain a signal strength S for a single ion:

$$S = \int_0^1 \sigma(\rho, z\sin(2\pi t))\, dt - \int_0^1 \sigma(0, z\sin(2\pi t))\, dt. \tag{5.11}$$

The values for ρ and z were chosen from Gaussian distributions with means μ_ρ, μ_z and standard deviations σ_ρ, σ_z that can be varied. A Poisson distribution with a variable mean was used to determine the number of ions in the trap. The signal strength S from each ion was then added to produce a total signal strength. Fig. 5.23 shows a histogram of the signal strengths with the following parameters: a mean number of ions equal to 1, $\mu_\rho = 3$ mm, $\sigma_\rho = 0.125$ mm, $\mu_z = 0$ mm, and $\sigma_z = 1$ mm. A total of 5000 data points were simulated. The histogram is color coded based on the number of ions in the trap. The sum of all the data is also shown as a blue line. As expected, the heights of the ion peaks follow the Poisson distribution used to generate the number of ions in the trap. The spread in the ion peaks is due to the variation in the ions' positions. The peaks can be fit with Gaussian distributions and relationships can be seen by plotting the means and standard deviations for each peak.

Fig. 5.24 displays the means and standard deviations for each ion peak in Fig. 5.23 along

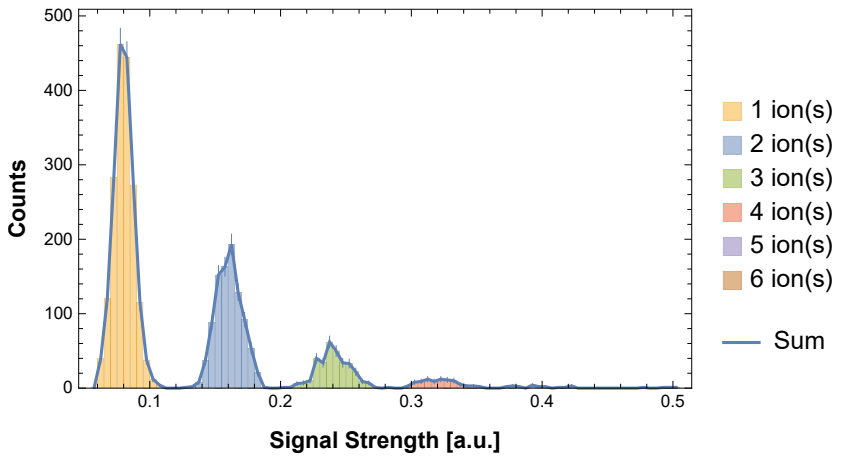

Figure 5.23: Simulated signal strength histogram with $\mu_\rho = 3$ mm, $\sigma_\rho = 0.125$ mm, $\mu_z = 0$ mm, and $\sigma_z = 1$ mm. A total of 5000 data points were simulated.

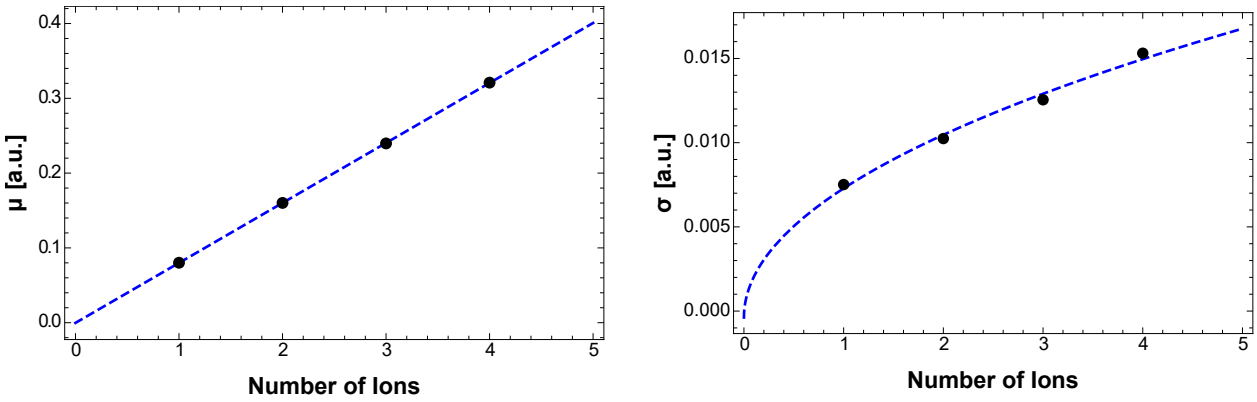

Figure 5.24: The means (Left) and standard deviations (Right) of Gaussian distributions fit to each ion peak in Fig. 5.23. A linear fit to the means and $\sqrt{N}$ fit to the standard deviations where N is the number of ions in the trap are also shown.

with fits to these quantities. From Fig. 5.24, a clear linear relationship between the means of the ion peaks is observed. The spacing between the ion peaks is identical, and the intercept is consistent with zero. The standard deviations of the ion peaks are proportional to $\sqrt{N}$ where N is the number of ions in the trap; the intercept is again consistent with zero. The ion peaks quickly smear together with larger uncertainties in the ions' positions. The radial uncertainty is particularly sensitive. Fig. 5.25 shows a second simulated signal strength histogram. The parameters are the same of that in Fig. 5.23 except σ_ρ, which is three times larger. Without the color guide, the ion peaks would be difficult to disentangle. The

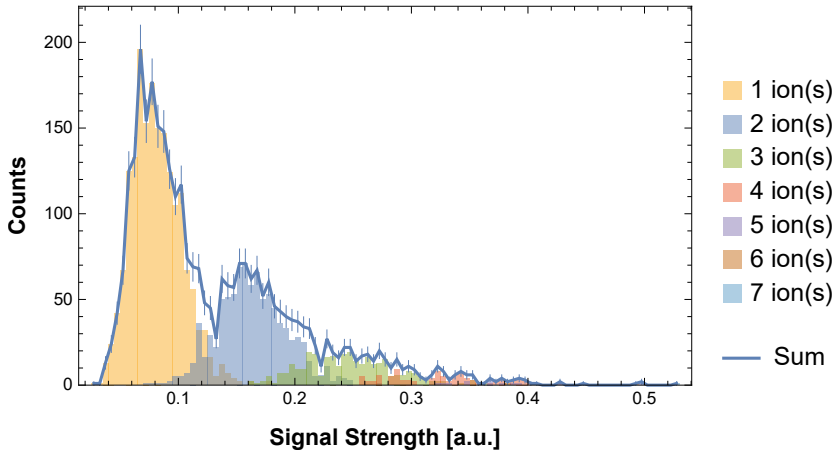

Figure 5.25: Simulated signal strength histogram with $\mu_\rho = 3$ mm, $\sigma_\rho = 0.375$ mm, $\mu_z = 0$ mm, and $\sigma_z = 1$ mm. A total of 5000 data points were simulated.

Gaussian fit parameters to each peak, however, still follow the trends observed in Fig. 5.24.

5.4.2 Experimental Results

To show single ion sensitivity experimentally, the signal strength must be quantified. This quantity can be extracted from the function used to fit the data:

$$y = a + b(\nu - \nu_0) + c(\nu - \nu_0)^2 + d\frac{\gamma}{(\nu - \nu_0)^2 + \gamma^2} \tag{5.12}$$

where a, b, c, d, γ, and ν_0 are free parameters. The fit contains a quadratic function for background and a Lorentzian function for the ion signal. Currently, the experimental signal strength is determined in two ways. The first signal strength metric is the area of the Lorentzian, which is found to be $d\pi$ when integrating the Lorentzian term from $-\infty$ to $+\infty$. The second metric is the difference between the signal component and background component of the fit evaluated at ν_0: $d/\gamma - a$.

To perform a single ion search, FT-ICR data is collected with and without ions. Using the LEBIT data analysis software EvaFFT, a fit can be performed on each shot, i.e. a single

release of ions from the cooler and buncher to the Penning trap. To perform the fits, an FFT amplitude threshold along with a frequency range must be selected. After choosing these quantities and fitting all the data, the signal strengths can be calculated for each shot and plotted as a histogram. Fig. 5.26 shows normalized experimental Lorentzian area histograms for both ion data and background data. The Lorentzian area data has gone through a set of filters on the individual fit parameters to remove poor quality data. There are 2646 counts in the ion data and 237 counts in the background data. This data was taken with a 0.25 mm in diameter collimator placed within DT8 just before the trap entrance to ensure minimal spread in the ions' radii when entering the trap.

The incoming beam rate was kept low to ensure that each shot had no more than a few ions. Because of this rate limit, the ion data should have some number of shots taken with no ions present in the trap. These shots are removed through a background subtraction routine. The background data is fit with a Gaussian distribution (see Fig. 5.26 for an example background fit). This Gaussian distribution is then used to subtract shots from the ion data. The resulting background subtracted Lorentzian area histogram can be seen in Fig. 5.27. Note in all cases the error bars are given by $\sqrt{N}$ where N is the number of data points in each bin. In Fig. 5.26, the error bars are normalized to the total number of data points for each data set.

The background subtracted histogram was then fit with five Gaussians to extract the location of peaks corresponding to a given number of ions in the trap (see Fig. 5.27). The means and amplitudes of the fits were all allowed to vary within some range that is currently chosen somewhat arbitrarily. The initial guess for the width of the first ion peak fit along with its bounds were used to scale the initial guesses for the widths and their bounds for the rest of the fits. The sum of the five Gaussians is shown with a green dotted line in Fig. 5.27.

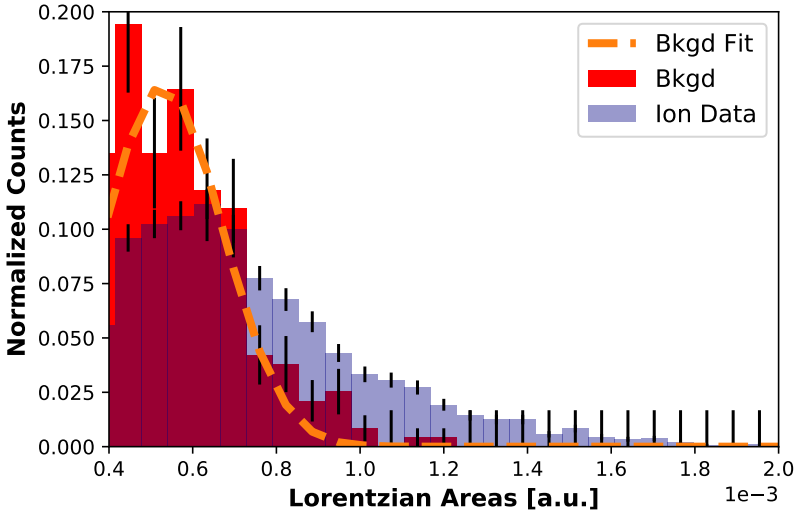

Figure 5.26: Experimental Lorentzian area histograms for both background fits (red), and ion data fits (purple). A fit to the background data is shown in orange. Error bars are calculated using $\sqrt{N}$ where N is the number of data points in each bin and normalized to the total number of data points for each data set.

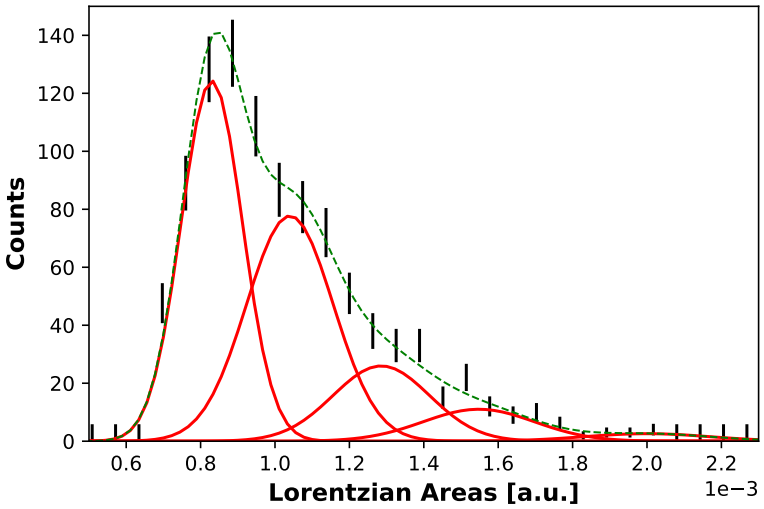

Figure 5.27: Background subtracted experimental Lorentzian area histogram with error bars (black lines) along with Gaussian fits to the expected location of the ion peaks (red). The sum of the five Gaussians is shown in green.

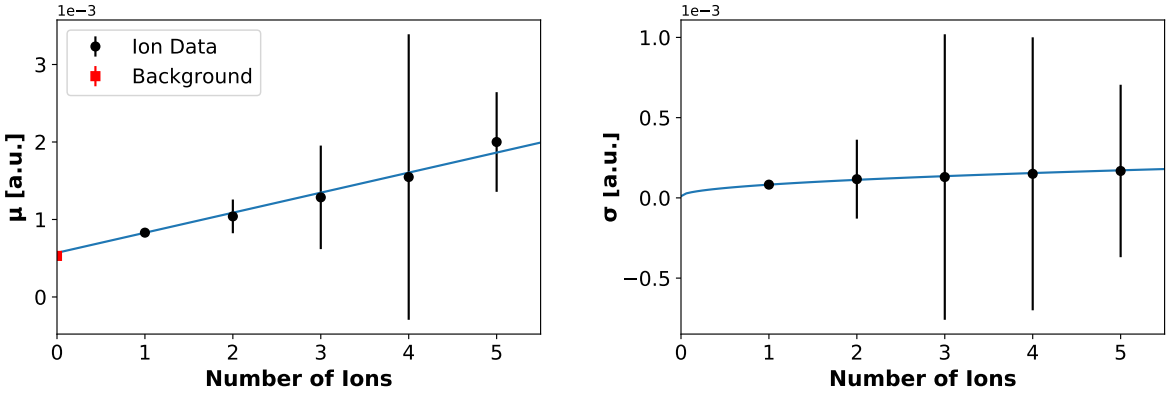

Figure 5.28: The means (Left) and standard deviations (Right) of the Gaussian fits to each ion peak in Fig. 5.27. A linear fit to the means and $\sqrt{N}$ fit to the standard deviations where N is the number of ions is also shown. The mean of the background data is shown on the left plot as well.

The means and standard devations of the five Gaussians in Fig. 5.27 can be plotted as a function of the number of ions in the trap. This is shown in Fig. 5.28. The means as a function of ion number were fit with a line shown in blue, which they follow well. The y-intercept of the line is $5.7(2) \times 10^{-4}$ while the background peak mean is $5.3(1) \times 10^{-4}$. These are expected to agree and only differ by $1.8\,\sigma$. The widths of the Gaussians have large uncertainties, so it is difficult to compare them to a $\sqrt{N}$ fit, though this is done in Fig. 5.28 (Right).

Direct experimental evidence of single ion sensitivity appears to be within reach for SIPT. More work is still needed to better separate the ion peaks from each other and remove poor fits from the analysis. Fig. 5.29 shows two examples of shots that fall within the single ion peak in Fig. 5.27. While the signal on the left looks like an actual single ion signal, the signal on the right may be only noise. A visual examination of this fit would result in it being rejected from the data set. However, due to the large number of statistics needed to verify single ion sensitivity, it is not feasible to check each fit by eye. With the analysis

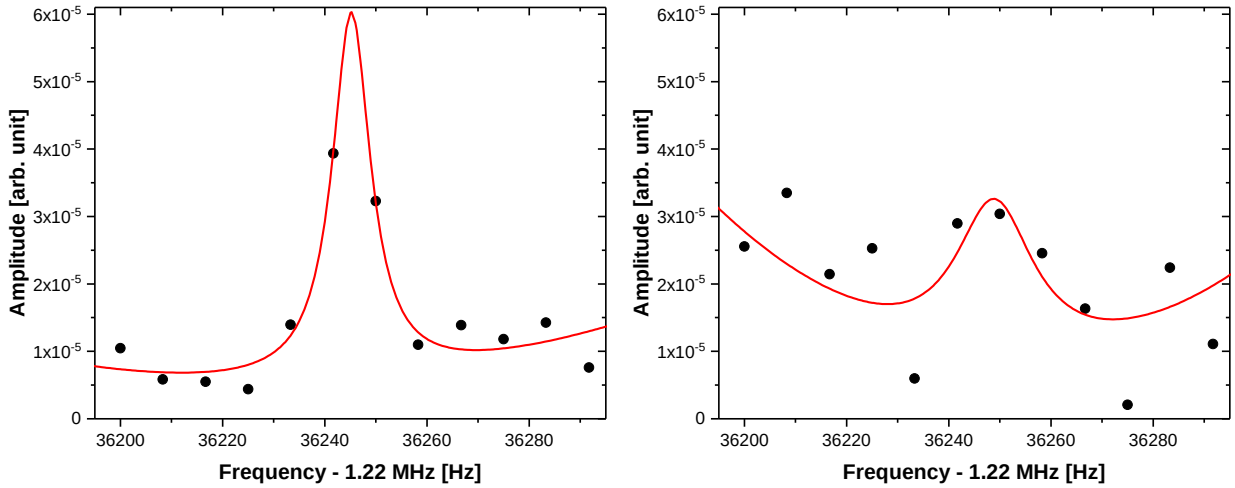

Figure 5.29: $^{85}Rb^{+}$ FT-ICR signals from shots that fall in the single ion peak in Fig. 5.27. The left and right signals have Lorentzian areas of 7.8×10^{-4} and 7.0×10^{-4}, respectively. Although the calculated signal strengths are similar, the quality of the resonances are drastically different.

above, there are many parameters that can be tuned as well: the fit parameter filters, zero padding of the FFT data, and the threshold and frequency limits used in EvaFFT to filter the raw FFT data. Thus, a more robust analysis code that systematically scans each of these parameters may need to be developed. Furthermore, because the noise level can vary from shot to shot, a thorough analysis of the a, b, and c background fit parameters on background data is needed to constrain these parameters which would help eliminate shots with extreme noise levels.

Another area of improvement could come from background reduction or an increased signal-to-noise ratio. A background study of the frequency spectrum showed that adjustments to the cryogenic amplifier voltages do not have a large impact on the shot-to-shot variation in the background. Hence, a more robust amplifer may be needed. Further trap tuning studies would also be useful for better controlling the ions' frequency. Spread in the detected ion frequency can lead to wider FT-ICR signals and lower signal strengths.

A few more steps need to be taken to finalize SIPT for FRIB. Arbitrary function generators need to be installed to allow for targeted dipole cleaning of contaminant ions, and the detection electrodes need to be rewired and tested to allow for ν_c pickup. Strategies for these last items have been established, setting the path to prepare SIPT for the first FRIB experiments.

Chapter 6

Conclusion

The first precision mass measurement of the neutron-deficient $N = Z$ nucleus ^{80}Zr was performed via Penning trap mass spectrometry at the LEBIT facility. The measurement revealed a significant enhancement in the binding energy of ^{80}Zr, which, through binding-energy indicators, is attributed to the deformed double shell closure at $N = Z = 40$ and an increase in the Wigner energy of this exotic system. A statistical Bayesian model mixing analysis employing eleven global nuclear mass models demonstrated difficulties with reproducing the observed mass anomaly using current theory. While successful, the measurement was difficult with the current destructive PTMS techniques employed at LEBIT due to the low ^{80}Zr production rate at the NSCL.

More exotic isotopes with even lower production rates are expected to be produced with FRIB. To prepare for these conditions, the single ion Penning trap has been developed at LEBIT and is going through its final commissioning stages. SIPT is the first rare isotope mass spectrometer to make use of the non-destructive FT-ICR detection technique. Beamline simulations and experimental studies, hardware upgrades, and FT-ICR signal analyses have placed SIPT within reach of definitive proof of single ion sensitivity. Trap tuning studies and detection scheme simulations have prepared SIPT for successful rare isotope mass measurements with FRIB. Combining the capabilities of both the 9.4 T Penning trap and SIPT with FRIB, LEBIT is prepared to make significant contributions to nuclear science for

the foreseeable future.

BIBLIOGRAPHY

BIBLIOGRAPHY

[1] W.J. Huang, M. Wang, F.G. Kondev, G. Audi, and S. Naimi. The AME 2020 atomic mass evaluation (I). Evaluation of input data, and adjustment procedures*. *Chin. Phys. C*, 45(3):030002, Mar 2021.

[2] W. Nazarewicz, J. Dudek, R. Bengtsson, T. Bengtsson, and I. Ragnarsson. Microscopic study of the high-spin behaviour in selected $A \simeq 80$ nuclei. *Nucl. Phys. A*, 435(2):397 – 447, 1985.

[3] S. Goriely, N. Chamel, and J. M. Pearson. Further explorations of Skyrme-Hartree-Fock-Bogoliubov mass formulas. XIII. The 2012 atomic mass evaluation and the symmetry coefficient. *Phys. Rev. C*, 88:024308, Aug 2013.

[4] W. Satuła, D.J. Dean, J. Gary, S. Mizutori, and W. Nazarewicz. On the origin of the Wigner energy. *Phys. Lett. B*, 407(2):103–109, 1997.

[5] E. Leistenschneider. *Dawning of nuclear magicity in $N = 32$ seen through precision mass spectrometry*. PhD thesis, University of British Columbia, 2019.

[6] M. König, G. Bollen, H.-J. Kluge, T. Otto, and J. Szerypo. Quadrupole excitation of stored ion motion at the true cyclotron frequency. *International Journal of Mass Spectrometry and Ion Processes*, 142(1):95 – 116, 1995.

[7] Z. Meisel, A. Hamaker, G. Bollen, B.A. Brown, M. Eibach, K. Gulyuz, C. Izzo, C. Langer, W.-J Ong, D. Puentes, M. Redshaw, R. Ringle, R. Sandler, H. Schatz, S. Schwarz, C.S. Sumithrarachchi, A.A. Valverde, and I.T. Yandow. Improved Nuclear Physics Near $A = 61$ Refines Urca Neutrino Luminosities in Accreted Neutron Star Crusts. 2021.

[8] Alec Hamaker, Georg Bollen, Martin Eibach, Christopher Izzo, Daniel Puentes, Matthew Redshaw, Ryan Ringle, Rachel Sandler, Stefan Schwarz, and Isaac Yandow. Sipt - an ultrasensitive mass spectrometer for rare isotopes. *Hyperfine Interactions*, 240(1):34, Apr 2019.

[9] S. George, K. Blaum, F. Herfurth, A. Herlert, M. Kretzschmar, S. Nagy, S. Schwarz, L. Schweikhard, and C. Yazidjian. The Ramsey method in high-precision mass spectrometry with Penning traps: Experimental results. *International Journal of Mass Spectrometry*, 264(2):110 – 121, 2007.

[10] W. Satuła, J. Dobaczewski, and W. Nazarewicz. Odd-Even Staggering of Nuclear Masses: Pairing or Shape Effect? *Phys. Rev. Lett.*, 81:3599–3602, Oct 1998.

[11] Y. Y. Zong, C. Ma, Y. M. Zhao, and A. Arima. Mass relations of mirror nuclei. *Phys. Rev. C*, 102:024302, Aug 2020.

[12] C. Izzo. *Mass Measurements of neutron-rich Cobalt Isotopes Beyond N=40 and the development of a Single Ion Penning Trap Mass Spectrometer for Rare Isotopes*. PhD thesis, Michigan State University, 2018.

[13] D. Lunney, J. M. Pearson, and C. Thibault. Recent trends in the determination of nuclear masses. *Rev. Mod. Phys.*, 75:1021–1082, Aug 2003.

[14] R. F. Casten. Approaching nuclei through multiple perspectives and diverse models: Patterns, symmetries, interactions. *Frontiers of Physics*, 13:132104, Sep 2018.

[15] I. Angeli and K.P. Marinova. Table of experimental nuclear ground state charge radii: An update. *Atomic Data and Nuclear Data Tables*, 99(1):69–95, 2013.

[16] Maria G. Mayer. On Closed Shells in Nuclei. *Phys. Rev.*, 74:235–239, Aug 1948.

[17] Otto Haxel, J. Hans D. Jensen, and Hans E. Suess. On the "Magic Numbers" in Nuclear Structure. *Phys. Rev.*, 75:1766–1766, Jun 1949.

[18] Alexander Belyaev and Douglas Ross. *The Nuclear Shell Model*, pages 53–66. Springer International Publishing, 2021.

[19] National Research Council. *Nuclear Physics: Exploring the Heart of Matter*. The National Academies Press, Washington, DC, 2013.

[20] Takaharu Otsuka, Alexandra Gade, Olivier Sorlin, Toshio Suzuki, and Yutaka Utsuno. Evolution of shell structure in exotic nuclei. *Rev. Mod. Phys.*, 92:015002, Mar 2020.

[21] J. Jänecke and E. Comay. Properties of homogeneous and inhomogeneous mass relations. *Nucl. Phys. A*, 436(1):108–124, 1985.

[22] A.S. Jensen, P.G. Hansen, and B. Jonson. New mass relations and two- and four-nucleon correlations. *Nucl. Phys. A*, 431(3):393–418, 1984.

[23] J.-Y. Zhang, R.F. Casten, and D.S. Brenner. Empirical proton-neutron interaction energies. Linearity and saturation phenomena. *Phys. Lett. B*, 227(1):1–5, 1989.

[24] M. Stoitsov, R. B. Cakirli, R. F. Casten, W. Nazarewicz, and W. Satuła. Empirical Proton-Neutron Interactions and Nuclear Density Functional Theory: Global, Regional, and Local Comparisons. *Phys. Rev. Lett.*, 98:132502, Mar 2007.

[25] M. Bender and P.-H. Heenen. What can be learned from binding energy differences about nuclear structure: The example of δV_{pn}. *Phys. Rev. C*, 83:064319, Jun 2011.

[26] A. Hamaker, E. Leistenschneider, R. Jain, G. Bollen, S.A. Giuliani, K. Lund, W. Nazarewicz, L. Neufcourt, C.R. Nicoloff, D. Puentes, R. Ringle, C.S. Sumithrarachchi, and I.T. Yandow. Precision mass measurement of lightweight self-conjugate nucleus ^{80}Zr. 2021.

[27] Jürgen Eberth, Richard A. Meyer, and Kornelius Sistemich, editors. *Nuclear Structure of the Zirconium Region*, Berlin, Heidelberg, 1988. Springer Berlin Heidelberg.

[28] J H Hamilton, A V Ramayya, C F Maguire, R B Piercey, R Bengtsson, P Moller, J R Nix, Jing ye Zhuang, R L Robinson, and S Frauendorf. Effects of reinforcing shell gaps in the competition between spherical and highly deformed shapes. *J. Phys. G*, 10(5):L87–L91, May 1984.

[29] A. Petrovici, K.W. Schmid, and Amand Faessler. Shape coexistence and shape transition in $N \approx Z$ nuclei from krypton to molybdenum. *Nucl. Phys. A*, 605(3):290–300, 1996.

[30] L. Gaudefroy, A. Obertelli, S. Péru, N. Pillet, S. Hilaire, J. P. Delaroche, M. Girod, and J. Libert. Collective structure of the $N = 40$ isotones. *Phys. Rev. C*, 80:064313, Dec 2009.

[31] Tomás R. Rodríguez and J. Luis Egido. Multiple shape coexistence in the nucleus ^{80}Zr. *Phys. Lett. B*, 705(3):255 – 259, 2011.

[32] K. Kaneko, N. Shimizu, T. Mizusaki, and Y. Sun. Triple enhancement of quasi-SU(3) quadrupole collectivity in Strontium-Zirconium $N \approx Z$ isotopes. *Phys. Lett. B*, 817:136286, 2021.

[33] P.-G. Reinhard, D. J. Dean, W. Nazarewicz, J. Dobaczewski, J. A. Maruhn, and M. R. Strayer. Shape coexistence and the effective nucleon-nucleon interaction. *Phys. Rev. C*, 60:014316, Jun 1999.

[34] C. J. Lister, M. Campbell, A. A. Chishti, W. Gelletly, L. Goettig, R. Moscrop, B. J. Varley, A. N. James, T. Morrison, H. G. Price, J. Simpson, K. Connel, and O. Skeppstedt. Gamma radiation from the $N = Z$ nucleus $^{80}_{40}\mathrm{Zr}_{40}$. *Phys. Rev. Lett.*, 59:1270–1273, Sep 1987.

[35] R. D. O. Llewellyn, M. A. Bentley, R. Wadsworth, H. Iwasaki, J. Dobaczewski, G. de Angelis, J. Ash, D. Bazin, P. C. Bender, B. Cederwall, B. P. Crider, M. Doncel, R. Elder, B. Elman, A. Gade, M. Grinder, T. Haylett, D. G. Jenkins, I. Y. Lee, B. Longfellow, E. Lunderberg, T. Mijatović, S. A. Milne, D. Muir, A. Pastore, D. Rhodes, and D. Weisshaar. Establishing the Maximum Collectivity in Highly Deformed $N = Z$ Nuclei. *Phys. Rev. Lett.*, 124:152501, Apr 2020.

[36] K. Langanke, J. Terasaki, F. Nowacki, D. J. Dean, and W. Nazarewicz. How magic is the magic ^{68}Ni nucleus? *Phys. Rev. C*, 67:044314, Apr 2003.

[37] I. Bentley and S. Frauendorf. Relation between Wigner energy and proton-neutron pairing. *Phys. Rev. C*, 88:014322, Jul 2013.

[38] Léo Neufcourt, Yuchen Cao, Samuel A. Giuliani, Witold Nazarewicz, Erik Olsen, and Oleg B. Tarasov. Quantified limits of the nuclear landscape. *Phys. Rev. C*, 101:044307, Apr 2020.

[39] Zach Meisel. Mapping the frontiers of the nuclear mass surface. *Journal of Physics: Conference Series*, 1668:012026, Oct 2020.

[40] H. Savajols. The SPEG Mass Measurement Program at GANIL. *Hyperfine Interactions*, 132(1):243–252, Jan 2001.

[41] D. Bazin, J.A. Caggiano, B.M. Sherrill, J. Yurkon, and A. Zeller. The S800 spectrograph. *Nuclear Instruments and Methods in Physics Research Section B: Beam Interactions with Materials and Atoms*, 204:629 – 633, 2003. 14th International Conference on Electromagnetic Isotope Separators and Techniques Related to their Applications.

[42] S. Issmer, M. Fruneau, J.A. Pinston, M. Asghar, D. Barnéoud, J. Genevey, Th. Kerscher, and K.E.G. Löbner. Direct mass measurements of A=80 isobars. *The European Physical Journal A - Hadrons and Nuclei*, 2(2):173–177, Jun 1998.

[43] Bernhard Franzke. The heavy ion storage and cooler ring project ESR at GSI. *Nuclear Instruments and Methods in Physics Research Section B: Beam Interactions with Materials and Atoms*, 24-25:18 – 25, 1987.

[44] J.W. Xia, W.L. Zhan, B.W. Wei, Y.J. Yuan, M.T. Song, W.Z. Zhang, X.D. Yang, P. Yuan, D.Q. Gao, H.W. Zhao, X.T. Yang, G.Q. Xiao, K.T. Man, J.R. Dang, X.H. Cai, Y.F. Wang, J.Y. Tang, W.M. Qiao, Y.N. Rao, Y. He, L.Z. Mao, and Z.Z. Zhou. The heavy ion cooler-storage-ring project (HIRFL-CSR) at Lanzhou. *Nuclear Instruments and Methods in Physics Research Section A: Accelerators, Spectrometers, Detectors and Associated Equipment*, 488(1):11 – 25, 2002.

[45] T. Dickel, W.R. Plaß, A. Becker, U. Czok, H. Geissel, E. Haettner, C. Jesch, W. Kinsel, M. Petrick, C. Scheidenberger, A. Simon, and M.I. Yavor. A high-performance multiple-reflection time-of-flight mass spectrometer and isobar separator for the research with exotic nuclei. *Nuclear Instruments and Methods in Physics Research Section A: Accelerators, Spectrometers, Detectors and Associated Equipment*, 777:172 – 188, 2015.

[46] Robert N. Wolf, Markus Eritt, Gerrit Marx, and Lutz Schweikhard. A multi-reflection time-of-flight mass separator for isobaric purification of radioactive ion beams. *Hyperfine Interactions*, 199(1):115–122, Jul 2011.

[47] R.N. Wolf, F. Wienholtz, D. Atanasov, D. Beck, K. Blaum, Ch. Borgmann, F. Herfurth, M. Kowalska, S. Kreim, Yu. A. Litvinov, D. Lunney, V. Manea, D. Neidherr, M. Rosenbusch, L. Schweikhard, J. Stanja, and K. Zuber. Isoltrap's multi-reflection time-of-flight mass separator/spectrometer. *International Journal of Mass Spectrometry*, 349-350:123–133, 2013. 100 years of Mass Spectrometry.

[48] M.P. Reiter, S. Ayet San Andrés, J. Bergmann, T. Dickel, J. Dilling, A. Jacobs, A.A. Kwiatkowski, W.R. Plaß, C. Scheidenberger, D. Short, C. Will, C. Babcock, E. Dunling, A. Finlay, C. Hornung, C. Jesch, R. Klawitter, B. Kootte, D. Lascar, E. Leistenschneider, T. Murböck, S.F. Paul, and M. Yavor. Commissioning and performance of titan's multiple-reflection time-of-flight mass-spectrometer and isobar separator. *Nuclear Instruments and Methods in Physics Research Section A: Accelerators, Spectrometers, Detectors and Associated Equipment*, 1018:165823, 2021.

[49] E. Leistenschneider, M. P. Reiter, S. Ayet San Andrés, B. Kootte, J. D. Holt, P. Navrátil, C. Babcock, C. Barbieri, B. R. Barquest, J. Bergmann, J. Bollig, T. Brunner, E. Dunling, A. Finlay, H. Geissel, L. Graham, F. Greiner, H. Hergert, C. Hornung, C. Jesch, R. Klawitter, Y. Lan, D. Lascar, K. G. Leach, W. Lippert, J. E. McKay, S. F. Paul, A. Schwenk, D. Short, J. Simonis, V. Somà, R. Steinbrügge, S. R. Stroberg, R. Thompson, M. E. Wieser, C. Will, M. Yavor, C. Andreoiu, T. Dickel, I. Dillmann, G. Gwinner, W. R. Plaß, C. Scheidenberger, A. A. Kwiatkowski, and J. Dilling. Dawning of the $n = 32$ shell closure seen through precision mass measurements of neutron-rich titanium isotopes. *Phys. Rev. Lett.*, 120:062503, Feb 2018.

[50] M. Mougeot, D. Atanasov, J. Karthein, R. N. Wolf, P. Ascher, K. Blaum, K. Chrysalidis, G. Hagen, J. D. Holt, W. J. Huang, G. R. Jansen, I. Kulikov, Yu. A. Litvinov, D. Lunney, V. Manea, T. Miyagi, T. Papenbrock, L. Schweikhard, A. Schwenk, T. Steinsberger, S. R. Stroberg, Z. H. Sun, A. Welker, F. Wienholtz, S. G. Wilkins, and K. Zuber. Mass measurements of $^{99–101}$In challenge ab initio nuclear theory of the nuclide ^{100}Sn. *Nature Physics*, 17:1099–1103, Oct 2021.

[51] I. Mardor, S. Ayet San Andrés, T. Dickel, D. Amanbayev, S. Beck, J. Bergmann, H. Geissel, L. Gröf, E. Haettner, C. Hornung, N. Kalantar-Nayestanaki, G. Kripko-Koncz, I. Miskun, A. Mollaebrahimi, W. R. Plaß, C. Scheidenberger, H. Weick, Soumya Bagchi, D. L. Balabanski, A. A. Bezbakh, Z. Brencic, O. Charviakova, V. Chudoba, Paul Constantin, M. Dehghan, A. S. Fomichev, L. V. Grigorenko, O. Hall, M. N. Harakeh, J.-P. Hucka, A. Kankainen, O. Kiselev, R. Knöbel, D. A. Kostyleva, S. A. Krupko, N. Kurkova, N. Kuzminchuk, I. Mukha, I. A. Muzalevskii, D. Nichita, C. Nociforo, Z. Patyk, M. Pfützner, S. Pietri, S. Purushothaman, M. P. Reiter, H. Roesch, F. Schirru, P. G. Sharov, A. Spătaru, G. Stanic, A. State, Y. K. Tanaka, M. Vencelj, M. I. Yavor, and J. Zhao. Mass measurements of As, Se, and Br nuclei, and their

implication on the proton-neutron interaction strength toward the $N = Z$ line. *Phys. Rev. C*, 103:034319, Mar 2021.

[52] Sönke Beck, Brian Kootte, Irene Dedes, Timo Dickel, A. A. Kwiatkowski, Eleni Marina Lykiardopoulou, Wolfgang R. Plaß, Moritz P. Reiter, Corina Andreoiu, Julian Bergmann, Thomas Brunner, Dominique Curien, Jens Dilling, Jerzy Dudek, Eleanor Dunling, Jake Flowerdew, Abdelghafar Gaamouci, Leigh Graham, Gerald Gwinner, Andrew Jacobs, Renee Klawitter, Yang Lan, Erich Leistenschneider, Nikolay Minkov, Victor Monier, Ish Mukul, Stefan F. Paul, Christoph Scheidenberger, Robert I. Thompson, James L. Tracy, Michael Vansteenkiste, Hua-Lei Wang, Michael E. Wieser, Christian Will, and Jie Yang. Mass measurements of neutron-deficient yb isotopes and nuclear structure at the extreme proton-rich side of the $n = 82$ shell. *Phys. Rev. Lett.*, 127:112501, Sep 2021.

[53] P. Schury, T. Niwase, M. Wada, P. Brionnet, S. Chen, T. Hashimoto, H. Haba, Y. Hirayama, D. S. Hou, S. Iimura, H. Ishiyama, S. Ishizawa, Y. Ito, D. Kaji, S. Kimura, H. Koura, J. J. Liu, H. Miyatake, J.-Y. Moon, K. Morimoto, K. Morita, D. Nagae, M. Rosenbusch, A. Takamine, Y. X. Watanabe, H. Wollnik, W. Xian, and S. X. Yan. First high-precision direct determination of the atomic mass of a superheavy nuclide. *Phys. Rev. C*, 104:L021304, Aug 2021.

[54] Sascha Rau, Fabian Heiße, Florian Köhler-Langes, Sangeetha Sasidharan, Raphael Haas, Dennis Renisch, Christoph E. Düllmann, Wolfgang Quint, Sven Sturm, and Klaus Blaum. Penning trap mass measurements of the deuteron and the HD^+ molecular ion. *Nature*, 585:43 – 47, Sep 2020.

[55] A. A. Valverde, G. Bollen, M. Brodeur, R. A. Bryce, K. Cooper, M. Eibach, K. Gulyuz, C. Izzo, D. J. Morrissey, M. Redshaw, R. Ringle, R. Sandler, S. Schwarz, C. S. Sumithrarachchi, and A. C. C. Villari. First Direct Determination of the Superallowed β-Decay Q_{EC} Value for ^{14}O. *Phys. Rev. Lett.*, 114:232502, Jun 2015.

[56] M. Smith, M. Brodeur, T. Brunner, S. Ettenauer, A Lapierre, R. Ringle, V. L. Ryjkov, F. Ames, P. Bricault, G. W. F. Drake, P. Delheij, D. Lunney, F. Sarazin, and J. Dilling. First Penning-Trap Mass Measurement of the Exotic Halo Nucleus ^{11}Li. *Phys. Rev. Lett.*, 101:202501, Nov 2008.

[57] G. Bollen, S. Becker, H.-J. Kluge, M. König, R.B. Moore, T. Otto, H. Raimbault-Hartmann, G. Savard, L. Schweikhard, and H. Stolzenberg. ISOLTRAP: a tandem Penning trap system for accurate on-line mass determination of short-lived isotopes. *Nuclear Instruments and Methods in Physics Research Section A: Accelerators, Spectrometers, Detectors and Associated Equipment*, 368(3):675 – 697, 1996.

[58] V.S. Kolhinen, T. Eronen, J. Hakala, A. Jokinen, S. Kopecky, S. Rinta-Antila, J. Szerypo, and J. Äystö. Penning trap for isobaric mass separation at IGISOL. *Nuclear*

Instruments and Methods in Physics Research Section B: Beam Interactions with Materials and Atoms, 204:502 – 506, 2003. 14th International Conference on Electromagnetic Isotope Separators and Techniques Related to their Applications.

[59] G. Sikler, D. Ackermann, F. Attallah, D. Beck, J. Dilling, S.A. Elisseev, H. Geissel, D. Habs, S. Heinz, F. Herfurth, F. Heßberger, S. Hofmann, H.-J. Kluge, C. Kozhuharov, G. Marx, M. Mukherjee, J. Neumayr, W.R. Plaß, W. Quint, S. Rahaman, D. Rodrıguez, C. Scheidenberger, M. Tarisien, P. Thirolf, V. Varentsov, C. Weber, and Z. Zhou. First on-line test of SHIPTRAP. *Nuclear Instruments and Methods in Physics Research Section B: Beam Interactions with Materials and Atoms*, 204:482 – 486, 2003. 14th International Conference on Electromagnetic Isotope Separators and Techniques Related to their Applications.

[60] G. Savard, R.C. Barber, D. Beeching, F. Buchinger, J.E. Crawford, S. Gulick, X. Feng, E. Hagberg, J.C. Hardy, V.T. Koslowsky, J.K.P. Lee, R.B. Moore, K.S. Sharma, and M. Watson. The Canadian Penning trap mass spectrometer. *Nuclear Physics A*, 626(1):353 – 356, 1997. Proceedings of the Third International Conference on Nuclear Physics at Storage Rings.

[61] A. A. Kwiatkowski, C. Andreoiu, J. C. Bale, T. Brunner, A. Chaudhuri, U. Chowdhury, P. Delheij, S. Ettenauer, D. Frekers, A. T. Gallant, A. Grossheim, G. Gwinner, F. Jang, A. Lennarz, T. Ma, E. Mané, M. R. Pearson, B. E. Schultz, M. C. Simon, V. V. Simon, and J. Dilling. TITAN: An ion trap facility for on-line mass measurement experiments. *Hyperfine Interactions*, 225(1):143–155, Jan 2014.

[62] Ryan Ringle, Stefan Schwarz, and Georg Bollen. Penning trap mass spectrometry of rare isotopes produced via projectile fragmentation at the LEBIT facility. *International Journal of Mass Spectrometry*, 349-350:87 – 93, 2013. 100 years of Mass Spectrometry.

[63] A. A. Valverde, M. Brodeur, G. Bollen, M. Eibach, K. Gulyuz, A. Hamaker, C. Izzo, W.-J. Ong, D. Puentes, M. Redshaw, R. Ringle, R. Sandler, S. Schwarz, C. S. Sumithrarachchi, J. Surbrook, A. C. C. Villari, and I. T. Yandow. High-Precision Mass Measurement of ^{56}Cu and the Redirection of the *rp*-Process Flow. *Phys. Rev. Lett.*, 120:032701, Jan 2018.

[64] Alan G. Marshall, Christopher L. Hendrickson, and George S. Jackson. Fourier transform ion cyclotron resonance mass spectrometry: A primer. *Mass Spectrometry Reviews*, 17(1):1–35, 1998.

[65] G. Gabrielse, L. Haarsma, and S.L. Rolston. Open-endcap Penning traps for high precision experiments. *International Journal of Mass Spectrometry and Ion Processes*, 88(2):319 – 332, 1989.

[66] H. Raimbault-Hartmann, D. Beck, G. Bollen, M. König, H.-J. Kluge, E. Schark, J. Stein, S. Schwarz, and J. Szerypo. A cylindrical Penning trap for capture, mass

selective cooling, and bunching of radioactive ion beams. *Nuclear Instruments and Methods in Physics Research Section B: Beam Interactions with Materials and Atoms*, 126(1):378 – 382, 1997. International Conference on Electromagnetic Isotope Separators and Techniques Related to Their Applications.

[67] Lowell S. Brown and Gerald Gabrielse. Geonium theory: Physics of a single electron or ion in a Penning trap. *Rev. Mod. Phys.*, 58:233–311, Jan 1986.

[68] G. Gabrielse. Why Is Sideband Mass Spectrometry Possible with Ions in a Penning Trap? *Phys. Rev. Lett.*, 102:172501, Apr 2009.

[69] Lowell S. Brown and Gerald Gabrielse. Precision spectroscopy of a charged particle in an imperfect penning trap. *Phys. Rev. A*, 25:2423–2425, Apr 1982.

[70] S. Eliseev, K. Blaum, M. Block, C. Droese, M. Goncharov, E. Minaya Ramirez, D. A. Nesterenko, Yu. N. Novikov, and L. Schweikhard. Phase-Imaging Ion-Cyclotron-Resonance Measurements for Short-Lived Nuclides. *Phys. Rev. Lett.*, 110:082501, Feb 2013.

[71] R. Ringle, G. Bollen, A. Prinke, J. Savory, P. Schury, S. Schwarz, and T. Sun. A "Lorentz" steerer for ion injection into a Penning trap. *International Journal of Mass Spectrometry*, 263(1):38 – 44, 2007.

[72] Klaus Blaum. High-accuracy mass spectrometry with stored ions. *Physics Reports*, 425(1):1 – 78, 2006.

[73] P. Duhamel and M. Vetterli. Fast fourier transforms: A tutorial review and a state of the art. *Signal Processing*, 19(4):259 – 299, 1990.

[74] J.B. Jeffries, S.E. Barlow, and G.H. Dunn. Theory of space-charge shift of ion cyclotron resonance frequencies. *International Journal of Mass Spectrometry and Ion Processes*, 54(1):169 – 187, 1983.

[75] J. B. Johnson. Thermal Agitation of Electricity in Conductors. *Phys. Rev.*, 32:97–109, Jul 1928.

[76] G. Bollen, R. B. Moore, G. Savard, and H. Stolzenberg. The accuracy of heavy-ion mass measurements using time of flight-ion cyclotron resonance in a Penning trap. *Journal of Applied Physics*, 68(9):4355–4374, 1990.

[77] S. Lohse, J. Berrocal, S. Böhland, J. van de Laar, M. Block, S. Chenmarev, Ch. E. Düllmann, Sz. Nagy, J. G. Ramírez, and D. Rodríguez. Quartz resonators for penning traps toward mass spectrometry on the heaviest ions. *Review of Scientific Instruments*, 91(9):093202, 2020.

[78] D.J. Morrissey, B.M. Sherrill, M. Steiner, A. Stolz, and I. Wiedenhoever. Commissioning the A1900 projectile fragment separator. *Nuclear Instruments and Methods in Physics Research Section B: Beam Interactions with Materials and Atoms*, 204:90 – 96, 2003. 14th International Conference on Electromagnetic Isotope Separators and Techniques Related to their Applications.

[79] C.S. Sumithrarachchi, D.J. Morrissey, S. Schwarz, K. Lund, G. Bollen, R. Ringle, G. Savard, and A.C.C. Villari. Beam thermalization in a large gas catcher. *Nuclear Instruments and Methods in Physics Research Section B: Beam Interactions with Materials and Atoms*, 463:305 – 309, 2020.

[80] K.R. Lund, G. Bollen, D. Lawton, D.J. Morrissey, J. Ottarson, R. Ringle, S. Schwarz, C.S. Sumithrarachchi, A.C.C. Villari, and J. Yurkon. Online tests of the Advanced Cryogenic Gas Stopper at NSCL. *Nucl. Instrum. Methods Phys. Res. B*, 463:378 – 381, 2020.

[81] S. Schwarz, G. Bollen, S. Chouhan, J.J. Das, M. Green, C. Magsig, D.J. Morrissey, J. Ottarson, C. Sumithrarachchi, A.C.C. Villari, and A. Zeller. The NSCL cyclotron gas stopper – Entering commissioning. *Nuclear Instruments and Methods in Physics Research Section B: Beam Interactions with Materials and Atoms*, 376:256 – 259, 2016. Proceedings of the XVIIth International Conference on Electromagnetic Isotope Separators and Related Topics (EMIS2015), Grand Rapids, MI, U.S.A., 11-15 May 2015.

[82] S. Schwarz, G. Bollen, R. Ringle, J. Savory, and P. Schury. The LEBIT ion cooler and buncher. *Nuclear Instruments and Methods in Physics Research Section A: Accelerators, Spectrometers, Detectors and Associated Equipment*, 816:131 – 141, 2016.

[83] R. Ringle, G. Bollen, A. Prinke, J. Savory, P. Schury, S. Schwarz, and T. Sun. The LEBIT 9.4T Penning trap mass spectrometer. *Nuclear Instruments and Methods in Physics Research Section A: Accelerators, Spectrometers, Detectors and Associated Equipment*, 604(3):536 – 547, 2009.

[84] C. Izzo, G. Bollen, S. Bustabad, M. Eibach, K. Gulyuz, D.J. Morrissey, M. Redshaw, R. Ringle, R. Sandler, S. Schwarz, and A.A. Valverde. A laser ablation source for offline ion production at LEBIT. *Nuclear Instruments and Methods in Physics Research Section B: Beam Interactions with Materials and Atoms*, 376:60 – 63, 2016. Proceedings of the XVIIth International Conference on Electromagnetic Isotope Separators and Related Topics (EMIS2015), Grand Rapids, MI, U.S.A., 11-15 May 2015.

[85] R. Sandler, G. Bollen, J. Dissanayake, M. Eibach, K. Gulyuz, A. Hamaker, C. Izzo, X. Mougeot, D. Puentes, F. G. A. Quarati, M. Redshaw, R. Ringle, and I. Yandow. Direct determination of the ^{138}La β-decay q value using penning trap mass spectrometry. *Phys. Rev. C*, 100:014308, Jul 2019.

[86] R. Sandler, G. Bollen, N. D. Gamage, A. Hamaker, C. Izzo, D. Puentes, M. Redshaw, R. Ringle, and I. Yandow. Investigation of the potential ultralow q-value β-decay candidates ^{89}Sr and ^{139}Ba using penning trap mass spectrometry. *Phys. Rev. C*, 100:024309, Aug 2019.

[87] N. R. Daly. Scintillation Type Mass Spectrometer Ion Detector. *Review of Scientific Instruments*, 31(3):264–267, 1960.

[88] K. Blaum, D. Beck, G. Bollen, P. Delahaye, C. Guénaut, F. Herfurth, A. Kellerbauer, H.-J. Kluge, D. Lunney, S. Schwarz, L. Schweikhard, and C. Yazidjian. Population inversion of nuclear states by a Penning trap mass spectrometer. *Europhys. Lett.*, 67(4):586–592, Aug 2004.

[89] A.A. Kwiatkowski, G. Bollen, M. Redshaw, R. Ringle, and S. Schwarz. Isobaric beam purification for high precision Penning trap mass spectrometry of radioactive isotope beams with SWIFT. *International Journal of Mass Spectrometry*, 379:9 – 15, 2015.

[90] K. Gulyuz, J. Ariche, G. Bollen, S. Bustabad, M. Eibach, C. Izzo, S. J. Novario, M. Redshaw, R. Ringle, R. Sandler, S. Schwarz, and A. A. Valverde. Determination of the direct double-β-decay Q value of ^{96}Zr and atomic masses of $^{90-92,94,96}$Zr and $^{92,94-98,100}$Mo. *Phys. Rev. C*, 91:055501, May 2015.

[91] R. Ringle, T. Sun, G. Bollen, D. Davies, M. Facina, J. Huikari, E. Kwan, D. J. Morrissey, A. Prinke, J. Savory, P. Schury, S. Schwarz, and C. S. Sumithrarachchi. High-precision Penning trap mass measurements of ^{37,38}Ca and their contributions to conserved vector current and isobaric mass multiplet equation. *Phys. Rev. C*, 75:055503, May 2007.

[92] A. Kellerbauer, K. Blaum, G. Bollen, F. Herfurth, H.-J. Kluge, M. Kuckein, E. Sauvan, C. Scheidenberger, and L. Schweikhard. From direct to absolute mass measurements: A study of the accuracy of ISOLTRAP. *The European Physical Journal D - Atomic, Molecular, Optical and Plasma Physics*, 22:53–64, 2003.

[93] Raymond T. Birge. The Calculation of Errors by the Method of Least Squares. *Phys. Rev.*, 40:207–227, Apr 1932.

[94] A. Kankainen, L. Batist, S. A. Eliseev, V.-V. Elomaa, T. Eronen, U. Hager, J. Hakala, A. Jokinen, I. Moore, Yu. N. Novikov, H. Penttilä, K. Peräjärvi, Popov. A. V., S. Rahaman, S. Rinta-Antila, P. Ronkanen, A. Saastamoinen, D. M. Seliverstov, T. Sonoda, G. K. Vorobjev, and J. Äystö. Mass measurements of neutron-deficient nuclides close to A = 80 with a Penning trap. *Eur. Phys. J. A*, 29:271 – 280, 2006.

[95] M. Vilén, A. Kankainen, P. Baczyk, L. Canete, J. Dobaczewski, T. Eronen, S. Geldhof, A. Jokinen, M. Konieczka, J. Kostensalo, I. D. Moore, D. A. Nesterenko, H. Penttilä, I. Pohjalainen, M. Reponen, S. Rinta-Antila, A. de Roubin, W. Satuła, and J. Suhonen.

High-precision mass measurements and production of neutron-deficient isotopes using heavy-ion beams at IGISOL. *Phys. Rev. C*, 100:054333, Nov 2019.

[96] Y.M. Xing, K.A. Li, Y.H. Zhang, X.H. Zhou, M. Wang, Yu.A. Litvinov, K. Blaum, S. Wanajo, S. Kubono, G. Martínez-Pinedo, A. Sieverding, R.J. Chen, P. Shuai, C.Y. Fu, X.L. Yan, W.J. Huang, X. Xu, X.D. Tang, H.S. Xu, T. Bao, X.C. Chen, B.S. Gao, J.J. He, Y.H. Lam, H.F. Li, J.H. Liu, X.W. Ma, R.S. Mao, M. Si, M.Z. Sun, X.L. Tu, Q. Wang, J.C. Yang, Y.J. Yuan, Q. Zeng, P. Zhang, X. Zhou, W.L. Zhan, S. Litvinov, G. Audi, T. Uesaka, Y. Yamaguchi, T. Yamaguchi, A. Ozawa, C. Fröhlich, T. Rauscher, F.-K. Thielemann, B.H. Sun, Y. Sun, A.C. Dai, and F.R. Xu. Mass measurements of neutron-deficient Y, Zr, and Nb isotopes and their impact on rp and νp nucleosynthesis processes. *Phys. Lett. B*, 781:358–363, 2018.

[97] A. S. Lalleman, G. Auger, W. Mittig, M. Chabert, M. Chartier, J. Fermé, A. Gillibert, A. Lépine-Szily, M. Lewitowicz, M. H. Moscatello, N. A. Orr, G. Politi, F. Sarazin, H. Savajols, P. Van Isacker, and A. C. C. Villari. Mass Measurements of Exotic Nuclei around N=Z=40 with CSS2. *Hyperfine Interactions*, 132(1):313–320, Jan 2001.

[98] J. A. Clark, G. Savard, K. S. Sharma, J. Vaz, J. C. Wang, Z. Zhou, A. Heinz, B. Blank, F. Buchinger, J. E. Crawford, S. Gulick, J. K. P. Lee, A. F. Levand, D. Seweryniak, G. D. Sprouse, and W. Trimble. Precise Mass Measurement of ^{68}Se, a Waiting-Point Nuclide along the rp Process. *Phys. Rev. Lett.*, 92:192501, May 2004.

[99] M. B. Gómez-Hornillos, M. Chartier, W. Mittig, A. Lépine-Szily, L. Caballero, C. E. Demonchy, G. Georgiev, N. A. Orr, G. Politi, M. Rousseau, P. Roussel-Chomaz, and A. C. C. Villari. Direct mass measurements of ^{68}Se and ^{80}Y. *Phys. Rev. C*, 78:014311, Jul 2008.

[100] H. Schatz and W.-J. Ong. Dependence of X-Ray Burst Models on Nuclear Masses. *Astrophys. J.*, 844(2):139, Aug 2017.

[101] P.-G. Reinhard, M. Bender, W. Nazarewicz, and T. Vertse. From finite nuclei to the nuclear liquid drop: Leptodermous expansion based on self-consistent mean-field theory. *Phys. Rev. C*, 73:014309, Jan 2006.

[102] M. Bender, T. Cornelius, G.A. Lalazissis, J.A. Maruhn, W. Nazarewicz, and P.-G. Reinhard. The $Z = 82$ shell closure in neutron-deficient Pb isotopes. *Eur. Phys. J. A*, 14(1):23–28, 2002.

[103] Á. Koszorús, X. F. Yang, W. G. Jiang, S. J. Novario, S. W. Bai, J. Billowes, C. L. Binnersley, M. L. Bissell, T. E. Cocolios, B. S. Cooper, R. P. de Groote, A. Ekström, K. T. Flanagan, C. Forssén, S. Franchoo, R. F. Garcia Ruiz, F. P. Gustafsson, G. Hagen, G. R. Jansen, A. Kanellakopoulos, M. Kortelainen, W. Nazarewicz, G. Neyens, T. Papenbrock, P. G. Reinhard, B. K. Sahoo, C. M. Ricketts, A. R. Vernon, and S. G.

Wilkins. Charge radii of exotic potassium isotopes challenge nuclear theory and the magic character of $N = 32$. *Nat. Phys.*, 17:439–443, 2021.

[104] D. R. Phillips, R. J. Furnstahl, U. Heinz, T. Maiti, W. Nazarewicz, F. M. Nunes, M. Plumlee, M. T. Pratola, S. Pratt, F. G. Viens, and S. M. Wild. Get on the BAND wagon: a Bayesian framework for quantifying model uncertainties in nuclear dynamics. *J. Phys. G*, 48(7):072001, May 2021.

[105] Léo Neufcourt, Yuchen Cao, Samuel Giuliani, Witold Nazarewicz, Erik Olsen, and Oleg B. Tarasov. Beyond the proton drip line: Bayesian analysis of proton-emitting nuclei. *Phys. Rev. C*, 101:014319, Jan 2020.

[106] J. Bartel, P. Quentin, M. Brack, C. Guet, and H.-B. Håkansson. Towards a better parametrisation of Skyrme-like effective forces: A critical study of the SkM force. *Nucl. Phys. A*, 386(1):79–100, 1982.

[107] J. Dobaczewski, H. Flocard, and J. Treiner. Hartree-Fock-Bogolyubov description of nuclei near the neutron-drip line. *Nucl. Phys. A*, 422(1):103–139, 1984.

[108] E Chabanat, P Bonche, P Haensel, J Meyer, and R Schaeffer. New Skyrme effective forces for supernovae and neutron rich nuclei. *Phys. Scr.*, T56:231–233, Jan 1995.

[109] P. Klüpfel, P.-G. Reinhard, T. J. Bürvenich, and J. A. Maruhn. Variations on a theme by Skyrme: A systematic study of adjustments of model parameters. *Phys. Rev. C*, 79:034310, Mar 2009.

[110] M. Kortelainen, T. Lesinski, J. Moré, W. Nazarewicz, J. Sarich, N. Schunck, M. V. Stoitsov, and S. Wild. Nuclear energy density optimization. *Phys. Rev. C*, 82:024313, Aug 2010.

[111] M. Kortelainen, J. McDonnell, W. Nazarewicz, P.-G. Reinhard, J. Sarich, N. Schunck, M. V. Stoitsov, and S. M. Wild. Nuclear energy density optimization: Large deformations. *Phys. Rev. C*, 85:024304, Feb 2012.

[112] M. Kortelainen, J. McDonnell, W. Nazarewicz, E. Olsen, P.-G. Reinhard, J. Sarich, N. Schunck, S. M. Wild, D. Davesne, J. Erler, and A. Pastore. Nuclear energy density optimization: Shell structure. *Phys. Rev. C*, 89:054314, May 2014.

[113] S. Goriely, S. Hilaire, M. Girod, and S. Péru. First Gogny-Hartree-Fock-Bogoliubov Nuclear Mass Model. *Phys. Rev. Lett.*, 102:242501, Jun 2009.

[114] M. Baldo, L. M. Robledo, P. Schuck, and X. Viñas. New Kohn-Sham density functional based on microscopic nuclear and neutron matter equations of state. *Phys. Rev. C*, 87:064305, Jun 2013.

[115] P. Möller, A.J. Sierk, T. Ichikawa, and H. Sagawa. Nuclear ground-state masses and deformations: FRDM(2012). *Atom. Data Nucl. Data Tables*, 109-110:1 – 204, 2016.

[116] T. Otto, G. Bollen, G. Savard, L. Schweikhard, H. Stolzenberg, G. Audi, R.B. Moore, G. Rouleau, J. Szerypo, and Z. Patyk. Penning-trap mass measurements of neutron-deficient rb and sr isotopes. *Nuclear Physics A*, 567(2):281–302, 1994.

[117] G. Sikler, G. Audi, D. Beck, K. Blaum, G. Bollen, F. Herfurth, A. Kellerbauer, H.-J. Kluge, D. Lunney, M. Oinonen, C. Scheidenberger, S. Schwarz, and J. Szerypo. Mass measurements on neutron-deficient sr and neutron-rich sn isotopes with the isoltrap mass spectrometer. *Nuclear Physics A*, 763:45–58, 2005.

[118] David A Dahl. SIMION for the personal computer in reflection. *International Journal of Mass Spectrometry*, 200(1):3 – 25, 2000. Volume 200: The state of the field as we move into a new millenium.

[119] R. Ringle. *High-Precision Mass Measurement of ^{38}Ca and Development of the LEBIT 9.4-T Penning Trap System.* PhD thesis, Michigan State University, 2006.

[120] D. Beck, K. Blaum, G. Bollen, P. Delahaye, S. George, C. Guénaut, F. Herfurth, A. Herlert, D. Lunney, L. Schweikhard, and C. Yazidjian. Electric and magnetic field optimization procedure for Penning trap mass spectrometers. *Nuclear Instruments and Methods in Physics Research Section A: Accelerators, Spectrometers, Detectors and Associated Equipment*, 598(2):635–641, 2009.

[121] M. Brodeur, V.L. Ryjkov, T. Brunner, S. Ettenauer, A.T. Gallant, V.V. Simon, M.J. Smith, A. Lapierre, R. Ringle, P. Delheij, M. Good, D. Lunney, and J. Dilling. Verifying the accuracy of the TITAN Penning-trap mass spectrometer. *International Journal of Mass Spectrometry*, 310:20–31, 2012.